

Search for decay $\Upsilon(5S) \rightarrow \gamma W_{bJ}$

Nicholas Corrado, Vladimir Savinov

University of Pittsburgh, Pittsburgh, PA-15260, USA

Abstract

The recent discovery of the states Z_b and Z'_b implies the possible existence of a new family of hadronic resonances including molecular states dubbed W_{bJ} . We describe a search for W_{bJ} in the decay $\Upsilon(5S) \rightarrow \gamma W_{bJ}$ using 121.4 fb^{-1} of data collected at the $\Upsilon(5S)$ resonance with the Belle detector at the KEKB asymmetric-energy electron-positron collider. Using Monte Carlo simulation, we study Belle's sensitivity to the decay $\Upsilon(5S) \rightarrow \gamma W_{bJ}$, search for its presence in Belle data and describe the procedure we would use to establish an upper limit on the visible production cross section for these new states.

16 Contents

17	1 Introduction	1
18	1.1 Motivation	1
19	1.2 New Spectroscopy	1
20	1.3 Radiative Decays $\Upsilon(5S) \rightarrow \gamma W_{bJ}$	3
21	1.4 Expected Signal in Data	4
22	2 Monte Carlo and Data Samples	6
23	3 Selection Criteria	6
24	3.1 Selection of Photon Candidates	7
25	3.2 Selection of Pion and Muon Candidates	8
26	3.3 Selection of $\Upsilon(5S)$ Candidates	8
27	3.4 Best Candidate Selection	8
28	4 Signal Monte Carlo Studies	8
29	4.1 Signal Monte Carlo Distributions	8
30	4.2 Description of the Signal Region	12
31	4.3 Trigger Simulation	15
32	5 Background Studies	18
33	5.1 Generic Monte Carlo and Blinded Data	18
34	6 Background from $\Upsilon(5S) \rightarrow \Upsilon(1S)\pi^+\pi^-$ with Initial State Radiation (ISR)	20
35	6.1 $\Upsilon(5S) \rightarrow \Upsilon(1S)\pi^+\pi^-$ ISR Monte Carlo Sample	20
36	6.2 Background Shape of $\Upsilon(5S) \rightarrow \Upsilon(1S)\pi^+\pi^-$ with ISR	22
37	7 Contribution from $\Upsilon(5S) \rightarrow Z_b^{(\prime)\pm}\pi^\mp$	26
38	8 Fitting	26
39	8.1 Signal and Background PDFs	26
40	8.2 Confidence Belts	28
41	8.3 Linearity Study	29
42	8.4 Sensitivity Estimation	31
43	9 Search Strategy Summary	33
44	10 Appendix	34
45	10.1 Final State Radiation	34
46	10.2 Changes in the Analysis between Note v1.5 and v2.0	35
47	10.2.1 Signal Photon Energy Conundrum	36
48	10.3 Fitting Strategy	41

49 List of Figures

50	1	Pure $b\bar{b}$ bottomonium mass spectrum for a relativized quark model	2
51	2	Spectrum of bottomonium and bottomonium-like mesons.	3
52	3	Expected family of molecular isotriplet resonances.	5
53	4	Various MC distributions which informed our selection criteria.	7
54	5	Signal MC distributions	10
55	6	$M(\pi^+\pi^+\mu^+\mu^-)$ and $M(\pi^+\pi^-(\mu^+\mu^-)_{\text{fit}})$ resolutions for signal events	11
56	7	ΔE resolution and quantities contributing to ΔE resolution.	12
57	8	Definitions of important regions	14
58	9	Offline trigger selection for reconstructed signal MC events.	16
59	10	Offline trigger efficiency for reconstructed signal MC events.	17
60	11	Identifying background present in data but not in generic MC.	18
61	12	Motivation for ISR studies.	20
62	13	Reweighted ISR energy spectrum	21
63	14	Background due to ISR.	22
64	15	Effect of decay models on $M(\pi^+\pi^-(\mu^+\mu^-)_{\text{fit}})$ distribution.	23
65	16	Effect of decay models on muon angular distribution.	24
66	17	Effect of ΔE cut on ISR background shape.	25
67	18	Definitions of subdivisions of the grand sideband region	25
68	19	Distribution of $M(\pi^+\pi^-(\mu^+\mu^-)_{\text{fit}})$ vs $M_{\text{rec}}(\gamma)$ for $\Upsilon(5S) \rightarrow Z_b^{(\prime)\pm}\pi^\mp$ MC	27
69	20	Distribution of $M(\pi^+\pi^-(\mu^+\mu^-)_{\text{fit}})$ for $\Upsilon(5S) \rightarrow Z_b^{(\prime)\pm}\pi^\mp$	27
70	21	Fitting background MC and data	29
71	22	90% confidence belts for frequentist method.	30
72	23	Average $N_{\text{sig}}^{\text{fit}}$ for varying values of $N_{\text{sig}}^{\text{gen}}$. The solid black line is the result of fitting these points to the linear function $f(x) = p_0 + p_1x$. The resulting fit parameters are shown in the box on the top right.	31
73			
74			
75	24	$N_{\text{sig}}^{\text{fit}}$ Distributions for ensemble tests with different $N_{\text{sig}}^{\text{gen}}$	32
76	25	Final state radiation from charged tracks	34
77	26	Signal invariant mass for a special MC sample with the original selection criteria.	38
78	27	Photon energy vs signal invariant mass for a special MC sample with the original selection criteria.	39
79			
80	28	Photon energy vs signal invariant mass for a special MC sample with relaxed selection criteria.	40
81			
82	29	Signal invariant mass for a special MC sample with relaxed selection criteria.	41
83	30	Signal invariant mass for a special MC sample with relaxed selection criteria (log scale).	42
84			
85	31	Photon energy vs signal invariant mass for blinded data with relaxed selection criteria.	43
86			
87	32	Signal invariant mass for blinded data with relaxed selection criteria.	44
88	33	Signal invariant mass for blinded data with relaxed selection criteria (log scale).	45
89	34	Signal invariant mass for blinded data with relaxed selection criteria (log scale, finer bins).	46
90			
91	35	Signal invariant mass for blinded data with relaxed selection criteria (log scale, fitting region).	47
92			

93	36	Photon energy vs signal invariant mass for ISR MC sample described in section 6 with relaxed selection criteria.	48
94			
95	37	Signal invariant mass for ISR MC sample described in section 6 with relaxed selection criteria.	49
96			
97	38	Signal invariant mass for ISR MC sample described in section 6 with relaxed selection criteria (log scale).	50
98			
99	39	Signal invariant mass for ISR MC sample described in section 6 with relaxed selection criteria (log scale, fitting region only).	51
100			
101	40	The results of the ML fit for ISR MC sample.	52
102	41	The results of the ML fit for ISR MC sample excluding the signal region.	52
103	42	The results of the ML fit for sidebands of the blinded data sample.	53
104	43	The results of the ML fit for ISR MC sample with background model and signal PDF shape.	53
105			
106	44	The results of the ML fit for ISR MC sample with background model and signal PDF shape (mass is a free parameter).	54
107			
108	45	The results of the ML fit for ISR + signal (50 events) MC sample with background model and signal PDF shape (mass is a free parameter).	54
109			
110	46	The results of the scan for ISR MC sample with background model and signal PDF shape.	55
111			
112	47	The results of the scan for ISR MC sample + 50 toy MC signal events with background model and signal PDF shape.	55
113			
114	48	The results of the scan for ISR MC sample with background model and signal PDF shape.	56
115			
116	49	The results of the scan for ISR MC sample + 50 toy MC signal events with background model and signal PDF shape.	56
117			

118 **List of Tables**

119	1	Possible molecular isotriplet states in decays of $\Upsilon(5S)$ and $\Upsilon(6S)$	4
120	2	EvtGen decay models used in Monte Carlo simulation of signal processes. . .	6
121	3	Selection criteria for $\Upsilon(5S) \rightarrow \gamma W_{bJ}$	9
122	4	Quantities contributing to widths of measured quantities	10
123	5	Definitions of the signal region and other important regions.	13
124	6	Backgrounds labeled in Fig. 11.	19
125	7	Decay models used in background ISR MC	22
126	8	Definitions of subdivisions of the grand sideband region	24
127	9	Comparing the number of events in ISR MC and blinded data in the subdivided grand sideband region	26
128			
129	10	Values of fixed quantities in the signal PDF model	28
130	11	Values of quantities used in upper limit calculation	33
131	12	The new (wider) blinded region in data. The important change is shown in	
132		red color. However, it is redundant and adds nothing new as compared to the	
133		second line in this table.	36

1 Introduction

Version 1.5 of this Note includes new plots, various corrections suggested and the answers to the questions asked by the referees. Also, this version includes two new appendices: section 10.2, “Changes in the Analysis between Note v1.5 and v2.0” and section 10.3, “Fitting Strategy”. Note that the plots in the main part of the note (*i.e.* excluding the plots in the Appendix part) have been prepared using the original analysis. The changes outlined in the section 10.2 and used for preparing plots in sections 10.2 and 10.3, have not yet been applied to the main body of the text of this Note.

1.1 Motivation

In this document, we describe a search for new hadronic states of matter – bottomonium-like particles dubbed W_{bJ} – in radiative decays of $\Upsilon(5S)$. These states are believed to be of molecular nature, where a pair of colored $B_{(s)}^{(*)}$ mesons, each containing a b or an anti- b quark, are held together by the strong interaction (in a way similar to single-pion exchange force mechanism in QCD-inspired low-energy models). As with conventional bottomonium, *i.e.* $b\bar{b}$ states, these molecular states exhibit their own spectroscopy. However, their masses and properties obviously could not be predicted using $q\bar{q}$ potential models. We are motivated by Belle’s discoveries [1, 2, 3, 4] of the $Z_b(10610)$ and $Z_b(10650)$ states (referred to in the rest of this document as Z_b and Z'_b or just Z_b) and theoretical predictions which use the molecular picture to explain the nature of the Z_b and predict the existence of additional hadronic states. These predictions can be used to explain various long-standing puzzles in the (no longer pure) bottomonium at energies above the threshold for B meson pair production.

1.2 New Spectroscopy

Since the discovery of the Υ meson, the b quark, and B mesons [5], conventional bottomonium states have been a rich source of information about strong interaction dynamics in the approximately non-relativistic $b\bar{b}$ system. Vector bottomonium and bottomonium-like states ($\Upsilon(nS)$ mesons) can be produced directly in the e^+e^- annihilation. Three of these states – $\Upsilon(1S)$, $\Upsilon(2S)$, and $\Upsilon(3S)$ – have masses below the $B\bar{B}$ threshold [6]. These states are believed to be pure $b\bar{b}$, and their properties are relatively easy to understand using potential models. Such relativized models [7] predict 34 $b\bar{b}$ bound states below $\Upsilon(4S)$ energy, 15 of which have been observed. We show the predictions for the energy levels in the $b\bar{b}$ spectroscopy [8, 9] in Fig. 1.

Hadronic transitions (such as, *e.g.* $\Upsilon(3S) \rightarrow \pi^+\pi^-\Upsilon(1S)$) between bottomonium states provide an excellent opportunity to study QCD dynamics in non-perturbative regime by comparing the measured masses, widths, branching fractions, angular and invariant mass distributions with the theoretical predictions. For pure bottomonium states – $b\bar{b}$ resonances below $B\bar{B}$ threshold – the hadronic transitions proceed via radiating the strong field, *i.e.*, by emitting the gluons which convert into light hadrons. States above $B\bar{B}$ threshold, starting with $\Upsilon(4S)$, are significantly wider than the lower-mass states, and their hadronic transitions are known to exhibit certain properties that are unexpected for pure $b\bar{b}$ states. While the latter are well described from the perspective of Heavy Quark Spin Symmetry (HQSS) where

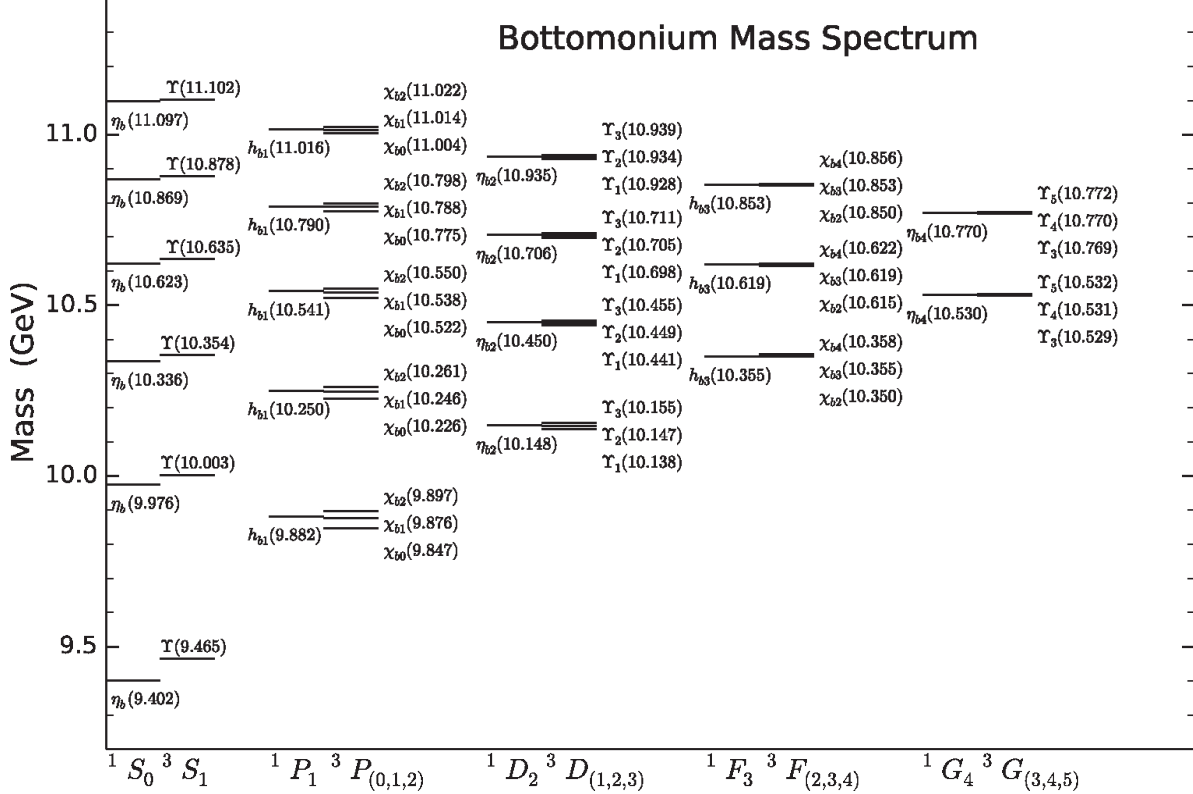


Figure 1: Pure (*i.e.* $b\bar{b}$) bottomonium mass spectrum [8] calculated using a relativized quark model [7].

174 transitions involving the spin of the heavy b quark are strongly suppressed, the former states,
 175 including the $\Upsilon(5S)$, require a different explanation [10].

176 The favored explanation for the properties of $\Upsilon(5S)$, including its decays to Z_b , is based
 177 on the molecular picture, where these vector bottomonium-like resonances are assumed to
 178 contain an admixture of pairs of colored heavy mesons. This hypothesis has been successfully
 179 employed [11] to explain the decays to and the existence of the six Z_b states. However,
 180 the details of the interaction responsible for these processes are not yet fully understood.
 181 Alternative explanations include a model with a diquark-antidiquark pair, where a pair of
 182 quarks and a pair of antiquarks are each bound with a stronger force than the force holding
 183 diquark and antidiquark together. While the search described in this document is model-
 184 independent, our motivation is somewhat biased in favor of the molecular picture and has
 185 likely impacted our decisions about how to perform the analysis.

186 The main goal of our study is to test some of the predictions of the new spectroscopy [12]
 187 that predicts energy levels for the molecular bottomonium-like states depicted in Fig. 2,
 188 Namely, we describe a search for the partner states of Z_b , referred to as W_{bJ} , and we aim to
 189 obtain new information about hadronic dynamics in presence of the heavy b quarks. Improv-
 190 ing the current understanding of such dynamics is of paramount importance for being able to
 191 use the hadronic decays of B mesons to extract possible contributions from the Beyond-the-
 192 Standard-Model (BSM) amplitudes, where the interplay between the strong interaction and
 193 the new BSM weak phases could not be reliably understood without the precise theoretical

$I^G(J^P)$	Name	Co-produced with (threshold, GeV/c ²)	Assumed composition	Decay channels
1 ⁺ (1 ⁺)	$Z_b(10610)$	π (10.75)	$B\bar{B}^*$	$\Upsilon(nS)\pi, h_b(nP)\pi, \eta_b(nS)\rho$
1 ⁺ (1 ⁺)	$Z'_b(10650)$	π (10.79)	$B^*\bar{B}^*$	$\Upsilon(nS)\pi, h_b(nP)\pi, \eta_b(nS)\rho$
1 ⁻ (0 ⁺)	W_{b0}	ρ (11.34), γ (10.56)	$B\bar{B}$	$\Upsilon(nS)\rho, \eta_b(nS)\pi, \chi_{b\pi}$
1 ⁻ (0 ⁺)	W'_{b0}	ρ (11.43), γ (10.65)	$B^*\bar{B}^*$	$\Upsilon(nS)\rho, \eta_b(nS)\pi, \chi_{b\pi}$
1 ⁻ (1 ⁺)	W_{b1}	ρ (11.38), γ (10.61)	$B\bar{B}^*$	$\Upsilon(nS)\rho, \chi_{b\pi}$
1 ⁻ (2 ⁺)	W_{b2}	ρ (11.43), γ (10.65)	$B^*\bar{B}^*$	$\Upsilon(nS)\rho, \chi_{b\pi}$

Table 1: Molecular isotriplet states which could be produced in the decays of $\Upsilon(5S)$ and $\Upsilon(6S)$ according to [10]. Note that the ρ could be replaced by a photon in the decays of $I_3 = 0$ states, but this would suppress the expected rate even more. Please see Fig. 3 as well.

199 Z_b are spin-1 isotriplets (both neutral and charged states were discovered in transitions
200 $\Upsilon(nS) \rightarrow \pi Z_b$ ($n = 5, 6$). The hypothetical partners of positive G -parity states Z_b , *i.e.* the
201 W_{bJ} states, would also be isotriplets but of negative G -parity (quantum numbers of the new
202 molecular states are defined by quantum numbers of their partners in two-body decays of the
203 $\Upsilon(5S)$ parent: while Z_b is accompanied by a pion, each W_{bJ} is accompanied by a ρ meson (or
204 a photon)). Therefore the W_{bJ} states are expected to appear in transitions $\Upsilon(nS) \rightarrow \rho W_{bJ}$.
205 Conservation of angular momentum allows J in W_{bJ} to be 0, 1 or 2. Excited states such as
206 W'_{b0} could exist as well. Quantum numbers assigned to Z_b and W_{bJ} states are summarized
207 in Table 1.

208 The $\Upsilon(5S)$ resonance does not have enough energy to allow the transition to W_{bJ} with
209 sufficient amount of energy left for the two pions in the tail of the ρ invariant mass. In
210 our analysis, instead of searching for decays with the ρ mesons, we have to allow for the $q\bar{q}$
211 annihilation and pay the price of approximately α_{em} in the branching fraction:

$$\frac{\Gamma(\Upsilon(5S) \rightarrow \gamma W_{bJ})}{\Gamma(\Upsilon(5S) \rightarrow Z_b \pi)} \sim \alpha_{\text{em}} \approx \frac{1}{137} \quad (1)$$

212 Therefore, we search for the transitions $\Upsilon(5S) \rightarrow \gamma W_{bJ}$. This indirect phase space limitation
213 allows us to search only for the $I_3 = 0$ partners of the Z_b states, *i.e.* only the neutral
214 component of each isotriplet can be found in such radiative transitions. We explain this
215 strategy, suggested [13] by M.B. Voloshin, in Fig. 3.

216 To search for all new resonances expected in the new spectroscopy would require to
217 collect a sizeable data sample at $\Upsilon(6S)$ or above its energy. Such possible future studies [14]
218 at Belle II and many more interesting discussions (such as possible existence of isoscalar
219 partners of Z_b and W_{bJ}) can be found elsewhere [10]. In the rest of this paper, we focus on
220 the analysis of the full $\Upsilon(5S)$ data sample where we search for the decay $\Upsilon(5S) \rightarrow \gamma W_{bJ}$.

221 1.4 Expected Signal in Data

222 Belle previously reported [15] that charged Z_b states comprise approximately 2.54% of the
223 1819 $\Upsilon(1S)\pi^+\pi^-$ (followed by $\Upsilon(1S) \rightarrow \mu^+\mu^-$) events observed with the full data sample.

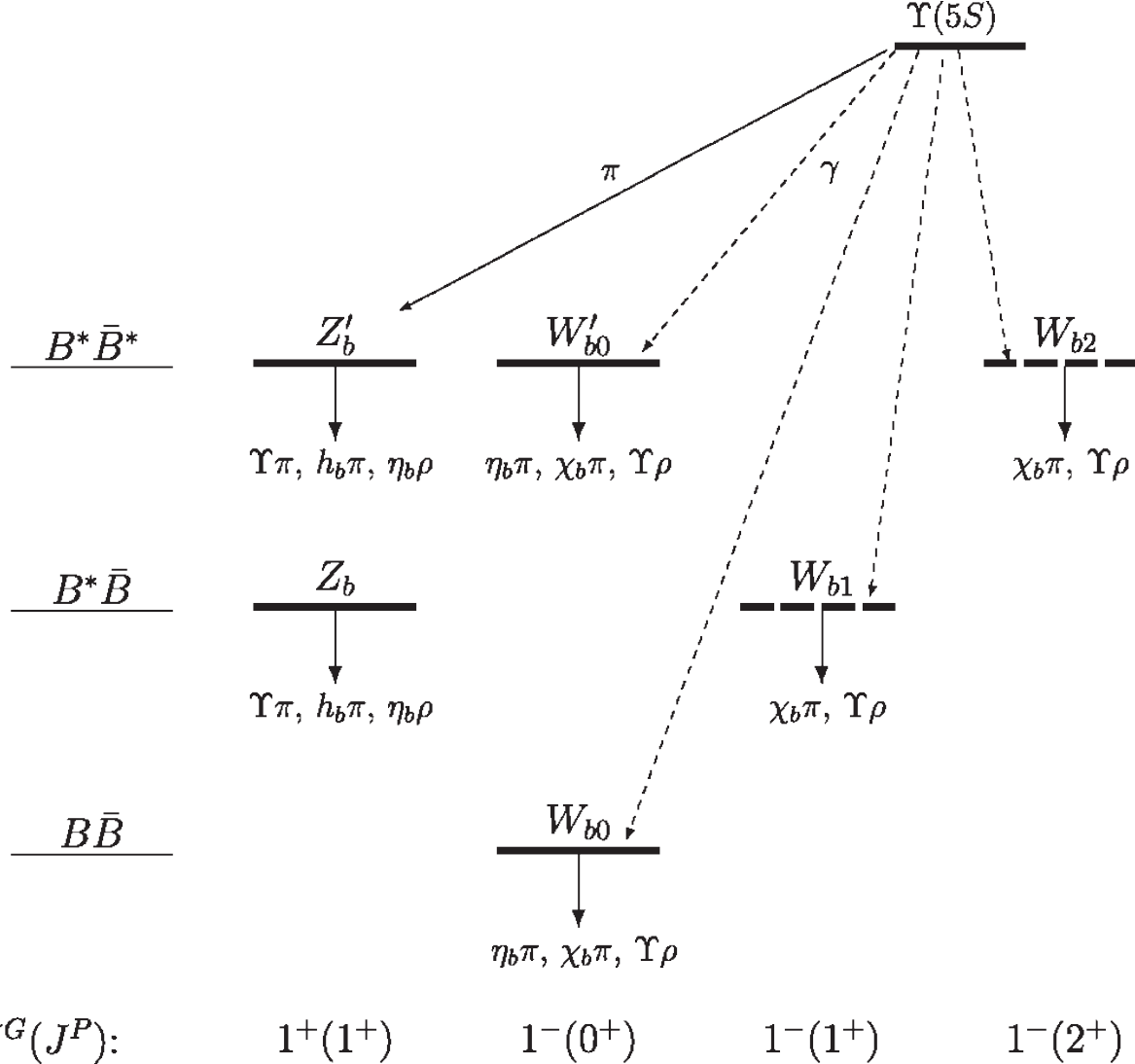


Figure 3: The expected family of isotriplet resonances from Ref. [13] (which the reader is advised to consult for relevant details). For $\Upsilon(6S)$ transitions, the photon is replaced by ρ . This would also allow to access charged W_{bJ} states. Also, please see Table 1.

224 The overall reconstruction efficiency in Z_b analysis was estimated to be around 46%. This
 225 allows us to estimate that, with an ideal, *i.e.* 100% efficient detector, we would expect to
 226 detect, approximately, 100 (charged) Z_b events.

227 While searching for W_{bj} events in radiative decays of $\Upsilon(5S)$, as elaborated in Section 1.3,
 228 we have to pay the price of α_{em} . Jumping a little bit ahead of ourselves, with our overall
 229 detection efficiency of 29%, we therefore expect to observe, on average, 0.2 W_{b0} events. This
 230 number, however, has a (hopefully very) large uncertainty, and, after all, we are (always!)
 231 driven by hope that nature might be kinder to us than we deserve. Also, tangentially, our
 232 LHC colleagues have been searching for signatures of SUSY for some time already, and, no
 233 matter how little has been observed so far, their noble quest will stop not. So why should we
 234 stop ours? On this philosophical note we conclude this discussion and proceed to describe

235 our actual analysis.

236 2 Monte Carlo and Data Samples

237 To study the properties of signal events, we generate 100,000 Monte Carlo (MC) events
 238 for $\Upsilon(5S) \rightarrow \gamma W_{bJ}$ followed by $W_{bJ} \rightarrow \Upsilon(1S)\rho^0$, $\Upsilon(1S) \rightarrow \mu^+\mu^-$, $\rho^0 \rightarrow \pi^+\pi^-$ using MC
 239 generator EvtGen [16]. Detector response is simulated using GEANT4 [17]. W_{bJ} is generated
 240 with an intrinsic width of 15 MeV, similar to the widths of Z_b and Z'_b . Table 2 displays the
 241 decay models [18] used in MC simulation of signal processes. The PHOTOS package [19] is
 242 used to simulated final state radiation (FSR). To allow for softer FSR photons in simulation,
 243 we modified the PHOTOS package to lower the minimum energy of final state radiation.
 244 Please see Section 10.1 for details.

245 We use six streams of generic MC to study background events. Each stream is equivalent
 246 to a full Belle data sample of 121.4 fb^{-1} of $\Upsilon(5S)$ resonance data. We generate additional MC
 247 samples to study background events originating from $\Upsilon(5S) \rightarrow \Upsilon(1S)\pi^+\pi^- \rightarrow \mu^+\mu^-\pi^+\pi^-$
 248 with initial state radiation (ISR) as well as events originating from $\Upsilon(5S) \rightarrow Z_b^\pm\pi^\mp \rightarrow$
 249 $\Upsilon(1S)\pi^\pm\pi^\mp \rightarrow \mu^+\mu^-\pi^\pm\pi^\mp$. We describe our studies of these processes in Section 6 and
 250 Section 7, respectively.

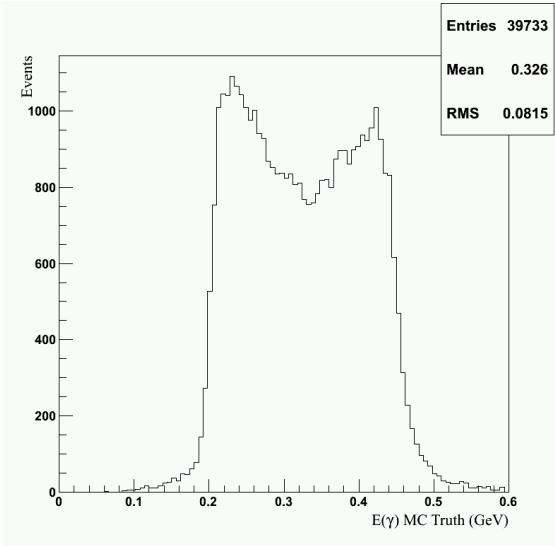
251 In this analysis, we use the full 121.4 fb^{-1} of on-resonance $\Upsilon(5S)$ data collected by the
 252 Belle detector at the KEKB collider from asymmetric energy e^+e^- collisions with $\sqrt{s} = 10.86$
 253 GeV [20].

Decay Process	Decay Model used in Mote Carlo Simulation
$\Upsilon(5S) \rightarrow W_{bJ}\gamma$	VSP_PWAVE
$W_{bJ} \rightarrow \Upsilon(1S)\rho^0$	SVV_HELAMP
$\rho^0 \rightarrow \pi^+\pi^-$	VSS
$\Upsilon(1S) \rightarrow \mu^+\mu^-$	VLL
Final state radiation	PHOTOS (modified)

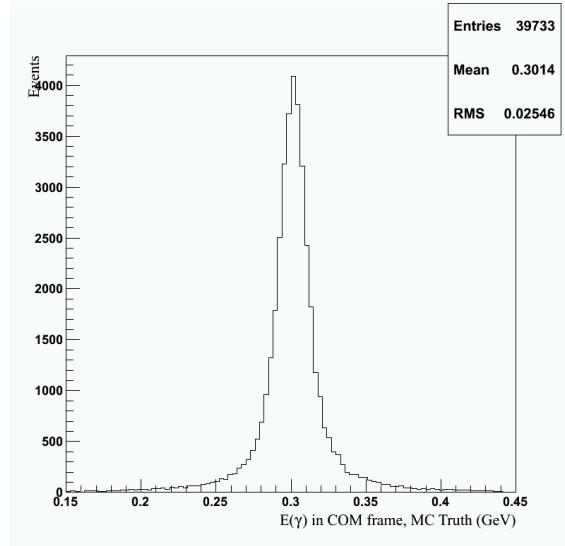
Table 2: EvtGen decay models used in Mote Carlo simulation of signal processes.

254 3 Selection Criteria

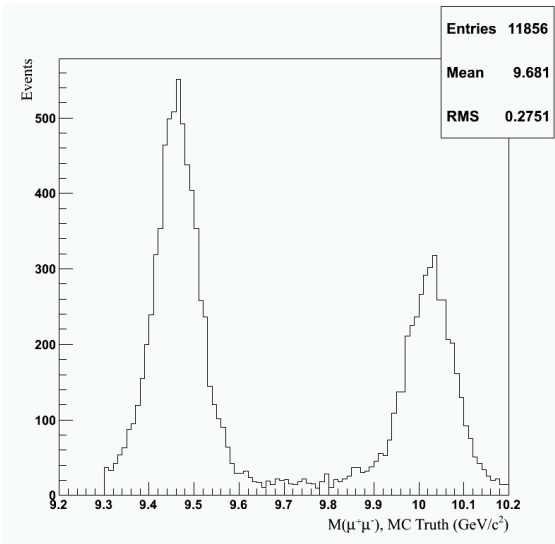
255 We reconstruct the decay mode $\Upsilon(5S) \rightarrow \gamma W_{bJ}$ followed by the decays $W_{bJ} \rightarrow \Upsilon(1S)\rho^0$,
 256 $\Upsilon(1S) \rightarrow \mu^+\mu^-$, $\rho^0 \rightarrow \pi^+\pi^-$. We select a fully-reconstructed final state particle combination
 257 consisting of $\pi^+\pi^-\mu^+\mu^-\gamma$. **The selection criteria that follow, though not systematically**
 258 **optimized, are based on MC truth distributions and typical choices made in previous Belle**
 259 **analyses.**



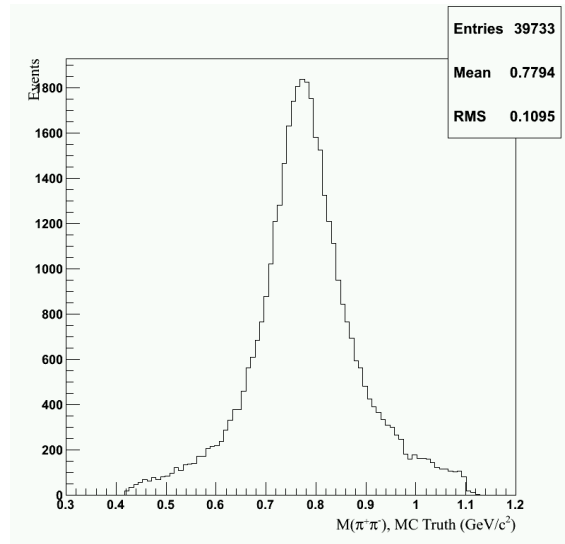
(a) Photon energy in the lab frame for events in signal MC.



(b) Photon energy in the COM frame for events in signal MC.



(c) $M(\mu^+\mu^-)$ for events in generic MC. The left peak is $\Upsilon(1S)$ and the right peak is $\Upsilon(2S)$. Note that the right tail of $\Upsilon(1S)$ overlaps with the left tail of $\Upsilon(2S)$.



(d) $M(\pi^+\pi^-)$ for events in signal MC.

Figure 4: Various MC distributions which informed our selection criteria.

260 3.1 Selection of Photon Candidates

261 We require reconstructed photons have energy between 100 and 600 MeV (in the lab frame)
 262 and polar angle between 17° and 150° . In the center of mass reference frame, the radiative
 263 photon is expected to be monochromatic with energy of approximately 300 MeV. To reject
 264 showers produced by neutral hadrons, we require $E_9/E_{25} > 0.75$, where the E_9/E_{25} ratio is
 265 defined as the energy summed in the 3×3 array of crystals surrounding the center of the

266 shower (E_9) to that of the 5 x 5 array of crystals surrounding the center of the shower (E_{25}).
267 See Fig. 4a and Fig. 4b for relevant distributions.

268 3.2 Selection of Pion and Muon Candidates

269 Pion candidates must satisfy $R_{K,\pi} < 0.9$, where $R_{K,\pi}$ is the “Kaon identification variable”
270 defined as the likelihood ratio of the charged track to be due to a kaon versus a pion, and
271 $R_{e,\text{hadron}} < 0.9$, where $R_{e,\text{hadron}}$ is the likelihood ratio of the charged track to be due to
272 an electron versus a hadron. Similarly, muon candidates must satisfy $R_\mu > 0.1$, where
273 R_μ is the likelihood ratio of the charged track to be due to a muon versus other particles
274 detected by the KLM detector subsystem. After imposing the aforementioned requirements,
275 we additionally require there to be four unique charged tracks – two pions and two muons.
276 Events with more than four such tracks are rejected.

277 To select reconstructed tracks that originate near the interaction point, we require pion
278 and muon candidates have $dr < 0.3$ cm and $|dz| < 2$ cm, where dr and dz are impact
279 parameters in the radial and z directions, respectively. We also require pion and muon
280 candidates to have transverse momenta $p_T > 100$ MeV. Candidate muon pairs must have
281 an invariant mass between $9.3 \text{ GeV}/c^2$ and $9.6 \text{ GeV}/c^2$. Candidate pion pairs must have an
282 invariant mass between $0.42 \text{ GeV}/c^2$ and $1.02 \text{ GeV}/c^2$. See Fig. 4c and Fig. 4d for relevant
283 distributions.

284 3.3 Selection of $\Upsilon(5S)$ Candidates

285 $\Upsilon(5S)$ candidates are required to have an invariant mass between 10.2 GeV and 11.5 GeV.
286 The muon pairs of selected $\Upsilon(5S)$ candidates are mass constrained to the nominal $\Upsilon(1S)$
287 invariant mass of $9.460 \text{ GeV}/c^2$. A summary of our selection criteria is shown in Table 3.

288 3.4 Best Candidate Selection

289 Approximately 32% of signal MC events satisfying our selection criteria have multiple signal
290 candidates. This is exclusively due to relatively soft photons. In events with multiple signal
291 candidates, we select the candidate that has an energy most consistent with the center of
292 mass energy of the experimental run. The selected candidates are correctly MC-tagged to full
293 MC truth for signal 90% of the time. For fully reconstructed signal MC events with multiple
294 candidates, our best candidate selection method selects a candidate correctly MC-tagged to
295 full MC truth 88% of the time.

296 4 Signal Monte Carlo Studies

297 4.1 Signal Monte Carlo Distributions

298 To understand properties of signal events, we investigate two invariant mass variables,
299 $M(\pi^+\pi^-(\mu^+\mu^-)_{\text{fit}})$ and $M_{\text{rec}}(\gamma)$, where subscript “fit” indicates that the muon pair is con-
300 strained to the nominal mass of $\Upsilon(1S)$. We define the invariant mass recoiling against X
301 as

Particle Candidate	Selection Criteria
γ	$100 \text{ MeV} \leq E(\gamma) \leq 600 \text{ MeV}$ $20 \text{ MeV} \leq E(\gamma) \leq 5000 \text{ MeV}$
π^\pm, μ^\pm	$dr < 0.3 \text{ cm}$ $dr < 0.4 \text{ cm}$ $dz < 2 \text{ cm}$ $ dz < 4 \text{ cm}$ $p_T > 100 \text{ MeV}/c$
π^\pm PID	$R_{K,\pi} < 0.9$ $R_{e,hadron} < 0.9$
μ^\pm	$R_\mu > 0.10$
ρ^0	$0.420 \text{ GeV}/c^2 < M_{\pi^+\pi^-} < 1.020 \text{ GeV}/c^2$
$\Upsilon(1S)$	$9.3 \text{ GeV}/c^2 < M_{\mu^+\mu^-} < 9.6 \text{ GeV}/c^2$
$\Upsilon(5S)$	$10.2 \text{ GeV}/c^2 < M_{\pi^+\pi^-\mu^+\mu^-\gamma} < 11.5 \text{ GeV}/c^2$ $-0.05 \text{ GeV} < \Delta E < 0.03 \text{ GeV}$
(full event reconstruction)	Exactly four tracks: two muons and two pions

Table 3: Selection criteria for $\Upsilon(5S) \rightarrow \gamma W_{bJ}$

$$M_{\text{rec}}(X) = \sqrt{(E_{\text{cm}}(\text{exp}) - E_{\text{cm}}(X))^2 - |\vec{0} - \vec{p}_{\text{cm}}(X)|^2} \quad (2)$$

302 where $E_{\text{cm}}(\text{exp})$ is the run's average energy, and $E_{\text{cm}}(X)$ and $\vec{p}_{\text{cm}}(X)$ are the energy and
303 momentum of system X . Subscript "cm" is used for quantities evaluated in the center of
304 mass reference frame of the experiment. For signal events, $M_{\text{rec}}(\gamma)$ and $M(\pi^+\pi^-(\mu^+\mu^-)_{\text{fit}})$
305 are two independent ways to estimate the invariant mass of W_{bJ} . Fully reconstructed signal
306 events fall along the main diagonal of the $M(\pi^+\pi^-(\mu^+\mu^-)_{\text{fit}})$ vs $M_{\text{rec}}(\gamma)$ plot shown in Fig. 5.
307 We define energy balance ΔE as

$$\Delta E = E_{\text{cm}}(\pi^+\pi^-(\mu^+\mu^-)_{\text{fit}}\gamma) - E_{\text{cm}}(\text{exp}). \quad (3)$$

308 ΔE is the most important variable we can use to select fully reconstructed signal event
309 candidates.

310 There are two effects contributing to the observed width of $M(\pi^+\pi^-(\mu^+\mu^-)_{\text{fit}})$: (1) the
311 intrinsic width of W_{bJ} , and (2) the charged track reconstruction. Fig. 6 shows $M(\pi^+\pi^+\mu^+\mu^-)$
312 and $M(\pi^+\pi^-(\mu^+\mu^-)_{\text{fit}})$ resolutions for signal events within the signal region and sideband
313 regions (defined in Section 4.2). We model both resolutions as the sum of two Gaussians
314 with the same mean and fit both resolutions. Contribution to $M(\pi^+\pi^-(\mu^+\mu^-)_{\text{fit}})$ resolution
315 from charged track reconstruction is primarily due to pions, since muon pairs are constrained
316 to $\Upsilon(1S)$ invariant mass.

317 The distribution of $M_{\text{rec}}(\gamma)$ has a long tail due to an underestimation of photon energy,
318 causing an overestimation of $M_{\text{rec}}(\gamma)$. Effects contributing to the observed width of $M_{\text{rec}}(\gamma)$
319 include (1) intrinsic width of W_{bJ} , and (2) photon energy resolution. $M_{\text{rec}}(\gamma)$ resolution is
320 dominated by photon energy resolution.

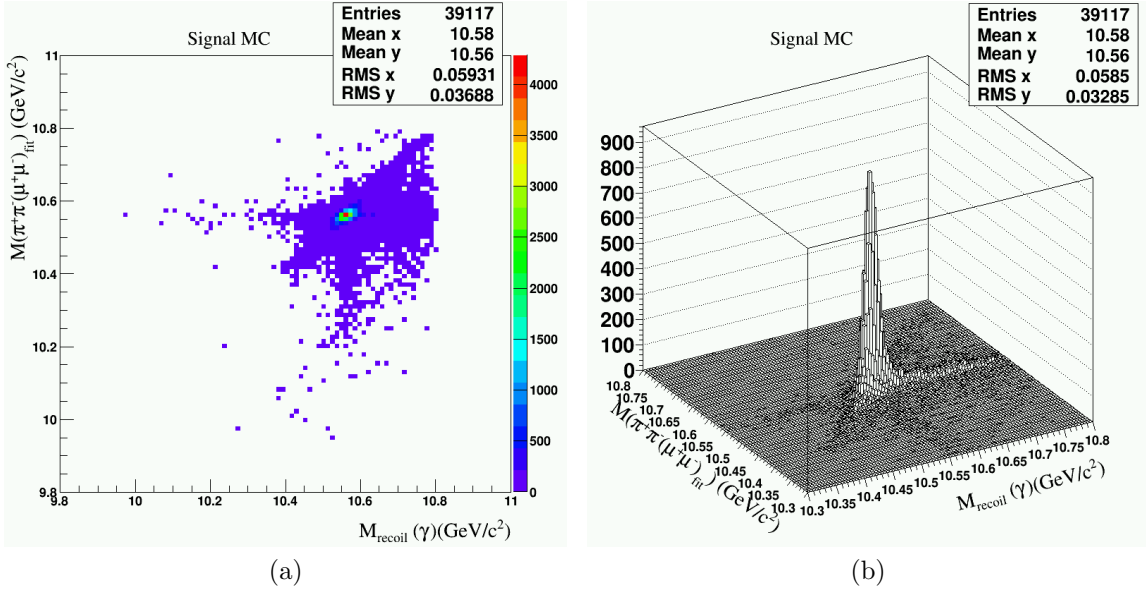
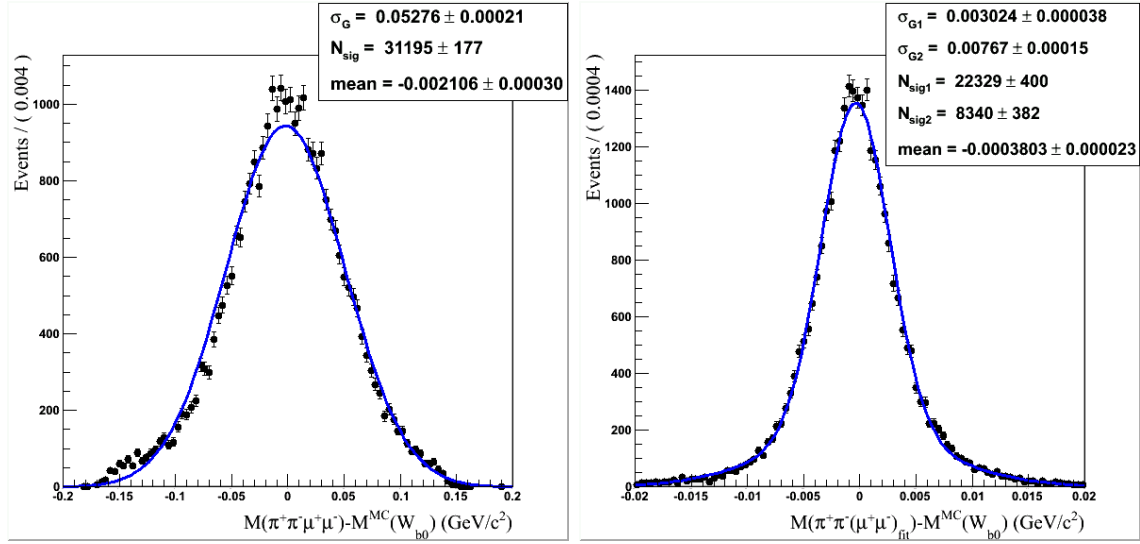


Figure 5: $M(\pi^+\pi^-(\mu^+\mu^-)_{\text{fit}})$ vs $M_{\text{rec}}(\gamma)$ distribution for W_{B0} signal MC events. We show the lego plot in Fig. 5b to emphasize that the tail of $M_{\text{rec}}(\gamma)$ is not as large as it appears in Fig. 5a. Note that Fig. 5b is plotted in a smaller range.

Quantity	Value
Intrinsic width of W_{bJ}	15 MeV/ c^2
Charged track resolution	4 MeV
Photon energy resolution	8 MeV
Beam energy resolution	6 MeV

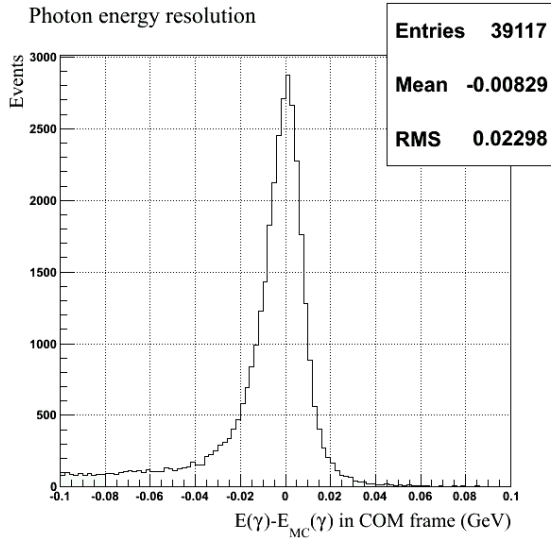
Table 4: Quantities contributing to widths of measured quantities

321 Effects contributing to the observed shape of ΔE include (1) photon energy resolution, (2)
 322 charged track resolution, (3) beam energy resolution, and (4) the intrinsic width of W_{bJ} . ΔE
 323 resolution is dominated by photon energy resolution as well. The values of relevant widths
 324 are listed in Table 4. In signal MC we observe $\sigma_{\Delta E} \approx 12$ MeV, so we take advantage of this
 325 excellent energy resolution to select fully reconstructed events. Because the distribution of
 326 ΔE is asymmetric (primarily due to leakage from the calorimeter and relatively soft non-
 327 signal photons in signal events), we use an asymmetric selection and require $-0.05 \text{ GeV} \leq$
 328 $\Delta E \leq 0.03 \text{ GeV}$. This selection cuts out the long tail in the distribution of $M_{\text{rec}}(\gamma)$ and
 329 reduces the efficiency by 20%. Note, however, that this selection primarily removes events
 330 where the signal photon is not reconstructed. After applying this selection on ΔE , signal
 331 reconstruction efficiency becomes approximately 31%. Fig. 7 displays ΔE resolution as well
 332 as quantities contributing to ΔE resolution.

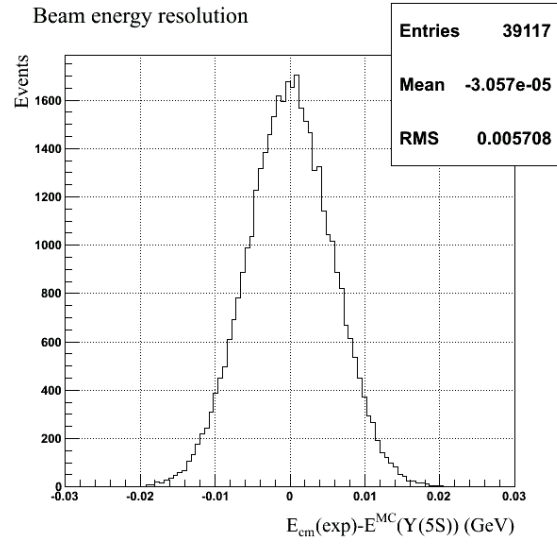


(a) $M(\pi^+\pi^+\mu^+\mu^-)$ resolution. Note that muons are not mass constrained. (b) $M(\pi^+\pi^-(\mu^+\mu^-)_{\text{fit}})$ resolution (muons are mass constrained).

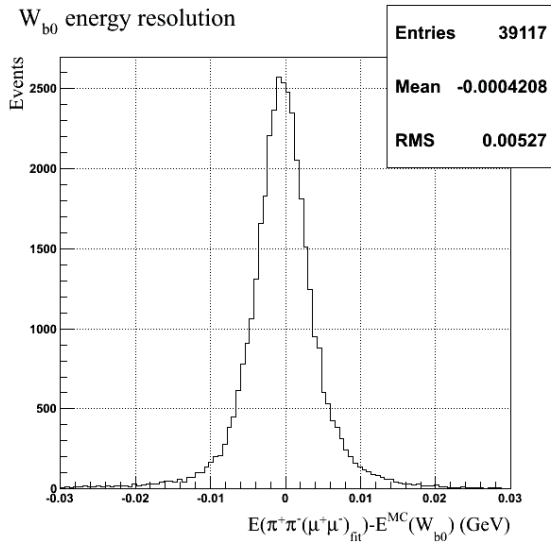
Figure 6: $M(\pi^+\pi^+\mu^+\mu^-)$ and $M(\pi^+\pi^-(\mu^+\mu^-)_{\text{fit}})$ resolutions for signal events within the signal region and sideband regions (defined in Section 4.2). Note that the horizontal scales are different.



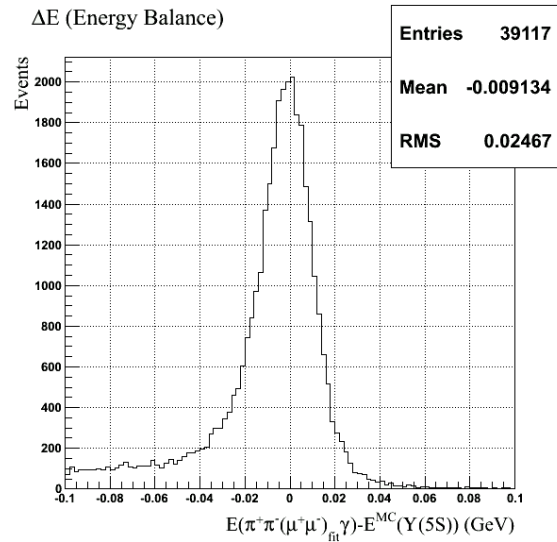
(a) Signal photon energy line shape in the COM reference frame.



(b) Beam energy resolution.



(c) $M(\pi^+\pi^-(\mu^+\mu^-)_{\text{fit}})$ energy line shape (includes the effect of intrinsic W_{bJ} width and charged track reconstruction).



(d) Signal candidate energy line shape. Includes the effects of W_{bJ} intrinsic width and resolution.

Figure 7: ΔE resolution and quantities contributing to ΔE resolution.

333 4.2 Description of the Signal Region

334 Table 5 contains the definitions of four important regions in this analysis. Before investigating
 335 data, we blind the region where we expect to find signal. We refer to this region as the
 336 blinded region. The invariant masses of W_{b0} , W_{b1} , and W'_{b0} and W_{b2} are expected to be at
 337 the $B\bar{B}$, $B^*\bar{B}$, and $B^*\bar{B}^*$ thresholds, respectively. The blinded region is defined as the region
 338 between the $B\bar{B}$ and $B^*\bar{B}^*$ thresholds plus an additional margin of 70 MeV on either side.
 339 This corresponds to $10.49 \text{ GeV}/c^2 \leq M(\pi^+\pi^-(\mu^+\mu^-)_{\text{fit}}) \leq 10.72 \text{ GeV}/c^2$. The boundary on

Region Name	Boundary Definitions
Blinded Region	$10.49 \text{ GeV}/c^2 \leq M(\pi^+\pi^-(\mu^+\mu^-)_{\text{fit}}) \leq 10.72 \text{ GeV}/c^2$ $M_{\text{rec}}(\gamma) \geq M(\pi^+\pi^-(\mu^+\mu^-)_{\text{fit}}) - 0.04 \text{ GeV}/c^2$ $M_{\text{rec}}(\gamma) \leq 10.8 \text{ GeV}/c^2$
Signal Region	$10.49 \text{ GeV}/c^2 \leq M(\pi^+\pi^-(\mu^+\mu^-)_{\text{fit}}) \leq 10.72 \text{ GeV}/c^2$ $-0.05 \text{ GeV} \leq \Delta E \leq 0.03 \text{ GeV}$
Sideband Region	$10.38 \text{ GeV}/c^2 \leq M(\pi^+\pi^-(\mu^+\mu^-)_{\text{fit}}) \leq 10.49 \text{ GeV}/c^2$ $10.72 \text{ GeV}/c^2 \leq M(\pi^+\pi^-(\mu^+\mu^-)_{\text{fit}}) \leq 10.80 \text{ GeV}/c^2$ $-0.05 \text{ GeV} \leq \Delta E \leq 0.03 \text{ GeV}$.
Grand Sideband Region	$10.38 \text{ GeV}/c^2 \leq M(\pi^+\pi^-(\mu^+\mu^-)_{\text{fit}}) \leq 10.80 \text{ GeV}/c^2$ $-0.20 \text{ GeV} \leq \Delta E \leq 0.20 \text{ GeV}$

Table 5: Definitions of the signal region and other important regions.

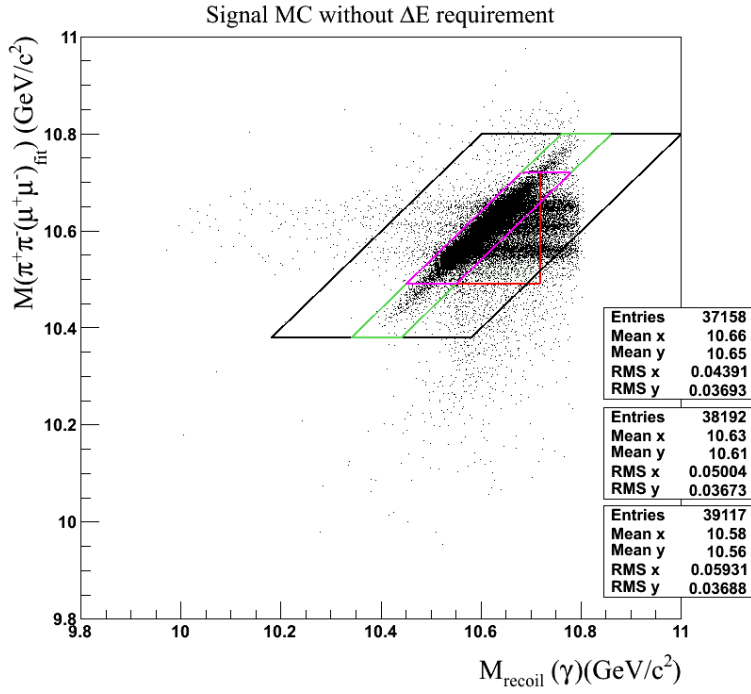
340 the left side of the region is defined by the sloped line $M_{\text{rec}}(\gamma) \geq M(\pi^+\pi^-(\mu^+\mu^-)_{\text{fit}}) - 0.04$
341 GeV/c^2 which lies parallel to the main diagonal. Approximately 20% of signal events are
342 located in the long right tail of the distribution of $M_{\text{rec}}(\gamma)$. A phase space boundary on
343 the right side of the plot at $M_{\text{rec}}(\gamma) \approx 10.75 \text{ GeV}/c^2$ forces this long tail of the $M_{\text{rec}}(\gamma)$
344 distribution into a smaller region for the higher mass W_{bJ} states. Hence, we do not define
345 a sloped boundary line as the right side of the signal region – a diagonal boundary would
346 exclude more signal events for the lower mass states because of the aforementioned phase
347 space boundary compressing the tail. Instead, we define the vertical line boundary $M_{\text{rec}}(\gamma) \leq$
348 $10.72 \text{ GeV}/c^2$ which assures that approximately equal percentages of signal would be blinded
349 for all masses of W_{bJ} states.

350 We define the signal region as the region contained within $10.49 \text{ GeV}/c^2 \leq M(\pi^+\pi^-(\mu^+\mu^-)_{\text{fit}}) \leq$
351 $10.72 \text{ GeV}/c^2$ satisfying $-0.05 \text{ (GeV)} \leq \Delta E \leq 0.03 \text{ GeV}$. The ΔE requirement selects only
352 fully-reconstructed signal events, where signal is peaking.

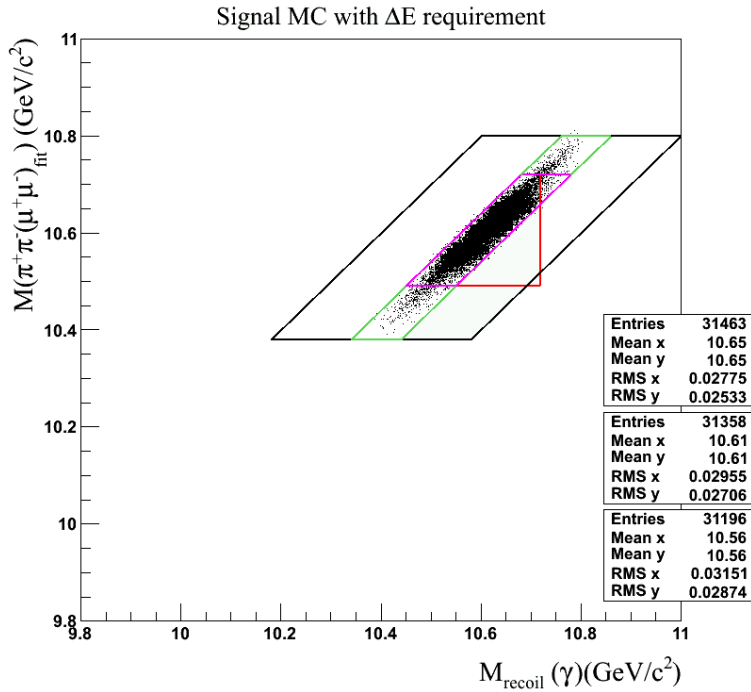
353 The sideband region is essentially an extension of the signal region, defined as the
354 regions within $10.38 \text{ GeV}/c^2 \leq M(\pi^+\pi^-(\mu^+\mu^-)_{\text{fit}}) \leq 10.49 \text{ GeV}/c^2$ and $10.72 \text{ GeV}/c^2 \leq$
355 $M(\pi^+\pi^-(\mu^+\mu^-)_{\text{fit}}) \leq 10.80 \text{ GeV}/c^2$ satisfying $-0.05 \text{ (GeV)} \leq \Delta E \leq 0.03 \text{ GeV}$.

356 We additionally define the grand sideband region as the region within $10.38 \text{ GeV}/c^2 \leq$
357 $M(\pi^+\pi^-(\mu^+\mu^-)_{\text{fit}}) \leq 10.80 \text{ GeV}/c^2$ satisfying $-0.20 \text{ GeV} \leq \Delta E \leq 0.20 \text{ GeV}$. This region is
358 used when studying background in data.

359 Fig. 8 displays these four regions with our three signal MC samples. It is important to
360 note that the blinded region is not completely contained within the grand sideband region
361 and the signal region is not completely contained within the blinded region. This is due to
362 historical reasons, as the blinded region was defined prior to the use of ΔE in this analysis.



(a) Does not include ΔE requirement.



(b) Includes ΔE requirement.

Figure 8: The blinded region (red), signal region (magenta), sideband region (green), and the grand sideband region (black). The plot in 8a includes the aforementioned ΔE requirement, while the plot in 8b does not. From top to bottom, the statistics boxes correspond to W'_{b0} , W_{b1} , and W_{b0} signal MC, respectively.

363 4.3 Trigger Simulation

364 Relatively low final state particle multiplicity of our signal events requires us to investigate
365 trigger efficiency. Trigger efficiency is simulated after full reconstruction. We find correlations
366 between trigger efficiency and kinematics. Fig. 9 shows various 2-dimensional distributions
367 of $\mu^+ \cos(\theta)$ vs $\mu^- \cos(\theta)$, and we see that events failing to satisfy trigger are more likely
368 to have one of the muons at a small angle with respect to the beam axis ($|\cos(\theta)| \geq 0.8$).
369 Fig. 10 shows additional distributions of $\mu^+ \cos(\theta)$ vs $\mu^+ \cos(\theta)$ which we use to determine
370 trigger efficiencies. When neither muon is at a small angle with respect to the beam axis,
371 trigger efficiency is 96%. When one of the muons is at a small angle with respect to the beam
372 axis, trigger efficiency drops to 89%. For all generated signal MC events, trigger efficiency is
373 approximately 94%. After accounting for trigger efficiency, our overall efficiency drops from
374 31% to 29%.

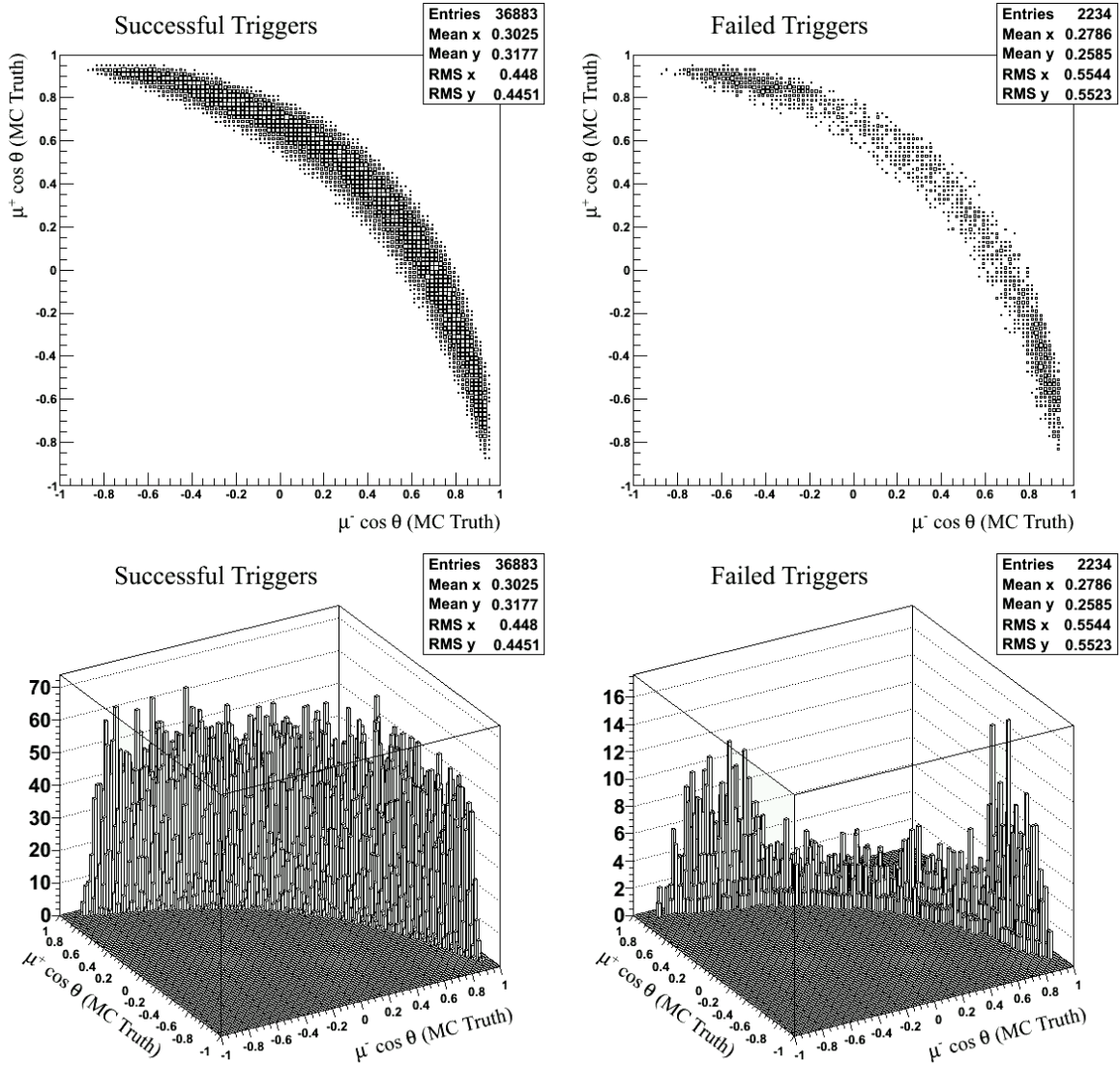


Figure 9: Reconstructed signal MC events that satisfy the offline trigger selection are plotted on the left, while events that fail the offline trigger selection are plotted on the right. We observe that events satisfying the trigger criteria are distributed more or less uniformly for kinematically allowed muons, but events failing to satisfy trigger are more likely to have one of the muons at a small angle with respect to the beam axis.

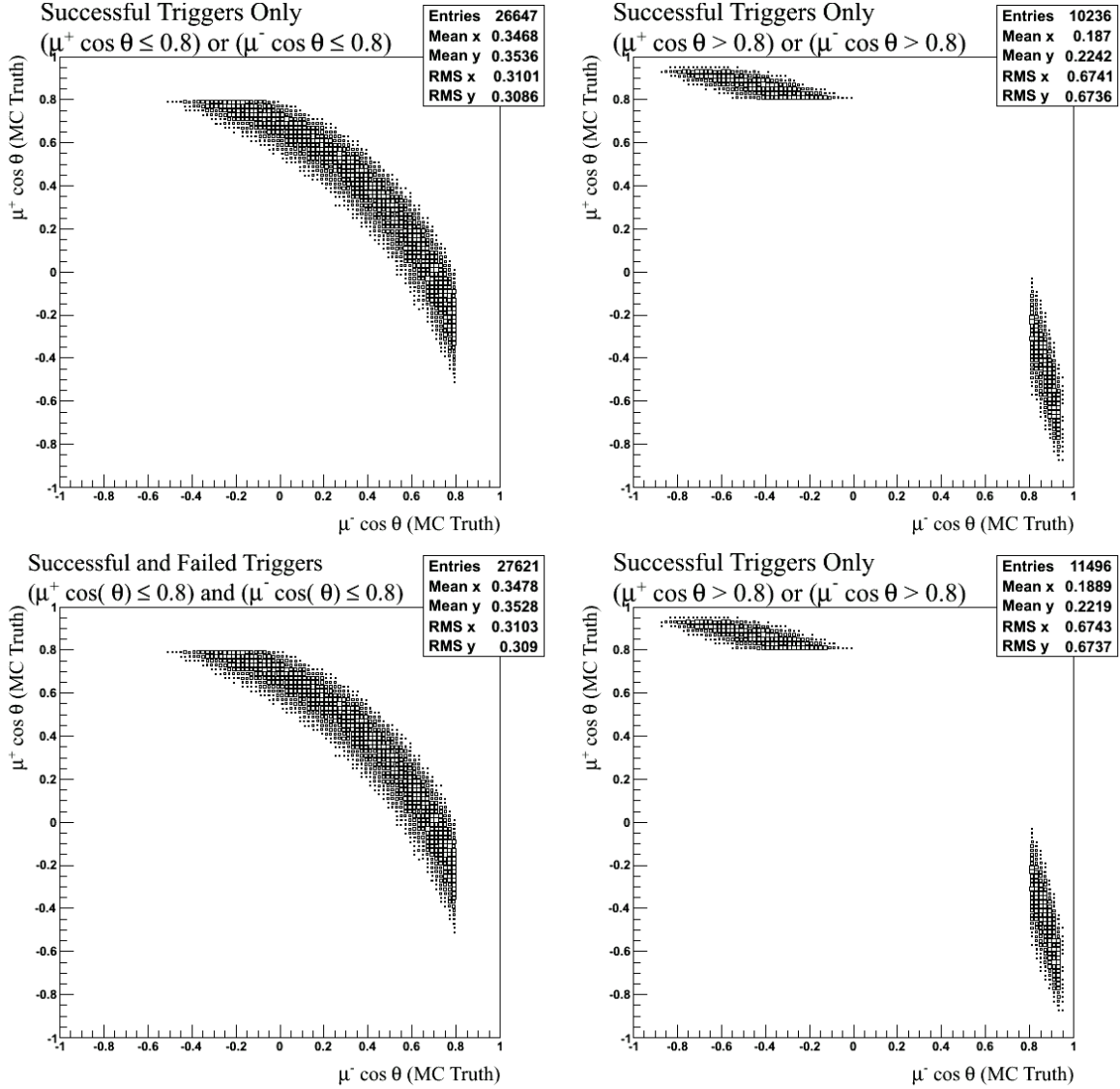


Figure 10: All reconstructed events in which both muons are generated with $|\cos(\theta)| < 0.8$ are plotted in the left two figures. Trigger efficiency for such events is approximately $(96 \pm 4)\%$. In the right two figures, we plot all reconstructed events where one of the muons is generated with $|\cos(\theta)| > 0.8$. Trigger efficiency for these events is reduced to about $(89 \pm 4)\%$.

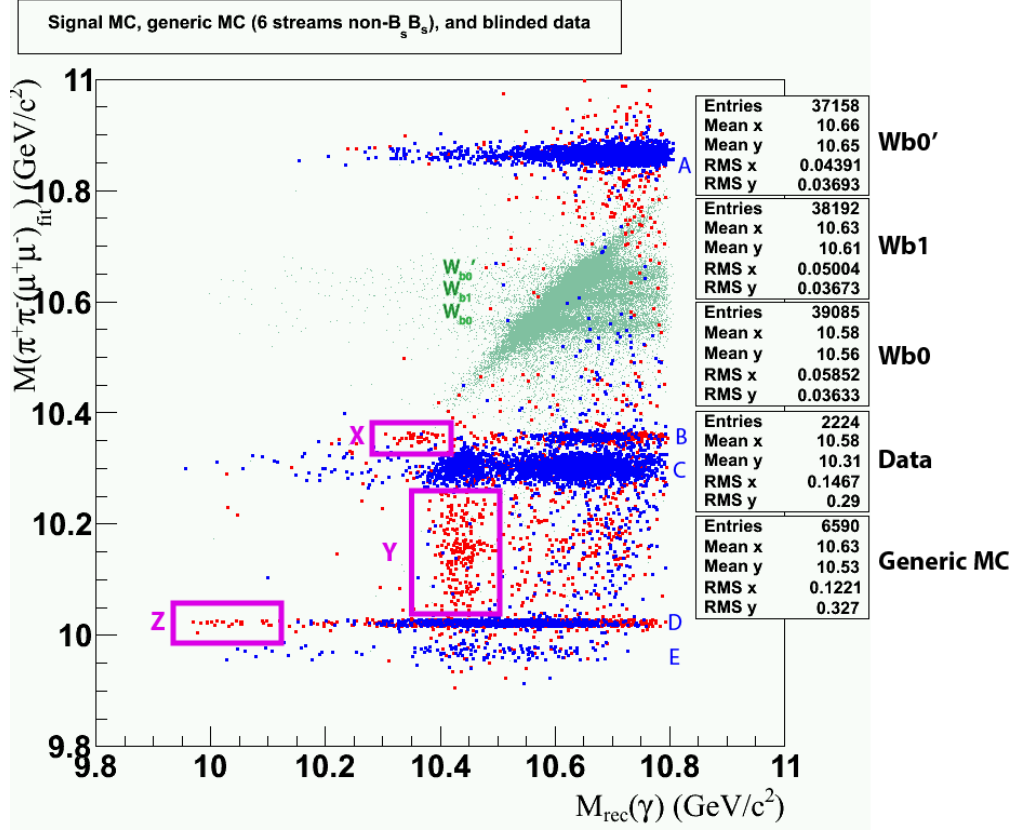


Figure 11: W_{b0} , W_{b1} , and W'_{b0} signal MC (light green), six streams of non- $B_s B_s$ generic MC (blue), and data with the signal region blinded (red).

5 Background Studies

5.1 Generic Monte Carlo and Blinded Data

Fig. 11 shows the distribution of $M(\pi^+\pi^-(\mu^+\mu^-)_{\text{fit}})$ vs $M_{\text{rec}}(\gamma)$ for generic MC and blinded data events. Using MC truth, we identify the background decays in generic MC and blinded data and group them into eight categories which are defined in Table 6. No uds , charm, or $B_s B_s$ generic MC events pass our selection criteria. A large number of non- $B_s B_s$ events do satisfy our selection criteria, though they fall primarily outside the signal region. The ΔE requirement excludes most of these background events. The most prominent non- $B_s B_s$ background sources are (cascade) dipion transitions to $\Upsilon(1S)$. We observe an enhancement in generic MC within the blinded region due to the decay $\Upsilon(5S) \rightarrow \Upsilon(2S)\pi^+\pi^-$, $\Upsilon(2S) \rightarrow \Upsilon(1S)\pi^+\pi^-$ where the selected signal pion candidates did not come from the same parent. The enhancement is removed when the ΔE constraint is applied, as such background events are not fully reconstructed.

We observe several regions where data events are clustering but generic MC events are not, and we have identified the likely origins of these events. The regions labeled X and Z in Fig. 11 are populated by events which are due to radiative returns to a lower mass $\Upsilon(nS)$ where the radiative photon is selected as our signal photon candidate. These events are

Label	Background
A	$\Upsilon(5S) \rightarrow \Upsilon(1S)\pi^+\pi^- \rightarrow \mu^+\mu^-\pi^+\pi^-$
B	$\Upsilon(5S) \rightarrow \Upsilon(3S)\pi^+\pi^- \rightarrow \Upsilon(1S)\pi^+\pi^-\pi^+\pi^- \rightarrow \mu^+\mu^-\pi^+\pi^-\pi^+\pi^-$ $\Upsilon(5S) \rightarrow \Upsilon(3S)\pi^0\pi^0 \rightarrow \Upsilon(1S)\pi^+\pi^-\pi^0\pi^0 \rightarrow \mu^+\mu^-\pi^+\pi^-\pi^0\pi^0$
C	$\Upsilon(5S) \rightarrow \Upsilon(2S)\pi^+\pi^- \rightarrow \Upsilon(1S)\pi^+\pi^-\pi^+\pi^- \rightarrow \mu^+\mu^-\pi^+\pi^-\pi^+\pi^-$ $\Upsilon(5S) \rightarrow \Upsilon(2S)\pi^+\pi^- \rightarrow \Upsilon(1S)\pi^0\pi^0\pi^+\pi^- \rightarrow \mu^+\mu^-\pi^0\pi^0\pi^+\pi^-$
D	$\Upsilon(5S) \rightarrow \Upsilon(2S)\pi^0\pi^0 \rightarrow \Upsilon(1S)\pi^+\pi^-\pi^0\pi^0 \rightarrow \mu^+\mu^-\pi^+\pi^-\pi^0\pi^0$
E	$\Upsilon(5S) \rightarrow \Upsilon(3S)\pi^+\pi^- \rightarrow \Upsilon(1S)\pi^0\pi^0\pi^+\pi^- \rightarrow \mu^+\mu^-\pi^0\pi^0\pi^+\pi^-$
X	$e^+e^- \rightarrow \Upsilon(3S)\gamma \rightarrow \Upsilon(1S)\pi^+\pi^-\gamma \rightarrow \mu^+\mu^-\pi^+\pi^-\gamma$
Y	Various processes involving $\chi_{bJ}(1P) \rightarrow \gamma\Upsilon(1S)$, <i>e.g.</i> $\Upsilon(5S) \rightarrow \Upsilon(1D)\pi^+\pi^-$, where $\Upsilon(1D) \rightarrow \gamma\chi_{bJ}(1P)$
Z	$e^+e^- \rightarrow \Upsilon(2S)\gamma \rightarrow \Upsilon(1S)\pi^+\pi^-\gamma \rightarrow \mu^+\mu^-\pi^+\pi^-\gamma$

Table 6: Backgrounds labeled in Fig. 11.

392 fully reconstructed, and thus fall along the main diagonal of the plot. The region labeled
393 Y includes processes involving radiative decays of $\chi_{bJ}(1P)$. These events have additional
394 final state particles that are not reconstructed, and hence they fall below the main diagonal
395 where $\Delta E < 0$. Events in categories X, Y, and Z are not of concern to us, since they are
396 located far from the signal region.

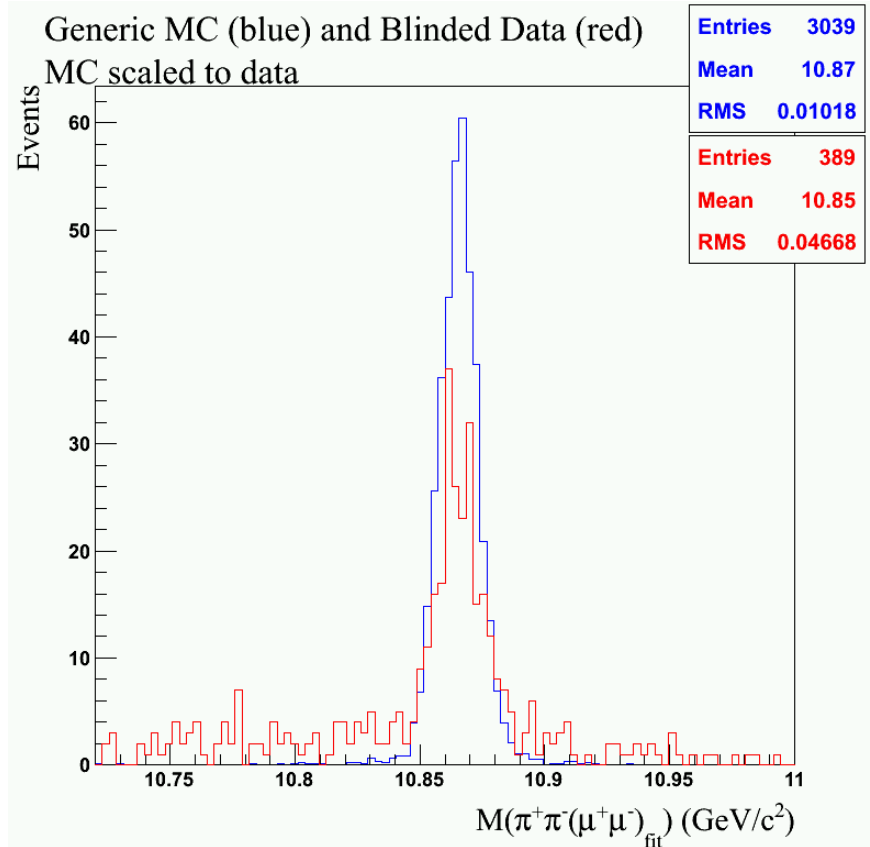


Figure 12: $M(\pi^+\pi^-(\mu^+\mu^-)_{\text{fit}})$ distributions for $\Upsilon(5S) \rightarrow \Upsilon(1S)\pi^+\pi^-$ events (label 'A' in Table 6). Distributions for generic MC and blinded data are shown in blue and red, respectively. Generic MC does not include ISR and is normalized to the number of data events shown in the plotted range. We choose $10.72 \text{ GeV}/c^2$ as the lower limit of the range plotted, since lower masses would include the blinded region.

397 6 Background from $\Upsilon(5S) \rightarrow \Upsilon(1S)\pi^+\pi^-$ with Initial 398 State Radiation (ISR)

399 We find that dipion transitions to $\Upsilon(1S)$ (labeled 'A' in Fig. 11) have a much longer tail
400 in data than in generic MC. This difference is shown in Fig. 12, and is due to initial state
401 radiation (ISR). This tail contaminates the signal region, so we generate additional MC
402 samples with ISR to study these backgrounds.

403 6.1 $\Upsilon(5S) \rightarrow \Upsilon(1S)\pi^+\pi^-$ ISR Monte Carlo Sample

404 The VectorISR model [18] is used to simulate ISR. We reweight the ISR photon energy
405 spectrum according to the correct radiator function up to order α^2 [21] using a Monte Carlo
406 method. After reweighting, there are approximately 110,000 events in our MC sample. A
407 distribution of the reweighted ISR spectrum is shown in Fig. 13.

408 Fig. 14 shows the $M(\pi^+\pi^-(\mu^+\mu^-)_{\text{fit}})$ vs $M_{\text{rec}}(\gamma)$ distribution for reweighted $\Upsilon(5S) \rightarrow$

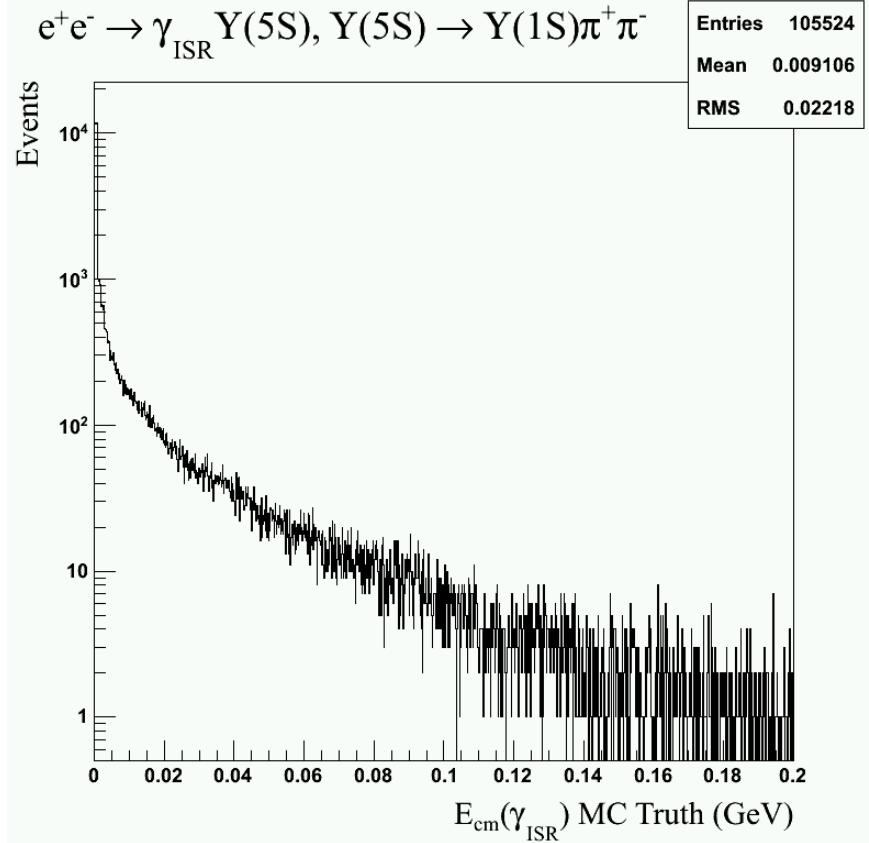


Figure 13: Reweighted ISR energy spectrum for $e^+e^- \rightarrow \gamma_{\text{ISR}}\Upsilon(5S), \Upsilon(5S) \rightarrow \Upsilon(1S)\pi^+\pi^-$. Note that a log scale is used for the vertical axis.

409 $\Upsilon(1S)\pi^+\pi^-$ events with ISR. Recall that the two plotted variables represent two independent
 410 ways to estimate the invariant mass of W_{bJ} , and therefore fully reconstructed events fall along
 411 the main diagonal of this plot. When the ISR photon of these backgrounds is selected as
 412 the signal photon candidate, these backgrounds are also fully reconstructed and fall along
 413 the main diagonal within the signal region. Approximately 3% of reconstructed events fall
 414 in the signal region. Fortunately, these backgrounds do not peak in the signal region in the
 415 distribution of $M(\pi^+\pi^-(\mu^+\mu^-)_{\text{fit}})$.

416 We simulate $\Upsilon(5S) \rightarrow \Upsilon(1S)\pi^+\pi^-$ with ISR using the models listed in Table 7. To
 417 determine if the choice of decay models affects the distribution shape of our signal variable
 418 $M(\pi^+\pi^-(\mu^+\mu^-)_{\text{fit}})$, we generate additional samples using the VVPIPI decay [18] model for
 419 $\Upsilon(5S) \rightarrow \Upsilon(1S)\pi^+\pi^-$ and the VLL decay model [18] for $\Upsilon(1S) \rightarrow \mu^+\mu^-$. Fig. 15 shows the
 420 distribution of $M(\pi^+\pi^-(\mu^+\mu^-)_{\text{fit}})$ for two different MC samples generated using different
 421 decay models.

422 We find that the choice of decay model has only a small effect on the shape of the
 423 $M(\pi^+\pi^-(\mu^+\mu^-)_{\text{fit}})$ distribution. Furthermore, we plot the $\cos\theta$ of μ^+ in Fig. 16 and find
 424 that the presence of ISR has only a small effect on the the angular distributions of muons. To
 425 determine if ISR affects the width of the $M(\pi^+\pi^-(\mu^+\mu^-)_{\text{fit}})$ distribution for signal processes
 426 $\Upsilon(5S) \rightarrow \gamma W_{bJ}$, we generate additional MC samples for the the signal process $\Upsilon(5S) \rightarrow \gamma W_{bJ}$

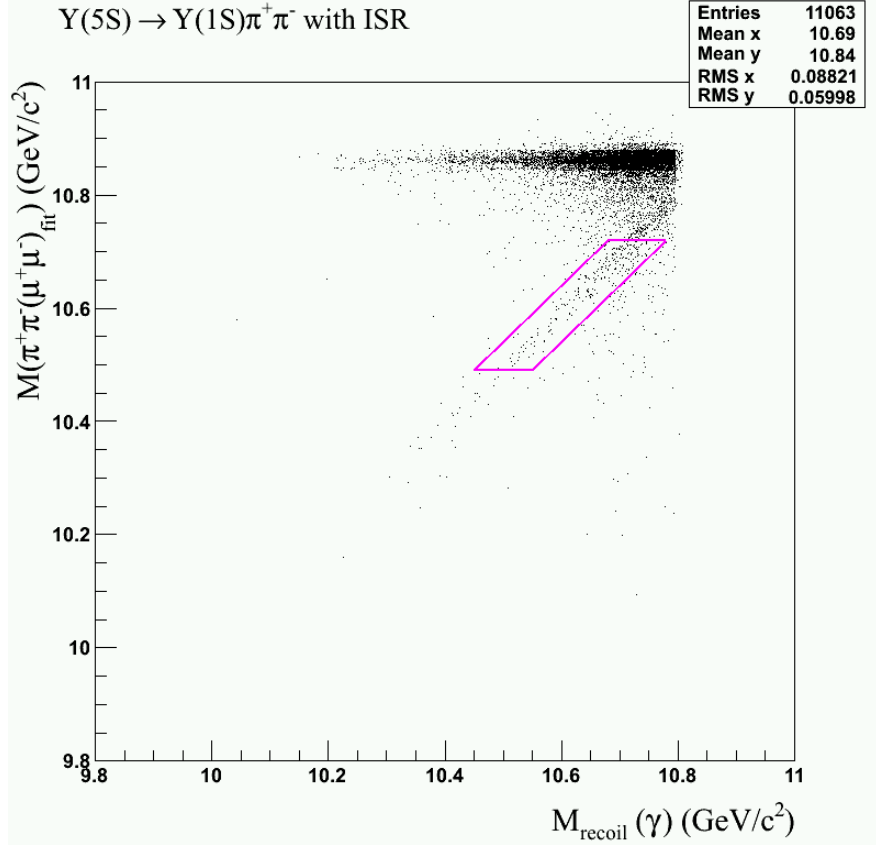


Figure 14: A 2-dimensional $M(\pi^+\pi^-(\mu^+\mu^-)_{\text{fit}})$ vs $M_{\text{rec}}(\gamma)$ distribution for $\Upsilon(5S) \rightarrow \Upsilon(1S)\pi^+\pi^-$ events with ISR (after reweighting). The signal region is outlined in magenta.

Decay Process	Decay Model used in Mote Carlo Simulation
$\Upsilon(5S) \rightarrow \Upsilon(1S)\pi^+\pi^-$	PHSP
$\Upsilon(1S) \rightarrow \mu^+\mu^-$	PHSP
Initial state radiation	VectorISR
Final state radiation	PHOTOS

Table 7: Decay models used in Mote Carlo simulation of $\Upsilon(5S) \rightarrow \Upsilon(1S)\pi^+\pi^-$ with ISR.

427 with ISR. We find that ISR has practically no effect on the width of the distribution of
 428 $M(\pi^+\pi^-(\mu^+\mu^-)_{\text{fit}})$.

429 6.2 Background Shape of $\Upsilon(5S) \rightarrow \Upsilon(1S)\pi^+\pi^-$ with ISR

430 It is likely that events due to $\Upsilon(5S) \rightarrow \Upsilon(1S)\pi^+\pi^-$ with ISR are a dominant source of
 431 backgrounds in the signal region. The rightmost plot in Fig. 17 shows the distribution of
 432 these events within the signal region for our reweighted MC. To see how the selection on
 433 ΔE affects the background shape, we loosen up the selection on ΔE in the left and middle

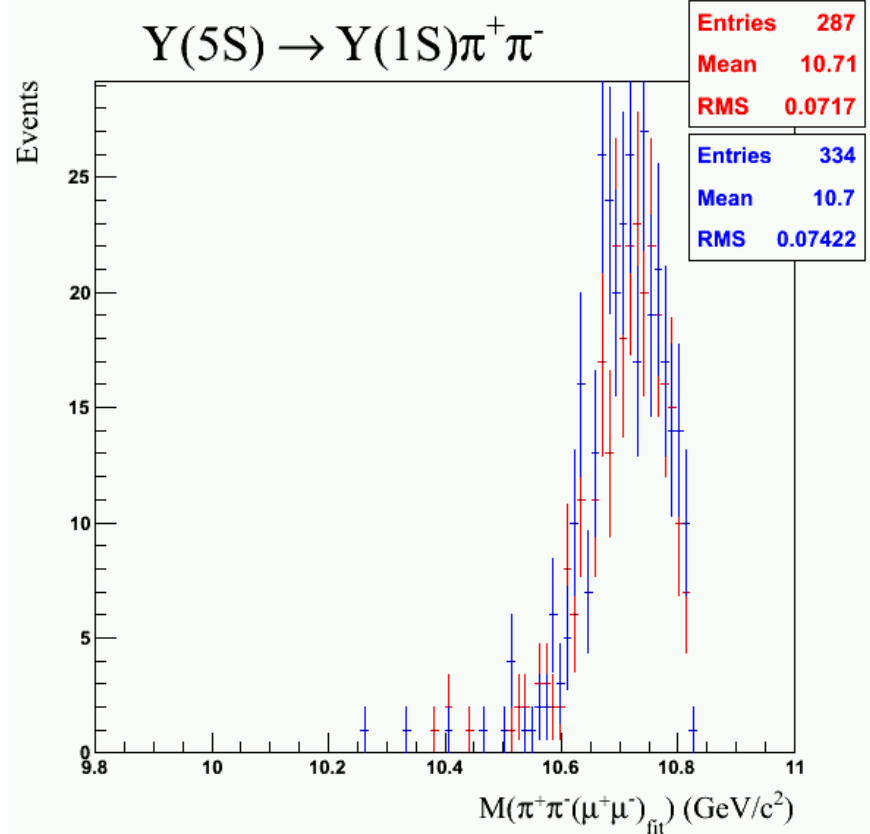


Figure 15: The distribution shown in blue is for events where $\Upsilon(5S) \rightarrow \Upsilon(1S)\pi^+\pi^-$ is generated using VVPIPI model [18] and $\Upsilon(1S) \rightarrow \mu^+\mu^-$ using VLL model [18]. The distribution shown in red is for events generated using PHSP model [18] for both processes. Neither samples contain ISR nor FSR, so they only differ by their decay models. The shapes of their $M(\pi^+\pi^-(\mu^+\mu^-)_{\text{fit}})$ distributions are very similar. Note that although there is a difference in efficiency between the two samples, this is unimportant for our analysis, because we are only interested in possible difference between the shapes of these distributions.

434 plots in Fig. 17. Imposing a selection on ΔE has only a small effect on the shape of these
 435 backgrounds in the signal region.

436 To determine if we can use this MC sample to estimate the number of background events
 437 in the signal region, we divide the grand sideband region shown in Fig. 18 into four smaller
 438 regions as defined in Table 8 and observe if the number of events in MC scales uniformly
 439 to data across all regions. Table 9 shows the number of ISR MC events and data events
 440 within the regions of interest. We see that ISR MC does not scale uniformly across all
 441 regions. While ISR studies improve the quality of our analysis and provide us with useful
 442 information about the shape of this background in the signal region, including ISR into our
 443 analysis does not sufficiently improve the scaling between data and MC in different regions
 444 of grand sideband.

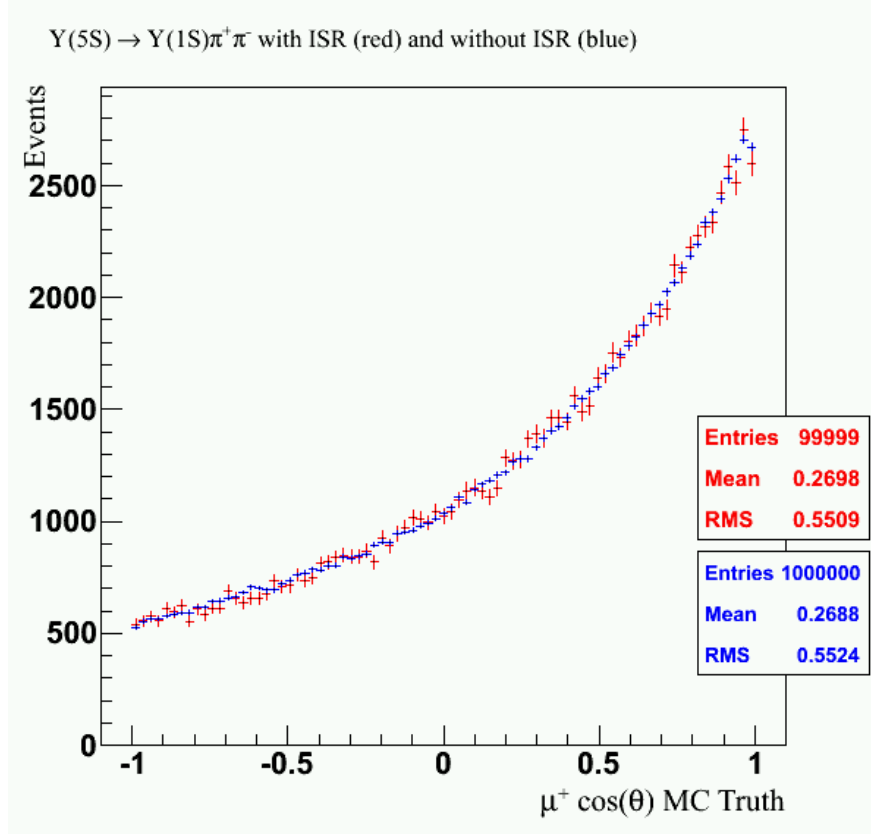


Figure 16: Distributions of $\cos \theta$ for μ^+ for $\Upsilon(5S) \rightarrow \Upsilon(1S)\pi^+\pi^-$ events. The distribution shown in red is for events generated with ISR while the distribution shown in blue is for events generated without ISR. Events in both distributions are generated using PHSP model for both $\Upsilon(5S) \rightarrow \Upsilon(1S)\pi^+\pi^-$ and $\Upsilon(1S) \rightarrow \mu^+\mu^-$. The blue distribution is normalized to the number of events in the red distribution.

Region Name	Boundary Definitions
Region 1	$10.72 \text{ GeV}/c^2 < M(\pi^+\pi^-(\mu^+\mu^-)_{\text{fit}}) < 10.80 \text{ GeV}/c^2$ $-0.2 \text{ GeV} < \Delta E < 0.2 \text{ GeV}$
Region 2	$10.49 \text{ GeV}/c^2 < M(\pi^+\pi^-(\mu^+\mu^-)_{\text{fit}}) < 10.72 \text{ GeV}/c^2$ $0.03 \text{ GeV} < \Delta E < 0.2 \text{ GeV}$
Region 3	$10.38 \text{ GeV}/c^2 < M(\pi^+\pi^-(\mu^+\mu^-)_{\text{fit}}) < 10.49 \text{ GeV}/c^2$ $-0.2 \text{ GeV} < \Delta E < 0.2 \text{ GeV}$
Excluded Region	$10.49 \text{ GeV}/c^2 < M(\pi^+\pi^-(\mu^+\mu^-)_{\text{fit}}) < 10.72 \text{ GeV}/c^2$ $-0.2 \text{ GeV} < \Delta E < 0.03 \text{ GeV}$

Table 8: Definitions of subdivisions of the grand sideband region. The Excluded Region is not considered in this analysis.

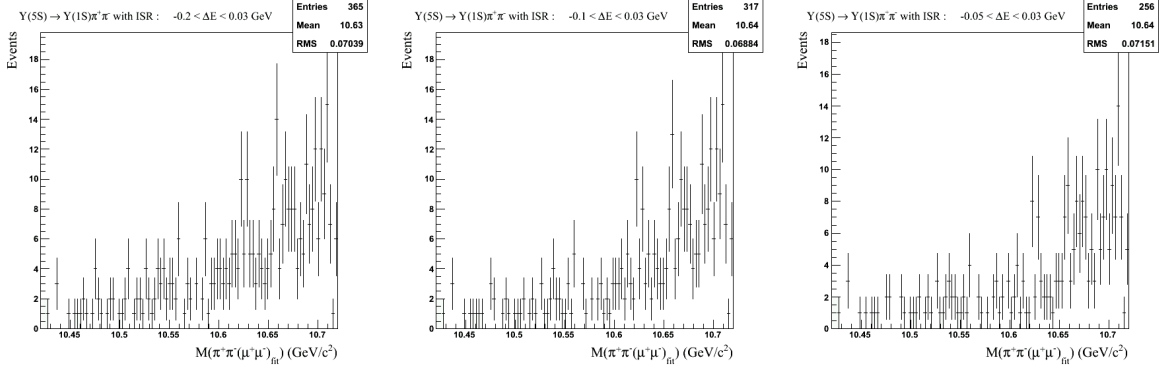


Figure 17: Distributions of $M(\pi^+\pi^-(\mu^+\mu^-)_{\text{fit}})$ for $\Upsilon(5S) \rightarrow \Upsilon(1S)\pi^+\pi^-$ with ISR in the signal region for different ΔE requirements. The leftmost distribution requires $-0.2 \text{ GeV} < \Delta E < 0.03 \text{ GeV}$, the middle distribution requires $-0.1 \text{ GeV} < \Delta E < 0.03 \text{ GeV}$, and the rightmost distribution requires $-0.05 \text{ GeV} < \Delta E < 0.03 \text{ GeV}$. The upper bound of ΔE is kept at 0.03 GeV for all distributions, since very few signal events fall beyond $\Delta E > 0.03 \text{ GeV}$.

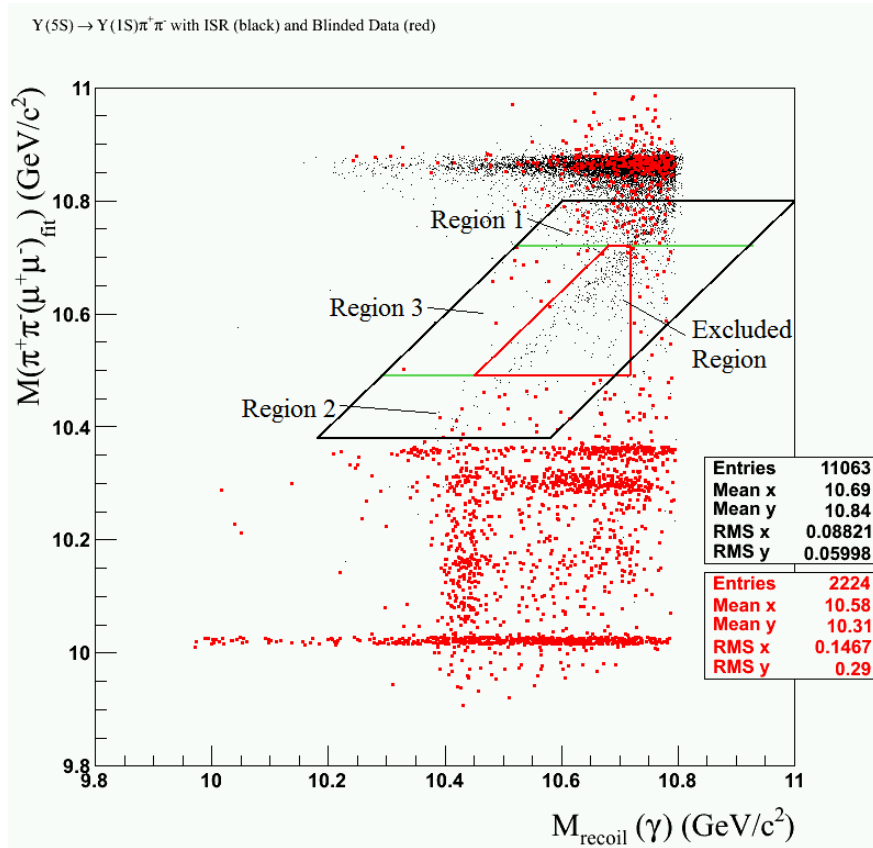


Figure 18: Subdivisions of the grand sideband region. The Excluded Region is not considered in this analysis.

Region	Number of events in ISR MC (N_{mc})	Number of events in blinded data (N_{data})	N_{mc}/N_{data}
Region 1	572	55	10.4
Region 2	28	23	1.2
Region 3	35	14	2.5

Table 9: Comparing the number of events in ISR MC and blinded data in the subdivided grand sideband region

7 Contribution from $\Upsilon(5S) \rightarrow Z_b^{(\prime)\pm} \pi^\mp$

Belle previously reported [15] that charged Z_b and Z_b' states comprise, respectively, approximately 2.54% and 1.04% of the 1819 $\Upsilon(1S)\pi^+\pi^-$ (followed by $\Upsilon(1S) \rightarrow \mu^+\mu^-$) events observed with the full data sample. The overall reconstruction efficiency in Z_b analysis was estimated to be around 46%. This allows us to estimate that, with an ideal, *i.e.* 100% efficient detector, we would expect to detect, approximately, 100 Z_b and 41 Z_b' events.

To estimate cross-feed between Z_b and W_{bj} analyses, we generated approximately 50,000 events for $\Upsilon(5S) \rightarrow Z_b^\pm \pi^\mp$ followed by $Z_b^\pm \rightarrow \Upsilon(1S)\pi^\mp$, $\Upsilon(1S) \rightarrow \mu^+\mu^-$. We also generated an additional 50,000 events for $\Upsilon(5S) \rightarrow Z_b'^\pm \pi^\mp$. These samples are 500 and 1000 larger than the numbers of such events which would be observed in data with an ideal detector.

The distribution of $M(\pi^+\pi^-(\mu^+\mu^-)_{\text{fit}})$ vs $M_{\text{rec}}(\gamma)$ is shown in Fig. 19 for both samples after applying our selection criteria for the W_{bj} analysis. Fig. 20 shows the distribution of $M(\pi^+\pi^-(\mu^+\mu^-)_{\text{fit}})$ for events inside the signal and sideband region. It is important to note that, approximately, only 2% of events fall in the signal region for each of the two samples. Therefore, we expect less than 100 events from each of the two Z_b samples to be found in the signal region for the W_{bj} analysis. As explained earlier in this section, to predict the ‘‘contamination’’ of our signal region by Z_b events, this number has to be scaled down by the factors of 500 and 1000 for contributions from Z_b and Z_b' , respectively. Therefore the process $\Upsilon(5S) \rightarrow Z_b^{(\prime)\pm} \pi^\mp$ in total, has negligible cross-feed contribution in the signal region and can be safely ignored.

8 Fitting

8.1 Signal and Background PDFs

To extract signal yield, we perform a one-dimensional extended unbinned ML fit to the variable $M(\pi^+\pi^-(\mu^+\mu^-)_{\text{fit}})$ using RooFit [22]. We model the signal distribution of $M(\pi^+\pi^-(\mu^+\mu^-)_{\text{fit}})$ as a Breit-Wigner convolved with the sum of two Gaussians (to simulate effects of detector resolution as shown in Fig. 6). The observed width and shape of $M(\pi^+\pi^-(\mu^+\mu^-)_{\text{fit}})$ distribution in signal MC remains practically the same after applying our ΔE requirement and after including ISR. Therefore, we fix the width of our signal PDF. We set the width of the Breit-Wigner to be $\sigma_{BW} = 15 \text{ MeV}/c^2$ to match the intrinsic width of Z_b and Z_b' . The

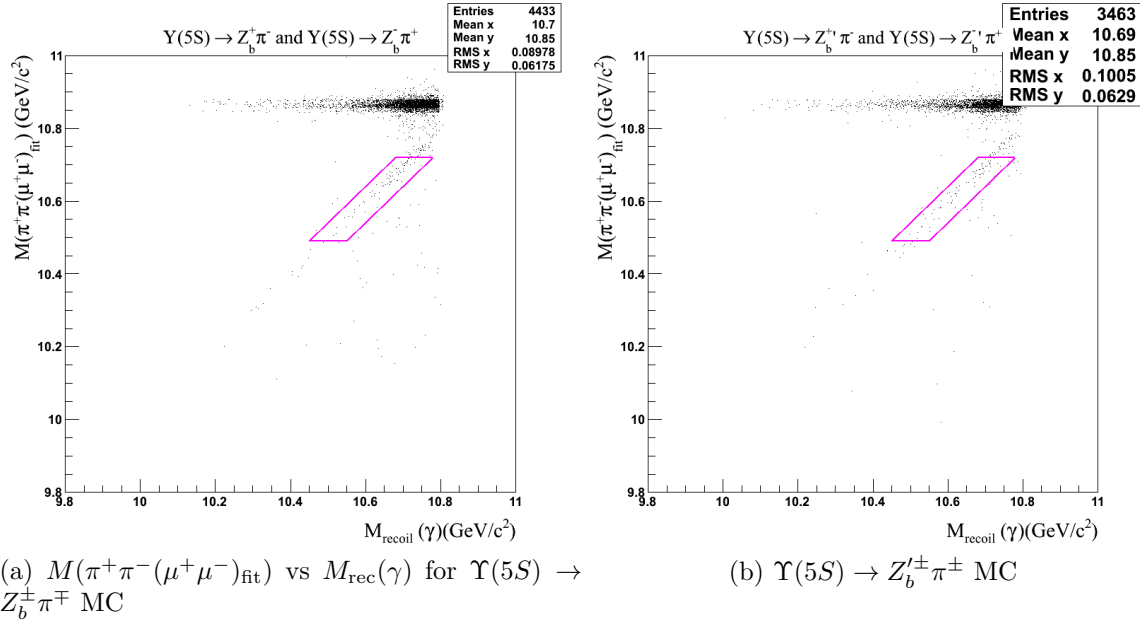
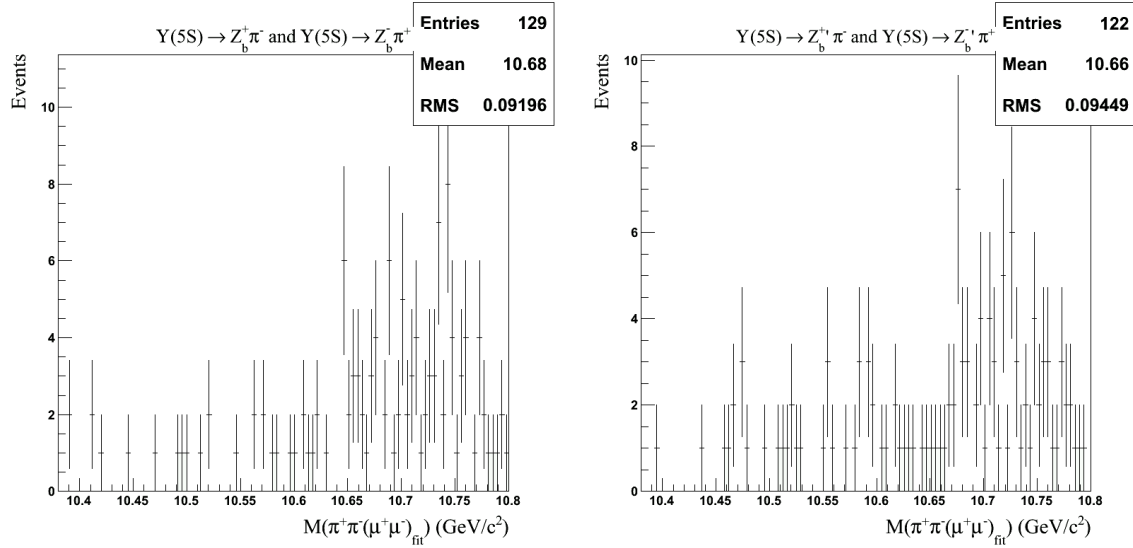


Figure 19: The distribution of $M(\pi^+\pi^-(\mu^+\mu^-)_{\text{fit}})$ vs $M_{\text{recoil}}(\gamma)$ for $\Upsilon(5S) \rightarrow Z_b^{(\prime)\pm}\pi^\mp$ MC.



(a) $M(\pi^+\pi^-(\mu^+\mu^-)_{\text{fit}})$ for $\Upsilon(5S) \rightarrow Z_b^\pm\pi^\mp$ MC. (b) $M(\pi^+\pi^-(\mu^+\mu^-)_{\text{fit}})$ for $\Upsilon(5S) \rightarrow Z_b^{\prime\pm}\pi^\mp$ MC.

Figure 20: The distribution of $M(\pi^+\pi^-(\mu^+\mu^-)_{\text{fit}})$ for $\Upsilon(5S) \rightarrow Z_b^{(\prime)\pm}\pi^\mp$ MC for events inside the signal and sideband region.

474 widths of the Gaussians used in convolution are $\sigma_{G_1} \approx 3 \text{ MeV}/c^2$ and $\sigma_{G_2} \approx 7.7 \text{ MeV}/c^2$ to
 475 match the widths obtained from the fit to $M(\pi^+\pi^-(\mu^+\mu^-)_{\text{fit}})$ resolution. We let the mean
 476 of Breit-Wigner float within the fit, as W_{bJ} could be observed at different invariant masses
 477 for different spins J . Table 10 lists the values of parameters used in our signal PDF model.
 478 We use an exponential $e^{\lambda x}$ to model background contributions due to ISR as well as

Quantity	Value Used in Signal PDF (MeV/c ²)
σ_{BW}	15
Mean of BW	floats between 10.38 and 10.80 GeV/c ²
σ_{G_1}	3.0 ± 0.1
σ_{G_2}	7.7 ± 0.2
Fraction of Gaussian 1	0.73 ± 0.01
Fraction of Gaussian 2	0.27 ± 0.01
Mean of both Gaussians	$(-3.8 \pm 0.2) \cdot 10^{-4}$

Table 10: Values of fixed quantities in the signal PDF model.

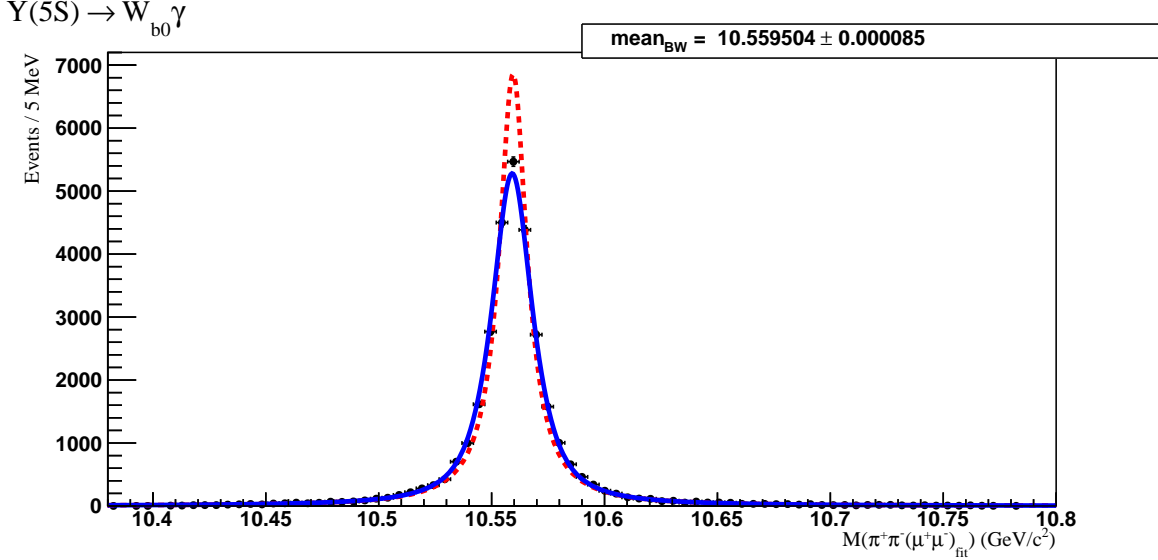
479 possible non-resonant contribution from dimuon continuum events. Strictly speaking, the
480 background distribution deviates from an exponential at $M(\pi^+\pi^-(\mu^+\mu^-)_{\text{fit}}) \approx 10.75$ GeV/c².
481 because of the phase space boundary at $M_{\text{rec}}(\gamma) \approx 10.75$ GeV/c² seen in Fig. 5. This
482 ever-present effect can be seen in figures showing the distribution of $M(\pi^+\pi^-(\mu^+\mu^-)_{\text{fit}})$ for
483 background events with our ΔE requirement (*e.g.* see Fig. 15, Fig. 21b, Fig. 21c). This
484 shortcoming of our analysis will be taken care of in the next version of this Note. We would
485 like to remark that the observed fall-off effect is easy to understand and describe in the
486 model used for fitting, as it is exclusively due to the boundary of phase space.

487 To estimate the number of background events we expect in the signal region, we per-
488 form an extended unbinned maximum likelihood fit to data only in the sideband regions.
489 To account for uncertainty in the number of data events in the sideband region, we fit
490 $M(\pi^+\pi^-(\mu^+\mu^-)_{\text{fit}})$ within the range of 10.38 GeV/c² and 10.80 GeV/c² when extracting
491 signal yield. This range corresponds to the signal region and sideband regions combined.
492 From the fit, we obtain $\lambda = 3.7951$. We extract 59 ± 11 background events in the signal
493 region and sideband regions combined. We expect 27 ± 5 of these background events to be
494 in the signal region alone. Fits to W_{b0} signal MC, $\Upsilon(5S) \rightarrow \Upsilon(1S)\pi^+\pi^-$ MC with ISR MC,
495 and data in the sidebands are shown in Fig. 21.

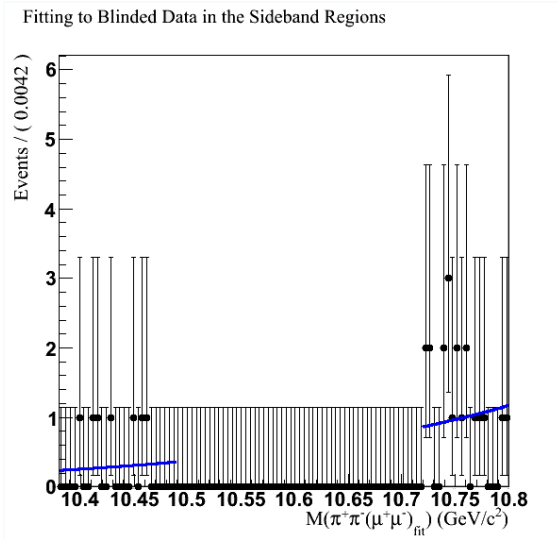
496 8.2 Confidence Belts

497 To construct a 90% confidence belt (with 5% on each side of the belt), we perform ensemble
498 tests. Each ensemble test consists of 1000 toy MC experiments. In each toy MC experiment,
499 we generate N_{sig} signal events and N_{bkg} background events according to their respective
500 PDF lineshapes used for fitting signal and background. We then fit the generated events in
501 the range $10.38 \text{ GeV}/c^2 < M(\pi^+\pi^-(\mu^+\mu^-)_{\text{fit}}) < 10.80 \text{ GeV}/c^2$ to our combined signal and
502 background PDF to extract the fitted number of signal events $N_{\text{sig}}^{\text{fit}}$.

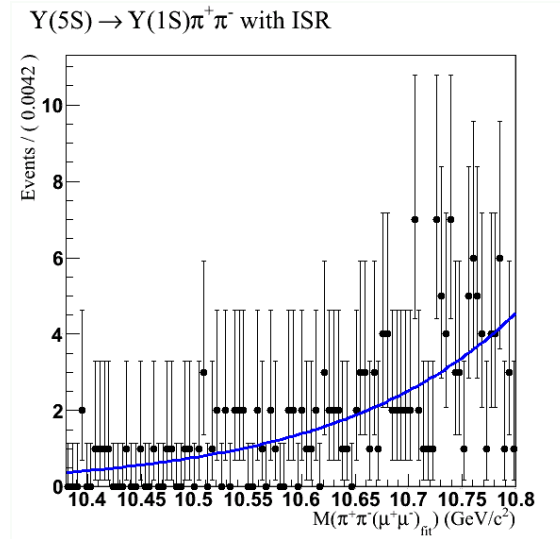
503 We construct our 90% confidence belt by performing ensemble tests with $N_{\text{bkg}}^{\text{gen}} = 59$ for
504 values of $N_{\text{sig}}^{\text{gen}}$ from 0 to 70. We additionally construct a 90% confidence belt where we allow
505 Poisson fluctuation in $N_{\text{bkg}}^{\text{gen}}$. These confidence belts are shown in Fig. 22.



(a) Fit result for the distribution of $M(\pi^+\pi^-(\mu^+\mu^-)_{\text{fit}})$ for signal MC in the signal and sideband region. The Breit-Wigner shape is shown in red. The blue distribution is the Breit-Wigner convolved with the sum of two Gaussians.



(b) Fit result for the distribution of $M(\pi^+\pi^-(\mu^+\mu^-)_{\text{fit}})$ for data in the sideband region.

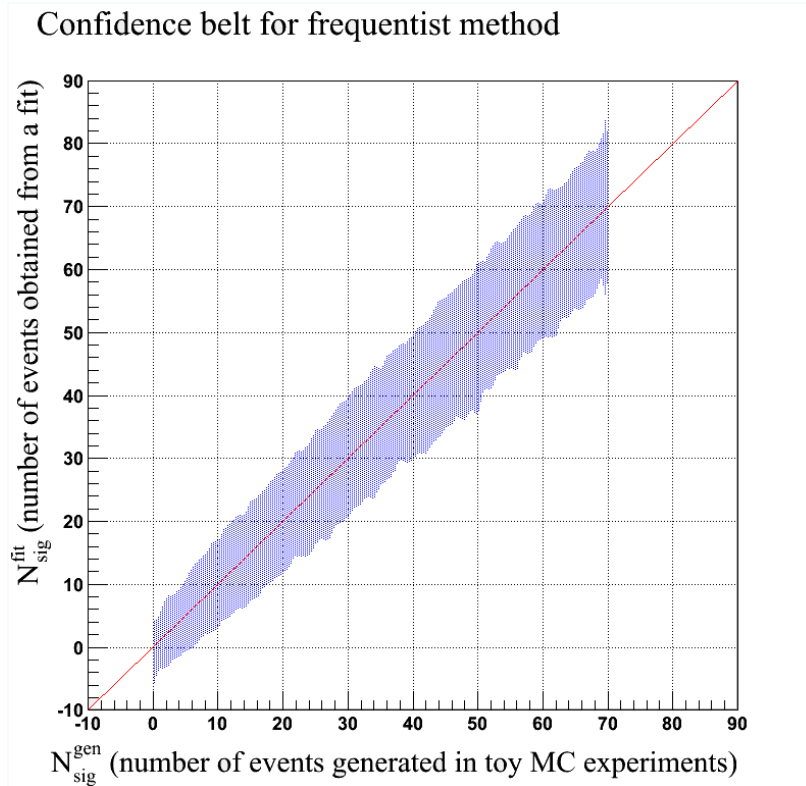


(c) Fit result for the distribution of $M(\pi^+\pi^-(\mu^+\mu^-)_{\text{fit}})$ for $\Upsilon(5S) \rightarrow \Upsilon(1S)\pi^+\pi^-$ with ISR for events in the signal region.

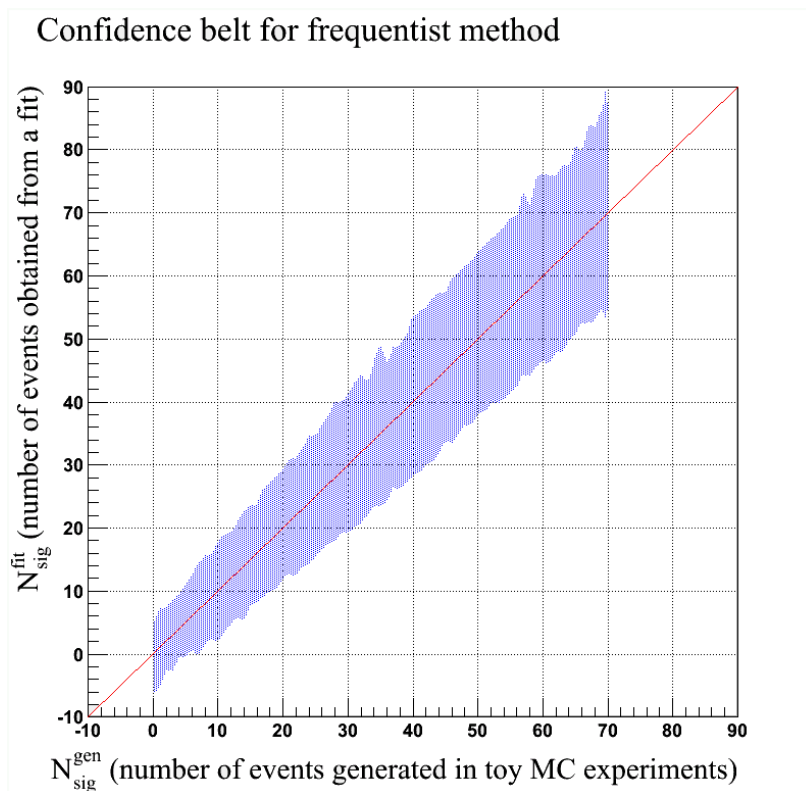
Figure 21: Fitting background MC and data

506 8.3 Linearity Study

507 To validate our fitting procedures, we perform a linearity study using ensemble tests. En-
 508 semble tests are generated as described in Section 8.2. For each ensemble test of 1000 toy
 509 MC experiments, we calculate the average number of signal events from the fit and the error
 510 associated with the average. We vary $N_{\text{sig}}^{\text{gen}}$ from 0 to 10 in steps of 1 and from 10 to 50 in
 511 steps of 5 while fixing $N_{\text{bkg}} = 59$.



(a) Does not include Poisson fluctuations in $N_{\text{bkg}}^{\text{gen}}$



(b) Includes Poisson fluctuations in $N_{\text{bkg}}^{\text{gen}}$.

Figure 22: 90% confidence belts for frequentist method.

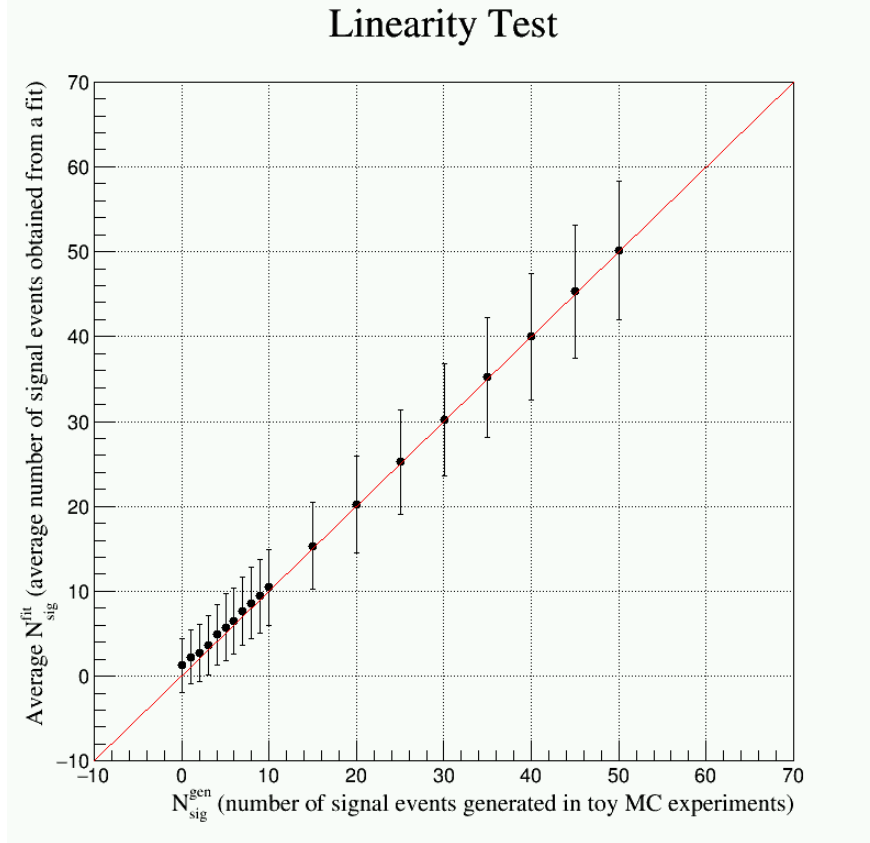
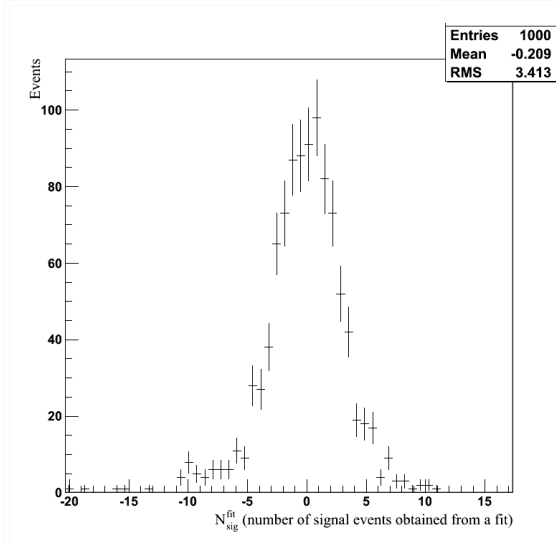


Figure 23: Average $N_{\text{sig}}^{\text{fit}}$ for varying values of $N_{\text{sig}}^{\text{gen}}$. The solid black line is the result of fitting these points to the linear function $f(x) = p_0 + p_1x$. The resulting fit parameters are shown in the box on the top right.

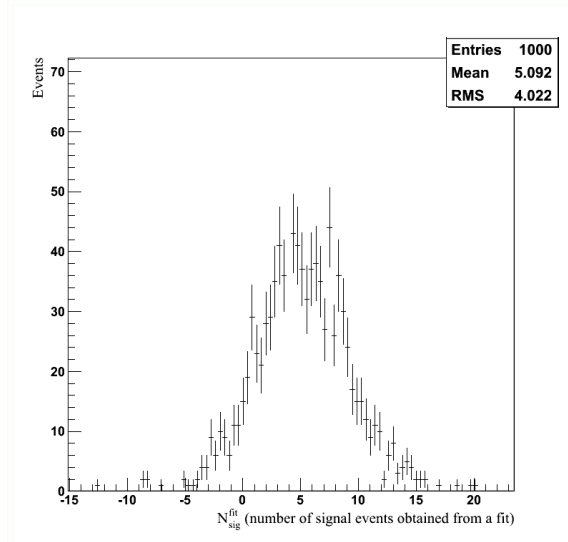
512 We plot the average number of signal events from the fit against $N_{\text{sig}}^{\text{gen}}$ and perform a fit
513 to a linear function $f(x) = p_0 + p_1x$. This plot and the results of the linear fit are shown
514 in Fig. 23. Fig. 24 displays distributions of $N_{\text{sig}}^{\text{fit}}$ for certain values of $N_{\text{sig}}^{\text{gen}}$. When $N_{\text{sig}}^{\text{gen}}$ is
515 large, the distribution of $N_{\text{sig}}^{\text{fit}}$ is unbiased. However, for small $N_{\text{sig}}^{\text{gen}}$, we see an asymmetry
516 in the distribution of $N_{\text{sig}}^{\text{fit}}$, indicating some bias. This effect is often observed for small
517 statistics and is not unexpected.

518 8.4 Sensitivity Estimation

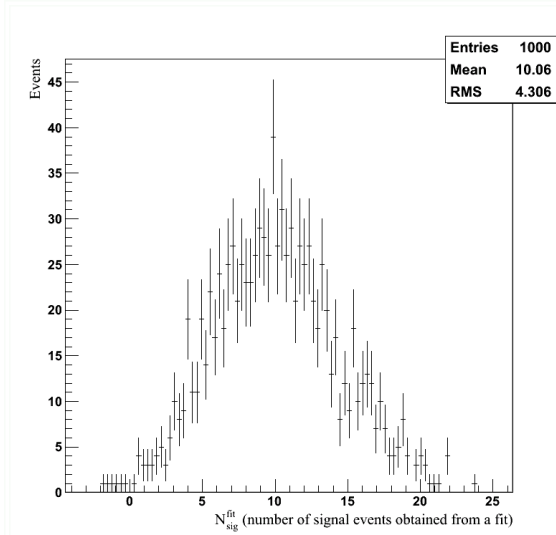
519 We estimate the upper limit on the branching fraction and visible cross section of $\Upsilon(5S) \rightarrow$
520 $\gamma W_{b,J}$ in the absence of signal by performing an extended unbinned maximum likelihood fit
521 on toy MC generated according to the fit to the data sidebands. We generate 1000 toy MC
522 samples with 59 background events, fit our combined signal and background shape to each
523 sample, and then average the resulting signal yields. There is an average signal yield of
524 -0.2 ± 3.2 events. Note that in Fig. 23, this average signal yield corresponds to the value
525 plotted at $N_{\text{sig}}^{\text{gen}} = 0$. Using the confidence belt in Fig. 22, we determine the 95% confidence
526 level upper limit on the number of signal events to be 10 events. We calculate the upper



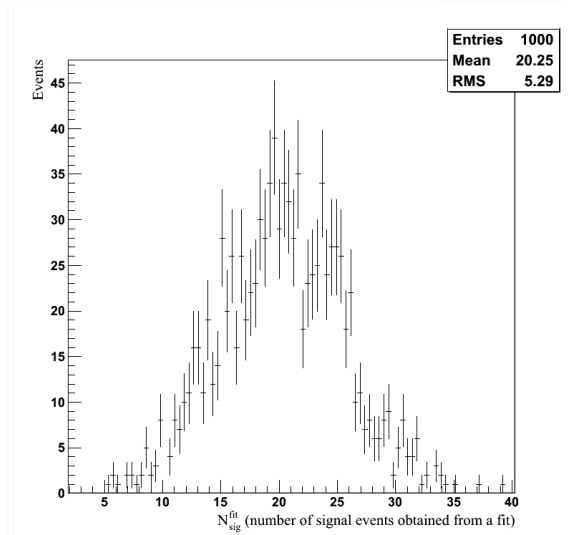
(a) Distribution of $N_{\text{sig}}^{\text{fit}}$ for an ensemble test with $N_{\text{sig}}^{\text{gen}} = 0$ and $N_{\text{bkg}}^{\text{gen}} = 59$.



(b) Distribution of $N_{\text{sig}}^{\text{fit}}$ for an ensemble test with $N_{\text{sig}}^{\text{gen}} = 5$ and $N_{\text{bkg}}^{\text{gen}} = 59$.



(c) Distribution of $N_{\text{sig}}^{\text{fit}}$ for an ensemble test with $N_{\text{sig}}^{\text{gen}} = 10$ and $N_{\text{bkg}}^{\text{gen}} = 59$.



(d) Distribution of $N_{\text{sig}}^{\text{fit}}$ for an ensemble test with $N_{\text{sig}}^{\text{gen}} = 20$ and $N_{\text{bkg}}^{\text{gen}} = 59$.

Figure 24: $N_{\text{sig}}^{\text{fit}}$ Distributions for ensemble tests with different $N_{\text{sig}}^{\text{gen}}$.

527 limit on the branching fraction in the absence of signal as follows:

$$\mathcal{B}(\Upsilon(5S) \rightarrow \gamma W_{bJ}) \cdot \mathcal{B}(W_{bJ} \rightarrow \Upsilon(1S)\rho^0) = \frac{N_{\text{sig}}}{\epsilon \cdot N_{\Upsilon(5S)} \cdot \mathcal{B}(\Upsilon(1S) \rightarrow \mu^+\mu^-) \cdot \mathcal{B}(\rho^0 \rightarrow \pi^+\pi^-)} \quad (4)$$

528 where $N_{\Upsilon(5S)}$ is the number of $\Upsilon(5S)$ and ϵ is our reconstruction efficiency. Using Eq. 4, we
 529 determine the upper limit on the branching fraction in the absence of signal to be 2.4×10^{-5} .

530 We calculate the visible cross section using

Quantity	Value
N_{sig}	10
ϵ	$(29 \pm 0.17)\%$
$N_{\Upsilon(5S)}$	$(6.53 \pm 0.66) \cdot 10^6$
$\mathcal{B}(\Upsilon(1S) \rightarrow \mu^+\mu^-)$	$(2.48 \pm 0.05)\%$
$\mathcal{B}(\rho^0 \rightarrow \pi^+\pi^-)$	99.8%
\mathcal{L}	121.4 fb^{-1}

Table 11: Values of quantities used to calculate upper limits on visible cross section and the branching fraction. Uncertainty in $\mathcal{B}(\rho^0 \rightarrow \pi^+\pi^-)$ is negligible. Note that, for purposes of estimating upper limits, we use $N_{\text{sig}} = 10$, which is the 95% CL boundary of the 90% CL frequentist belt shown in Fig. 22 for $N_{\text{sig}}^{\text{fit}} = 3$, according to the result of the fit $N_{\text{sig}}^{\text{fit}} = -0.2 \pm 3.2$.

$$\sigma_{\text{vis}} = \frac{N_{\text{sig}}}{\epsilon \mathcal{B}(\Upsilon(1S) \rightarrow \mu^+\mu^-) \mathcal{B}(\rho^0 \rightarrow \pi^+\pi^-) \mathcal{L}} \quad (5)$$

531 where \mathcal{L} is the integrated luminosity. We find $\sigma_{\text{vis}} = (0.115 \pm 0.006) \text{ fb}$. All values used to
532 calculate the branching fraction and visible cross section are shown in Table 11.

533 9 Search Strategy Summary

534 In this analysis, we describe a search for a new molecular state W_{bJ} which could be produced
535 in the radiative transition $\Upsilon(5S) \rightarrow \gamma W_{bJ}$ followed by the decays $W_{bJ} \rightarrow \Upsilon(1S)\rho^0$, $\Upsilon(1S) \rightarrow$
536 $\mu^+\mu^-$, $\rho^0 \rightarrow \pi^+\pi^-$. We fully reconstruct the signal final state consisting of two muons, two
537 pions, and a photon. We perform a blind analysis by optimizing our selection criteria and
538 analysis techniques using only MC samples before applying them to data.

539 To search for the presence of W_{bJ} in Belle data, we propose to "unblind" the data in
540 the signal region and then fit a one-dimensional distribution of $M(\pi^+\pi^-(\mu^+\mu^-)_{\text{fit}})$ using
541 the aforementioned models for signal and background shapes. In the fit, we fix the width
542 of W_{bJ} to that of Z_b . Because we expect only one signal in our signal region, we plan to
543 scan the range of invariant masses of $M(\pi^+\pi^-(\mu^+\mu^-)_{\text{fit}})$ and, for each assumed value of the
544 invariant mass, we perform a fit to data, where the background parameter λ is allowed to
545 float. If the fit returns a statistically significant result, we claim a discovery. We will then
546 produce a plot of the upper limit versus mass of W_{bJ} . This plot will be produced regardless
547 of whether or not the fit yields a significant result. Our confidence belt (Fig. 22) will be
548 used to either claim a discovery of W_{bJ} or establish an upper limit on the signal production
549 rate (branching fraction) for the radiative decay $\Upsilon(5S) \rightarrow \gamma W_{bJ}$. The following sources of
550 systematic uncertainties will be considered in our final estimate of the upper limit of the
551 branching fraction of $\Upsilon(5S) \rightarrow \gamma W_{bJ}$:

- 552 • Number of $\Upsilon(5S)$

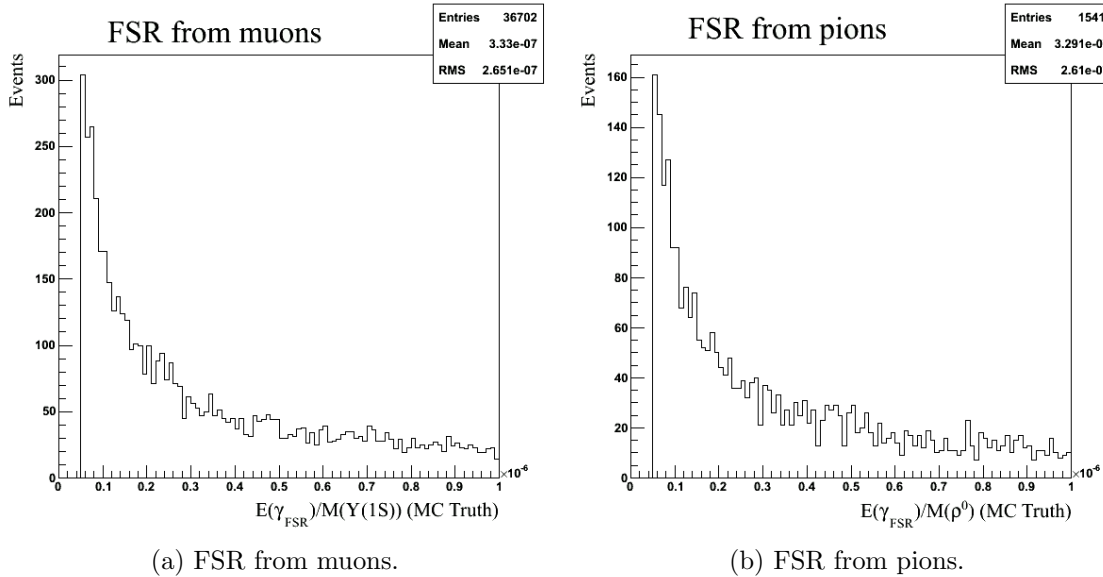


Figure 25: Final state radiation from charged tracks

- 553 • Signal Reconstruction Efficiency
- 554 • Daughter Branching Fractions
- 555 • MC statistics
- 556 • PDF parameterization
- 557 • Fit bias
- 558 • Trigger efficiency

559 10 Appendix

560 10.1 Final State Radiation

561 In the version of package PHOTOS used by Belle, the minimum FSR photon energy (eval-
562 uated in the center of mass frame of charged particle's parent) is calculated as follows:

$$E(\gamma_{FSR}) = (\text{XPHCUT}) \cdot 0.5 \cdot M(\text{parent}) \tag{6}$$

563 where XPHCUT is a hardcoded constant set to 0.01. Hence, the minimum FSR energy is
564 approximately 4 MeV for pions ($M(\rho^0) = 770$ MeV) and 50 MeV for muons ($M(\Upsilon(1S)) =$
565 9.46 GeV). The lower limit on FSR energy for muons is too high, so we lowered the
566 value of XPHCUT to 10^{-7} . To accomplish this, we changed XPHCUT=0.01D0 to XPH-
567 CUT=0.0000001D0, recompiled the phocin.F source code and then rebuilt EvtGen with an
568 updated PHOTOS library.

569 To verify that XPHCUT was successfully lowered to 10^{-7} , we plot the ratios $\frac{E(\gamma_{FSR})}{M(\Upsilon(1S))}$
 570 and $\frac{E(\gamma_{FSR}^p)}{M(\rho)}$ as generated in Fig. 25. Because these quantities are bounded from below by
 571 $XPHCUT \cdot 0.5$, we prove that XPHCUT was successfully lowered.

572 10.2 Changes in the Analysis between Note v1.5 and v2.0

573 In this section we describe and explain the reasons for important changes we made in the
 574 analysis after Note v1.0 was released. These changes have not yet been applied to the main
 575 body of the text. All plots – except those in this and the next sections of this Note (v1.5)
 576 – have been made using the selection developed in the original analysis. The next version
 577 of this Note (v2.0) will have some of the critical plots and tables in the main section of the
 578 note updated to reflect for the changes described below.

579 Overall, there are four changes in the analysis related to (1) photon energy selection
 580 (extended), (2) the region blinded in data (increased), (3) selection criteria on dr and dz
 581 (relaxed) and (4) PID requirements for charged pions (removed).

582 The main improvement (extending signal photon energy spectrum) helps us to develop
 583 a robust and reliable approach to fitting the signal invariant mass spectrum (to be applied
 584 to data when the permission to open the signal region is secured). Extending the blinded
 585 region in data was done to avoid an annoying “undercoverage” demonstrated in Fig. 7 of
 586 Note v1.1, *i.e.* our decision to impose a requirement on ΔE was made after we had defined
 587 the blinded region, and hence, the top right corner of the signal region was not blinded
 588 originally. While no signal is expected in that corner, we would prefer to blind the entire
 589 signal region to simplify fitting. We deemed the changes in the selection applied to track
 590 impact parameters to be “right”, so no additional systematics needs to be included in the
 591 result of the analysis. For the same reason we decided to remove PID cuts for charged pion
 592 candidates: any such selection criterion costs us some (even if very small) efficiency loss,
 593 and, more importantly, has some systematic uncertainty associated with it. We made the
 594 changes in PID and impact parameters selection just because we had to reskim the data and
 595 generic MC anyway.

596 The four changes are itemized (and elaborated more on) below, starting with the most
 597 important improvement in the analysis:

598 • Signal Photon Energy

599 In the first version of this Note, as shown in Table 3, signal photon candidates were
 600 selected in the range between 100 and 600 MeV. As you can see in Fig. 4a of this
 601 version of the Note, this energy range is sufficient for signal photon selection, how-
 602 ever, we found it to be very restrictive for purposes of fitting the signal invariant
 603 mass $M(\pi^+\pi^-(\mu^+\mu^-)_{\text{fit}})$ including the sidebands. This effect is explained better in a
 604 dedicated subsection below.

605 • Blinded Region in Data

606 As we already explained, our original blinding (which we decided about before we
 607 developed the fitting procedure) inadvertently exposed one corner of the signal region in
 608 data to possible inspection. This possibly introduces some bias, but more importantly

Region Name	Boundary Definitions
The New Blinded Region	$10.49 \text{ GeV}/c^2 \leq M(\pi^+\pi^-(\mu^+\mu^-)_{\text{fit}}) \leq 10.72 \text{ GeV}/c^2$ $M_{\text{rec}}(\gamma) \geq M(\pi^+\pi^-(\mu^+\mu^-)_{\text{fit}}) - 0.04 \text{ GeV}/c^2$ $M_{\text{rec}}(\gamma) \leq 11.0 \text{ GeV}/c^2$

Table 12: The new (wider) blinded region in data. The important change is shown in red color. However, it is redundant and adds nothing new as compared to the second line in this table.

609 makes the fitting of the $M(\pi^+\pi^-(\mu^+\mu^-)_{\text{fit}})$ distribution slightly more difficult. As
610 we had to reskim the data and repeat all analysis steps, we decided to extend the
611 blinded region as shown in Table 12. Please compare this with Table 5 in the original
612 version of the note. In one sentence, we blinded the entire right-side tail of the $M_{\text{rec}}(\gamma)$
613 distribution. Note that the change shown in red color in this table is not even necessary:
614 the second line of the boundary described in the table is sufficient to achieve our goal.
615 We show the third line in the table only so the comparison with the previous version
616 of this Note is easier to make.

617 • **Impact Parameters for Charged Tracks**

618 The dz and dr selection criteria have been loosened to ≤ 4 cm and ≤ 0.5 cm, respec-
619 tively.

620 • **PID Requirements for Charged Pion Candidates**

621 These requirements have been eliminated.

622 As we already mentioned, these four changes in the selection criteria required us to reskim
623 generic MC and data. That was easy.

624 **10.2.1 Signal Photon Energy Conundrum**

625 Well, retrospectively, extending signal photon energy selection was not really a very difficult
626 decision, but it requires a thorough explanation. Below we try our best to walk the reader
627 through the logic of our decision.

628 In our analysis we extract the signal yield by fitting the distribution of the signal invariant
629 mass $M(\pi^+\pi^-(\mu^+\mu^-)_{\text{fit}})$. We are confident (because we proved this) that we observe the ISR
630 background (*i.e.* events where the production of $\Upsilon(5S)$ is accompanied by some initial state
631 radiation). However, we suspect that there are other sources of non-peaking background,
632 such as, *e.g.* poorly reconstructed events of all possible types, cosmic events overlapping
633 with incompletely reconstructed collision events – you name it – present in data. The key
634 part of our approach to fitting is that, on basis of our extensive and thorough studies of
635 non-signal data and generic MC, we expect no peaking backgrounds to be present in the
636 signal region.

637 For as long as no bias is present in selecting signal event candidates, background events
638 of ISR origin are relatively well described (as you will see for yourself very soon) by the sum

639 of an exponential and a straight line of non-negative slope. Small non-peaking background is
 640 likely to be sufficiently-well approximated also by the same straight line (of zero or positive
 641 slope). However, our original selection criteria strongly suppressed ISR background at large
 642 values of the signal invariant mass $M(\pi^+\pi^-(\mu^+\mu^-)_{\text{fit}})$, making it very difficult to reliably
 643 obtain the shape of such biased background distribution using sidebands in data. We realized
 644 that, in order to significantly reduce such possible bias, we have to avoid suppressing ISR
 645 background in the sideband region.

646 To demonstrate the effect we are trying to explain in this section, we generated a some-
 647 what ridiculous MC sample, where an incredibly broad “structure” (an almost flat distribu-
 648 tion of the invariant mass called, for purposes of MC production, “ $\Upsilon(5S)$ ” (which it is most
 649 definitely not!)) was generated along with ISR in the e^+e^- annihilation followed by this
 650 structure’s “decay” to $\Upsilon(1S)\pi^+\pi^-$. Applying our selection criteria to such MC sample after
 651 detector simulation and reconstruction allows us to investigate the phase space of relevant
 652 kinematic parameters at sufficient level of precision to make meaningful conclusions. Note
 653 that we do not even try to reweight the ISR energy spectrum in this exercise, because all we
 654 need for our studies is a good coverage of phase space (which is already a good enough of a
 655 reason NOT to reweight such MC!).

656 We start by demonstrating, in Fig. 26, that, with the original signal photon energy
 657 selection, the reconstructed ISR background does not resemble an exponent in the signal
 658 plus sideband region of the invariant mass $M(\pi^+\pi^-(\mu^+\mu^-)_{\text{fit}})$ (indicated by vertical lines
 659 in this figure). The explanation for the observed shape lies in the cut on signal photon
 660 energy requiring at least 100 MeV. Further, Fig. 27, where we show the 2D distribution
 661 of the reconstructed signal photon energy (in the lab) vs $M(\pi^+\pi^-(\mu^+\mu^-)_{\text{fit}})$, demonstrates
 662 that the range of the invariant mass $M(\pi^+\pi^-(\mu^+\mu^-)_{\text{fit}})$ is actually biased on both ends of
 663 the spectrum – at higher masses because of the 100 MeV cut, at smaller masses because
 664 of the 600 MeV cut. Note that the relevant value of the invariant mass, where the ISR
 665 background is suppressed by the 100 MeV cut, is located at the intersection of the left-side
 666 of the “opening cone” of phase space with the horizontal line of the 100 MeV cut on the
 667 photon energy. Note that the opening angle of the cone describing the phase space is due to
 668 the ΔE selection, which we keep to be $-0.05 \text{ GeV} \leq \Delta E \leq 0.03 \text{ GeV}$.

669 In order to avoid the described bias in background photon energy spectrum and to be
 670 able to use the higher-mass sideband to perform a robust fit to such background, we release
 671 the cut on signal photon energy to the lowest possible value of 20 MeV (standard Belle
 672 reconstruction and MDST production do not go lower than that). Note that in our analysis
 673 we do not really care about possible energy dependence of photon reconstruction efficiency
 674 systematic uncertainty, because our signal is associated with photons of higher energy, but
 675 we need (even if smoothly suppressed) an exponential-like energy distribution of background
 676 photons to make extracting the signal from data reliable. In our approach we obtain the
 677 shape of background distribution from data also.

678 Interestingly, to improve our understanding of backgrounds, we also have to raise the
 679 cut on the other end of the photon energy region, though, in this case, for a different
 680 reason. As is explained in Table 6 and Fig. 10 of the original version of the note, there is
 681 a particular peaking background, namely, radiative (*i.e.* ISR) production of $\Upsilon(3S)$ followed
 682 by its dipion transition to $\Upsilon(1S)$, which is uncomfortably too close to the left side of our
 683 signal plus sideband region of $M(\pi^+\pi^-(\mu^+\mu^-)_{\text{fit}})$. When both charged pions and the photon

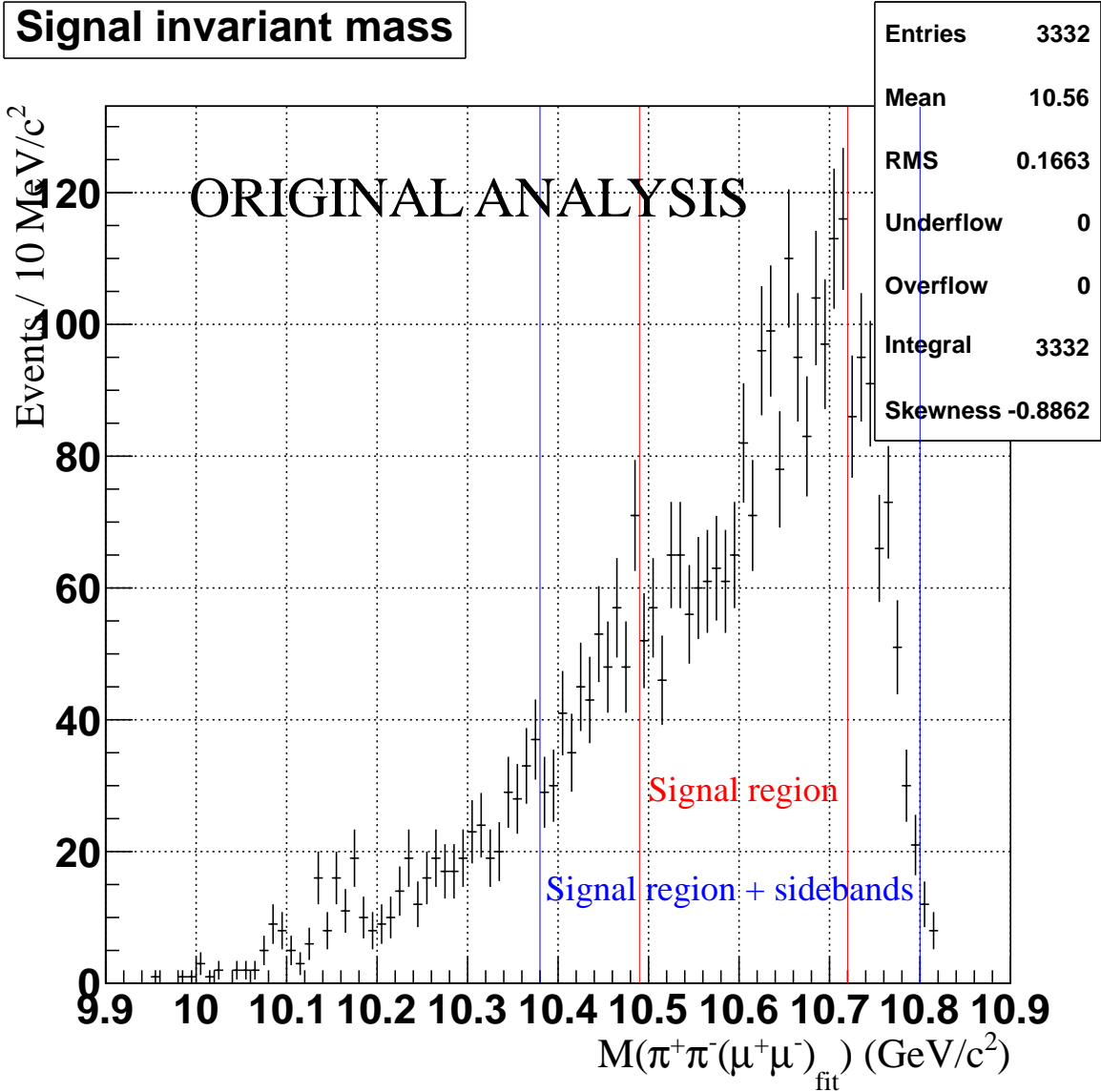


Figure 26: The reconstructed invariant mass $M(\pi^+\pi^-(\mu^+\mu^-)_{\text{fit}})$ for a special ISR MC sample with the original selection criteria. Only best candidates are shown.

684 are misreconstructed, sometimes this unfortunate happenstance might shift some of such
 685 these events into the signal region. Therefore, it would be best to investigate this possible
 686 background using the data. This goal requires us to release the signal photon energy cut.
 687 For practical purposes, in the improved version of the analysis, we limit signal photon energy
 688 to 5 GeV. Note that our approach also facilitates possible measurement of ISR production
 689 of $\Upsilon(3S)$ and $\Upsilon(2S)$, which could be used to calibrate ISR MC.

690 After widening the signal photon candidate energy selection as described and explained,
 691 we plot the distributions of photon energy spectrum vs $M(\pi^+\pi^-(\mu^+\mu^-)_{\text{fit}})$ in Fig. 28 and
 692 $M(\pi^+\pi^-(\mu^+\mu^-)_{\text{fit}})$ in Fig. 29 (as always, for best candidates only) for MC events from our
 693 “ridiculous” background MC sample. We conclude that the current (*i.e.* new, relaxed) se-
 694 lection criteria allow us to perform a robust fit to the background using the sidebands of

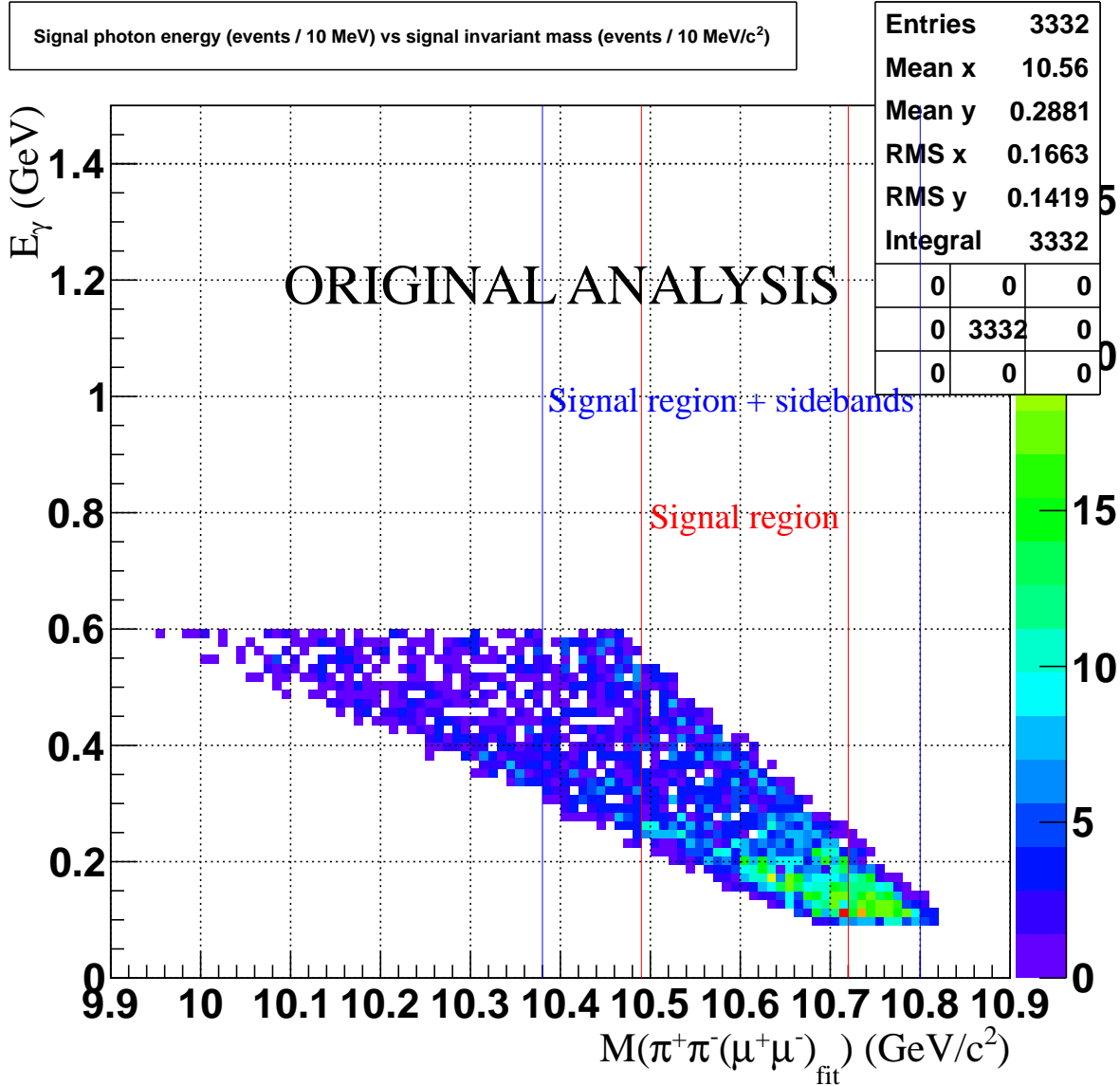


Figure 27: The reconstructed signal photon energy versus the invariant mass $wbjm$ for a special ISR MC sample with the original selection criteria. Only best candidates are shown.

695 $M(\pi^+\pi^-(\mu^+\mu^-)_{\text{fit}})$ for the values of this variable up to 10.78 GeV/c². To further investi-
 696 gate the shape of $M(\pi^+\pi^-(\mu^+\mu^-)_{\text{fit}})$ in this special MC sample, we plot the distribution of
 697 $M(\pi^+\pi^-(\mu^+\mu^-)_{\text{fit}})$ using the logarithmic scale in Fig. 30. We observe that the distribution
 698 shown in the figure does not follow a simple exponential dependence on $M(\pi^+\pi^-(\mu^+\mu^-)_{\text{fit}})$
 699 in part because, as explained previously, the ISR spectrum in this MC sample is completely
 700 unreasonable.

701 We reskim the data and generic background MC, blind the signal region and present
 702 the data distributions of photon energy spectrum vs $M(\pi^+\pi^-(\mu^+\mu^-)_{\text{fit}})$ in Fig. 31 and
 703 $M(\pi^+\pi^-(\mu^+\mu^-)_{\text{fit}})$ in Fig. 32. We observe unambiguous signatures of $\Upsilon(2S)$ and $\Upsilon(3S)$
 704 ISR production. We also show the distribution of $M(\pi^+\pi^-(\mu^+\mu^-)_{\text{fit}})$ for blinded data in
 705 Figures 33 and 34 using the logarithmic scale. Note that the last figure is plotted using

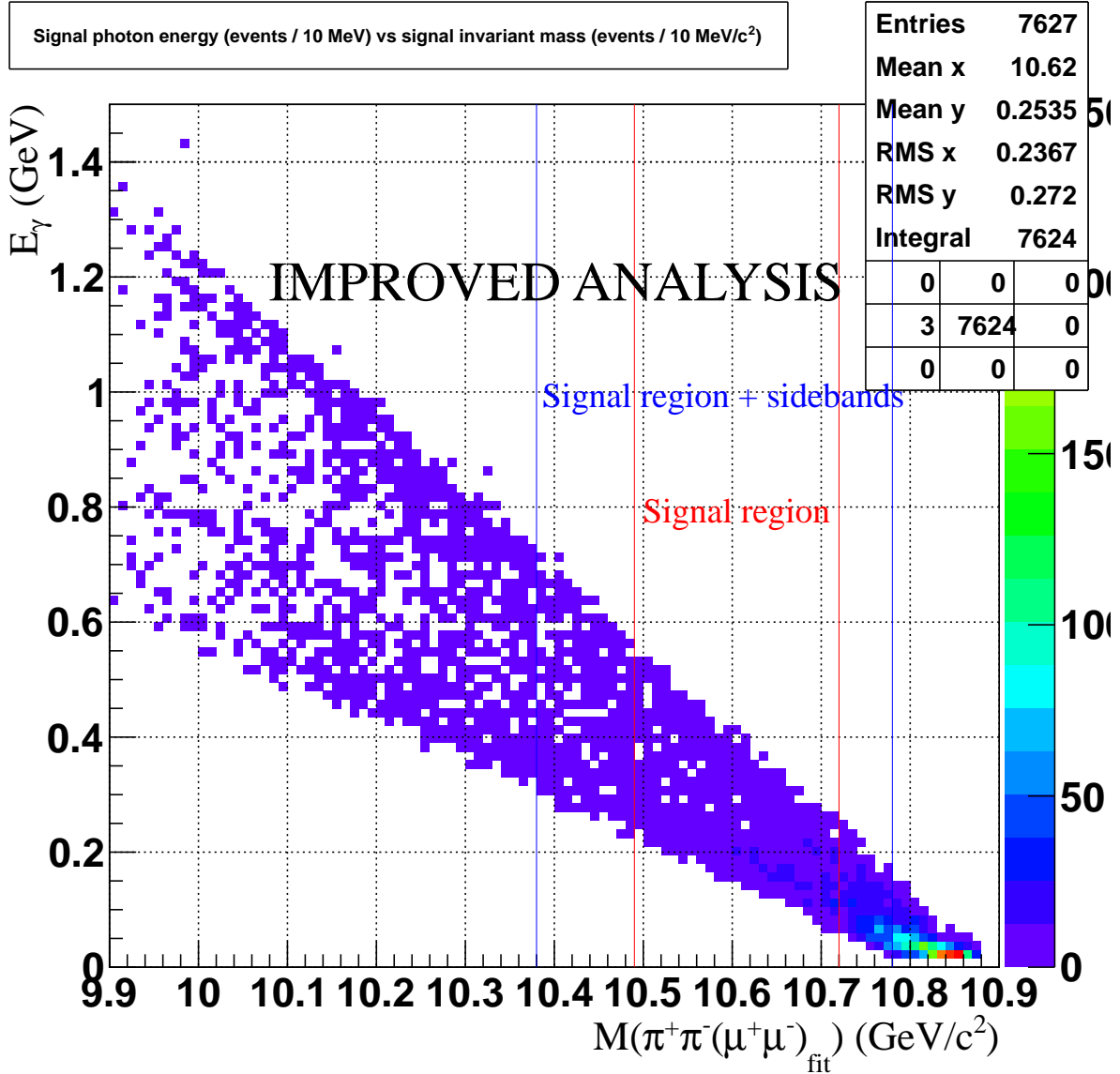


Figure 28: The reconstructed signal photon energy versus the invariant mass $M(\pi^+\pi^-(\mu^+\mu^-)_{\text{fit}})$ for a special ISR MC sample with relaxed selection criteria. Only best candidates are shown.

706 a finer bin width of $2 \text{ MeV}/c^2$ in a narrower range of the invariant mass. Using the data,
 707 we perform a rough estimate of the width of the peak seen at the nominal mass of $\Upsilon(3S)$,
 708 $10.355 \text{ GeV}/c^2$, corresponding to events originating from radiative return to $\Upsilon(3S)$. Using
 709 our estimate of $5 \text{ MeV}/c^2$ (consistent with our MC-based understanding of resolution), we
 710 conclude that events in the left sideband of Fig. 34 are at least 5 width units away from
 711 this peak. Hence, it is unlikely that events in our left sideband are from radiative return to
 712 $\Upsilon(3S)$.

713 In the next section we explain our fitting strategy for extracting the signal from data
 714 (when the permission to unblind is granted). We fit the data in the range of signal invariant
 715 mass $M(\pi^+\pi^-(\mu^+\mu^-)_{\text{fit}})$ between the two blue vertical lines shown in Figures 27–34, *i.e.*

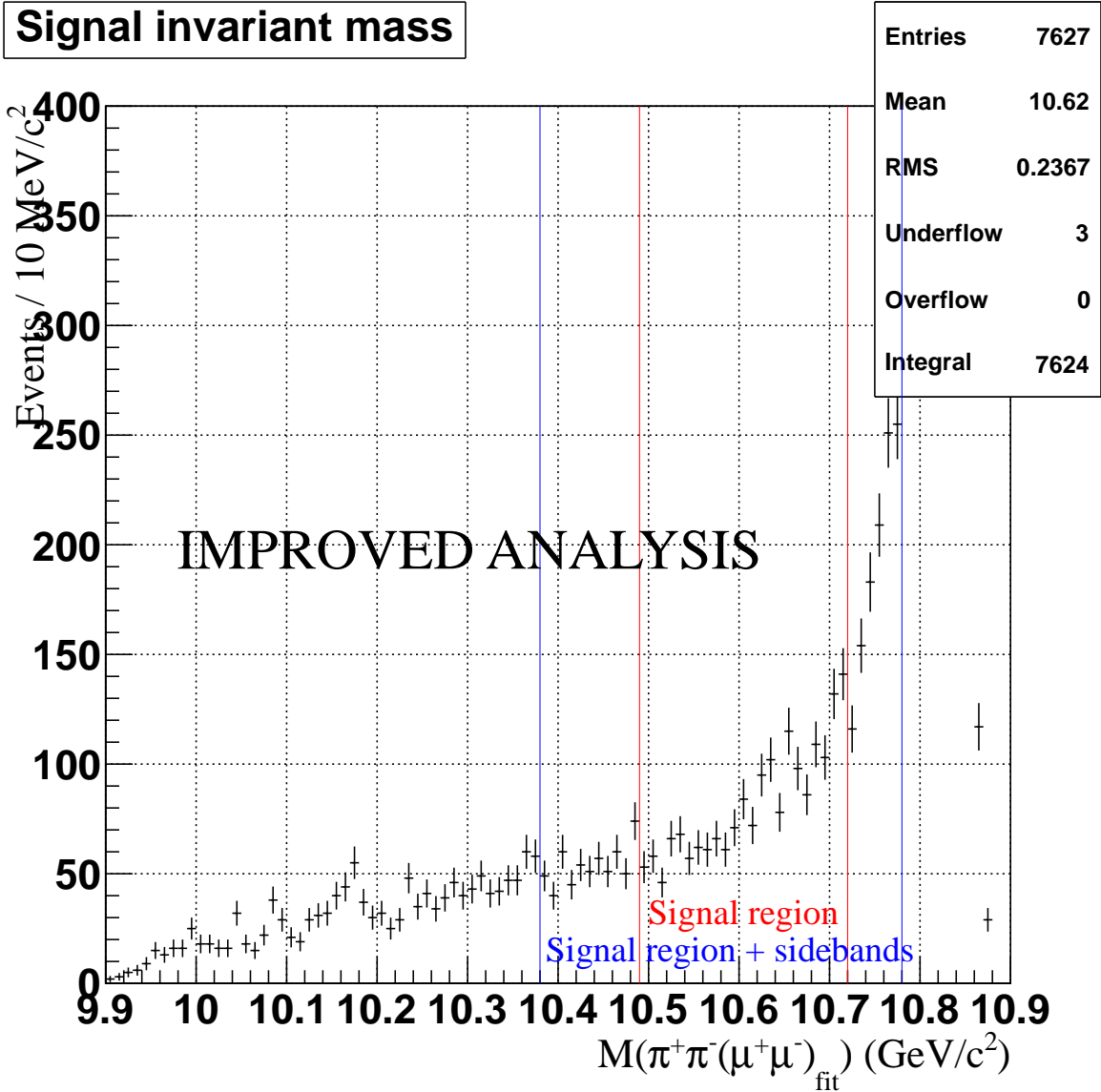


Figure 29: The reconstructed invariant mass $M(\pi^+\pi^-(\mu^+\mu^-)_{\text{fit}})$ for a special ISR MC sample with relaxed selection criteria. Only best candidates are shown.

716 in the range $10.38 \text{ GeV}/c^2 \leq M(\pi^+\pi^-(\mu^+\mu^-)_{\text{fit}}) \leq 10.78 \text{ GeV}/c^2$. This region of the
 717 invariant mass in blinded data is shown in Fig. 35.

718 Finally, to conclude this section, we present Figures 36–39, where we show the distri-
 719 butions of the energy of the signal photon candidate versus $M(\pi^+\pi^-(\mu^+\mu^-)_{\text{fit}})$ and the
 720 projections onto the $M(\pi^+\pi^-(\mu^+\mu^-)_{\text{fit}})$ invariant mass for our correctly reweighted ISR MC
 721 sample (described in section 6) for the decay $\Upsilon(5S) \rightarrow \Upsilon(1S)\pi^+\pi^-$.

722 10.3 Fitting Strategy

723 To extract the $W_{b,J}$ signal from the data or to estimate the upper limit on its production, we
 724 (plan to) fit the invariant mass distribution $M(\pi^+\pi^-(\mu^+\mu^-)_{\text{fit}})$ in data with the sum of an

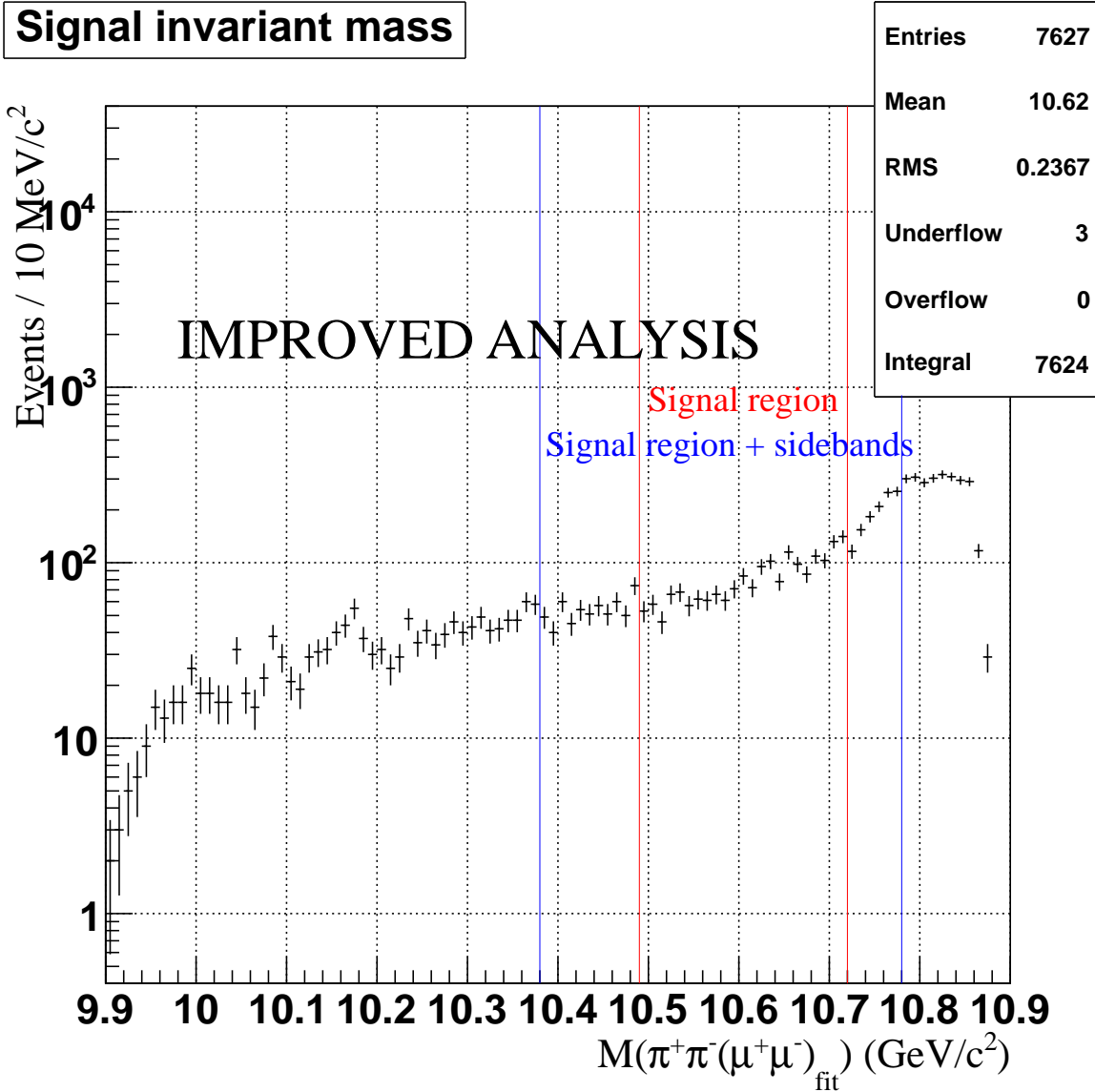


Figure 30: The reconstructed invariant mass $M(\pi^+\pi^-(\mu^+\mu^-)_{\text{fit}})$ for a special ISR MC sample with relaxed selection criteria shown using the logarithmic scale. The ISR spectrum in this special MC sample has an unreasonable shape and could not be described by an exponential. Only best candidates are shown.

725 exponential, a straight line of zero or positive slope and the model for the signal shown in
 726 Fig. 21a. We plan to perform such fits for the values of (fixed) nominal mass of W_{bJ} between
 727 10.5 and 10.7 GeV/c² in steps of a few MeV/c². Important reference points here are provided
 728 by the invariant masses of Z_B and Z'_b which are, respectively, 10.610 and 10.650 GeV/c². We
 729 expect (or, rather, M. Voloshin expects) W_{bJ} to be roughly as wide (or narrow) as $Z_b^{(l)}$. This
 730 makes our life easier. Each fit will be performed independently. The shape of background
 731 distribution will be obtained from the data including the signal region. In our opinion, we
 732 can not obtain the shape of background exclusively from the sidebands because our sidebands

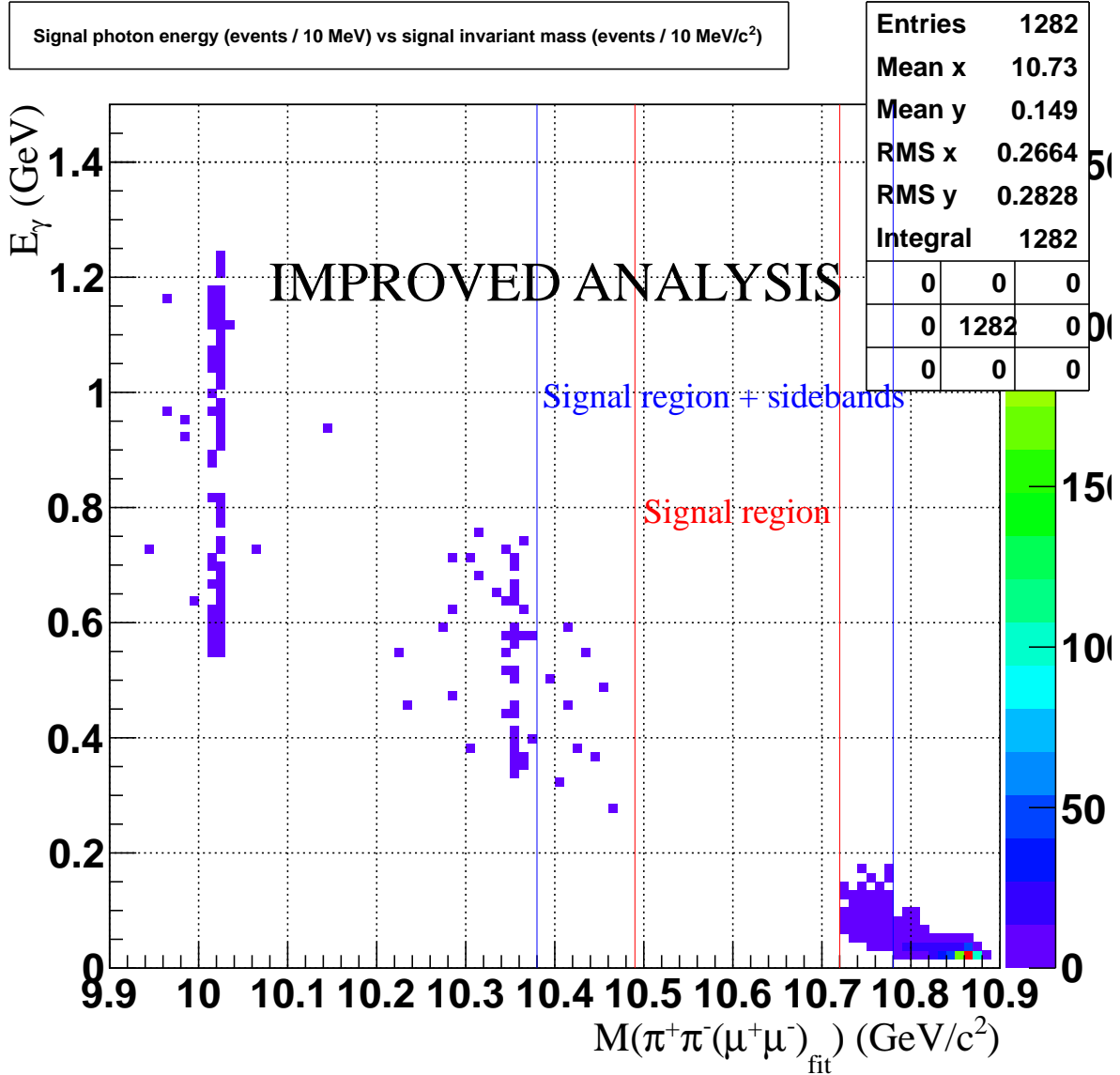


Figure 31: The reconstructed signal photon energy versus the invariant mass $M(\pi^+\pi^-(\mu^+\mu^-)_{\text{fit}})$ for blinded data with relaxed selection criteria. Only best candidates are shown.

733 are relatively narrow and, also, if the shape of the background function is fixed using our
 734 sidebands, fitting with the model described in this section could easily introduce a significant
 735 bias in the results of the fit. Another limitation comes from the wide range of the invariant
 736 mass region where we are searching for the W_{bJ} . For each individual fit (with a particular
 737 hypothesis for W_{bJ} mass), the effective sideband region is going to be significantly wider than
 738 in our exercises discussed in this section. The key assumptions are: 1) there are no peaking
 739 backgrounds in the entire signal region, and 2) backgrounds can be modeled by the sum of
 740 an exponential and a straight line. Our confidence is based on MC studies using, first of all,
 741 our ISR MC samples.

742 We fit the invariant mass $M(\pi^+\pi^-(\mu^+\mu^-)_{\text{fit}})$ in the range between $10.38 \text{ GeV}/c^2 \leq$

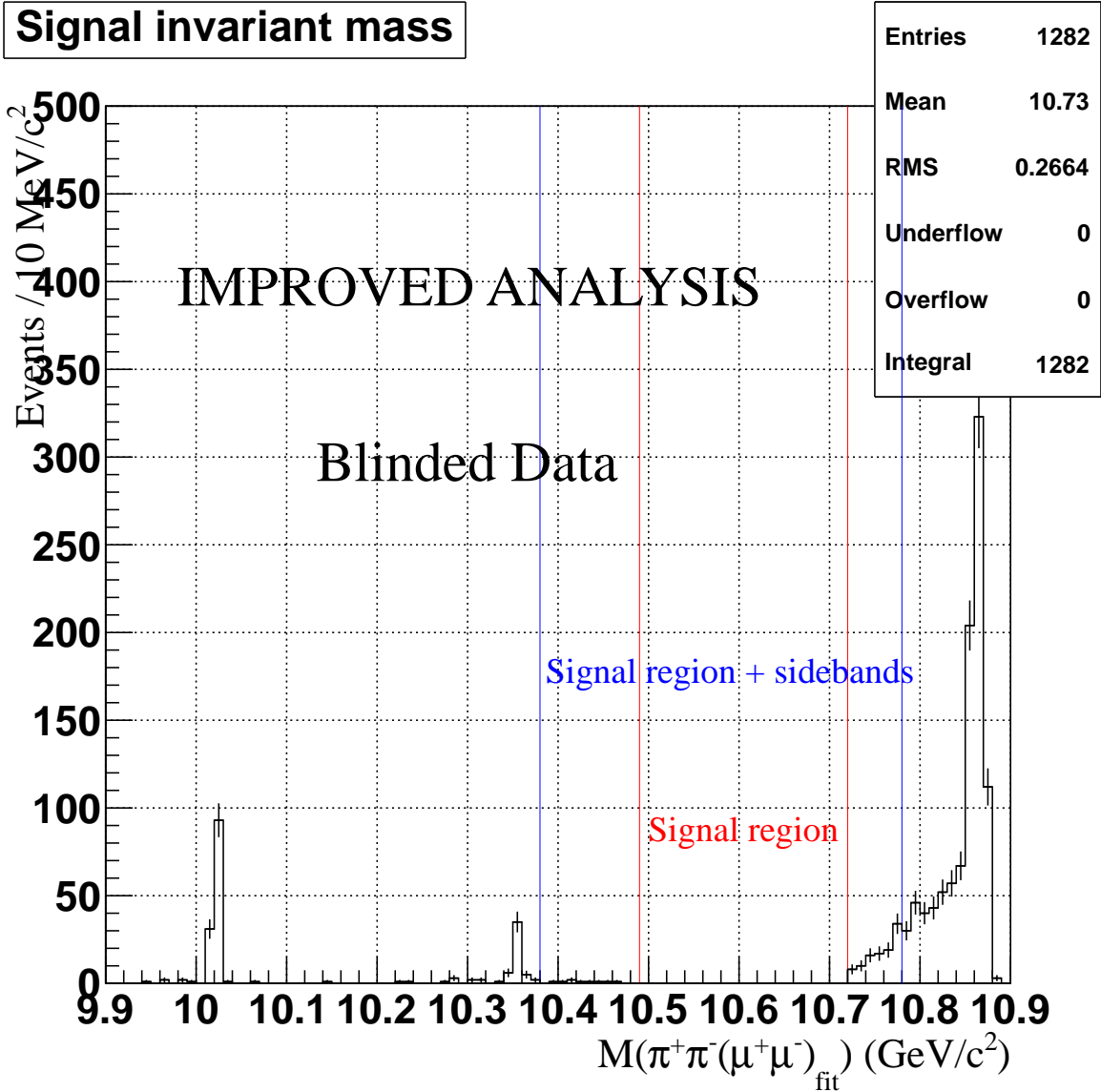


Figure 32: The reconstructed invariant mass $M(\pi^+\pi^-(\mu^+\mu^-)_{\text{fit}})$ for blinded data with relaxed selection criteria. Only best candidates are shown.

743 $M(\pi^+\pi^-(\mu^+\mu^-)_{\text{fit}}) \leq 10.78 \text{ GeV}/c^2$. In principle, we can (significantly) extend the invariant
 744 mass included in the fit toward smaller values (therefore including the radiative production
 745 of $\Upsilon(3S)$ or even $\Upsilon(2S)$ in our fits), however, it is not clear to us if this would necessarily
 746 help us understand the shape of the background and to reduce the uncertainty in our model
 747 description of the data in the signal region.

748 In this section we show some of the results of our unbinned extended maximum likelihood
 749 fits to $M(\pi^+\pi^-(\mu^+\mu^-)_{\text{fit}})$ using a model implemented using RooFit for various MC samples
 750 under different conditions.

751 We start our adventure by fitting the distribution of properly reweighted ISR MC sample
 752 for the decay $\Upsilon(5S) \rightarrow \Upsilon(1S)\pi^+\pi^-$ shown in Fig. 39. We fit this distribution using the
 753 unbinned extended maximum likelihood technique implemented in RooFit with the sum of

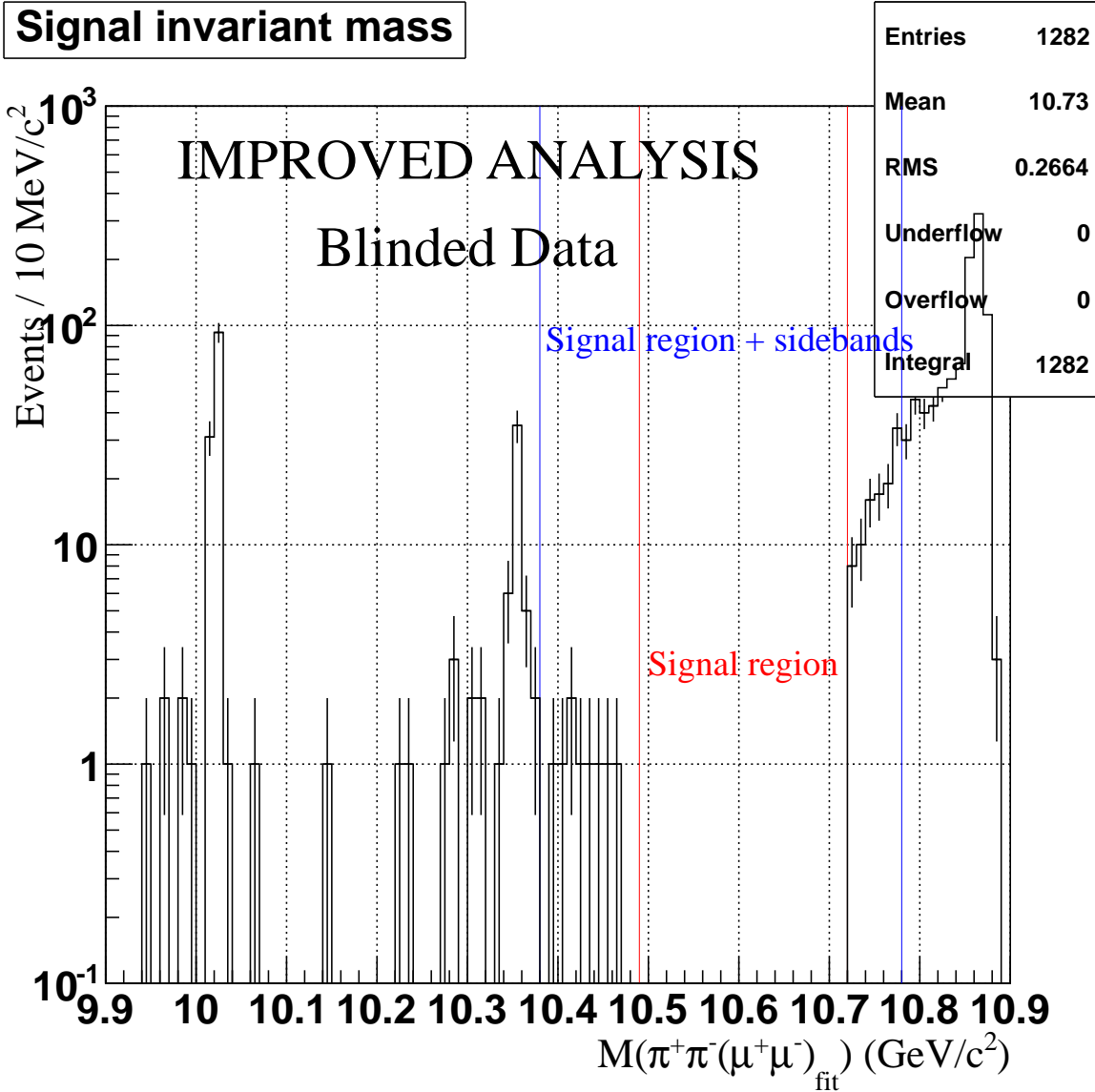


Figure 33: The reconstructed invariant mass $M(\pi^+\pi^-(\mu^+\mu^-)_{\text{fit}})$ for blinded data with relaxed selection criteria plotted using the logarithmic scale. This is the same distribution as shown in Fig. 32. Only best candidates are shown.

754 an exponential and a straight line of zero or positive slope (if the curious reader really wants
 755 to know, we use `RooChebychev` for the latter). The results of this fit are shown in Fig. 40.
 756 We show the results of the fit using both the linear and the logarithmic scales because while
 757 one PDF is linear when plotted on log scale, the other PDF is, surprise, linear when plotted
 758 on linear scale because it is a line! Note that the fit has four parameters: α is the parameter
 759 of the exponent, `slope` is the slope of the straight line, $N1$ and $N2$ are the numbers of
 760 events obtained from the fit for background contributions parameterized by the exponent
 761 and the straight line, respectively. Note that we can not replace these two parameters by
 762 a single fraction parameter in an **extended** ML fit. When we fit real data, we plan to let
 763 the relative contributions from the two PDFs to be independently varying parameters in

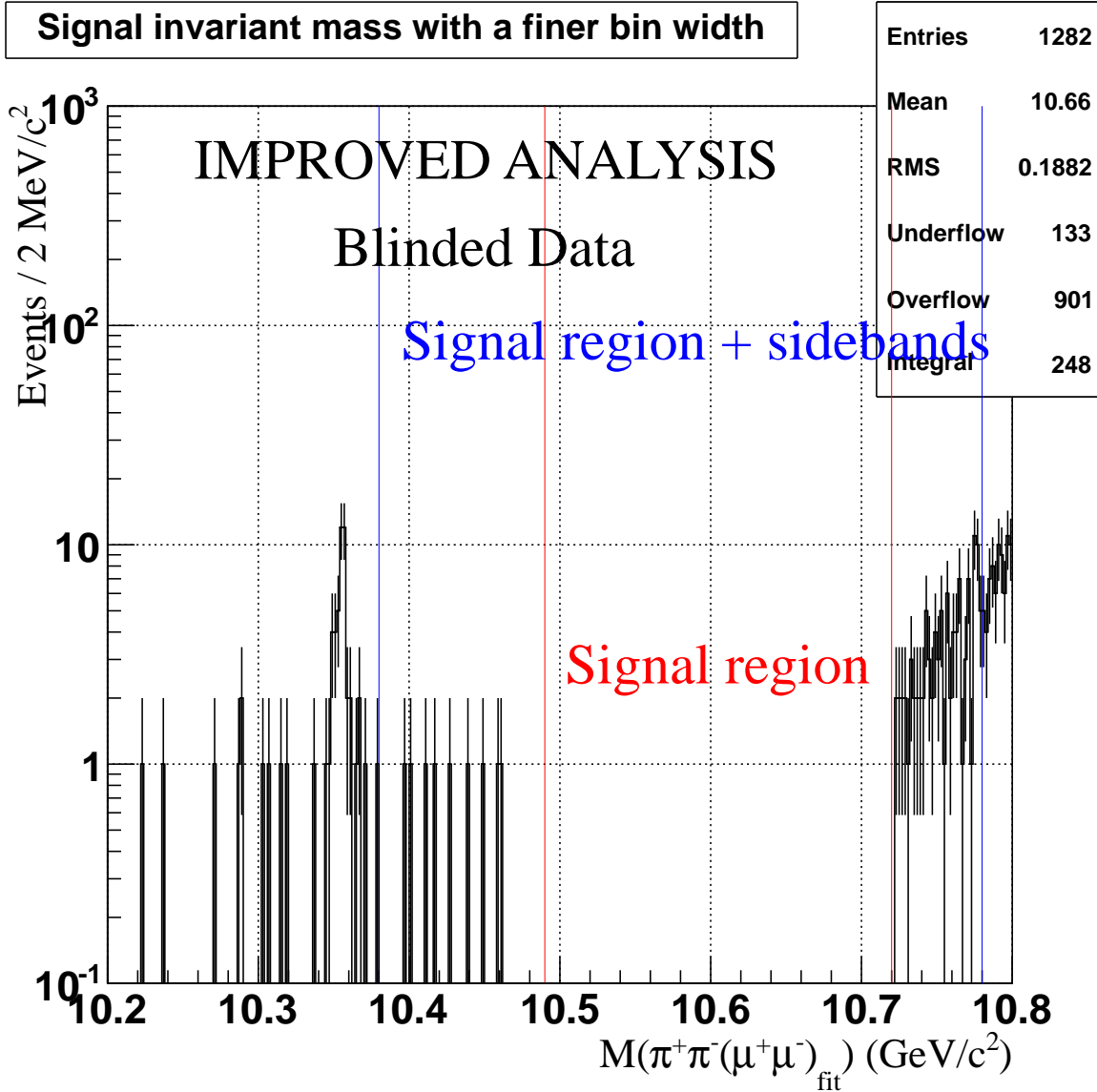


Figure 34: The reconstructed invariant mass $M(\pi^+\pi^-(\mu^+\mu^-)_{\text{fit}})$ for blinded data with relaxed selection criteria plotted using the logarithmic scale for a narrower region of the invariant mass using a finer bin width than used for plots shown in Figures 32 and 33. Only best candidates are shown.

764 the fit, same way it is the case in fits described here. This degree of freedom could be used
 765 to approximate (a small contribution, as we conclude from studying the sidebands) from
 766 non-peaking background possibly present in data in the signal region.

767 In the next step we exclude events in the signal region from the fit and repeat the
 768 described exercise for the same ISR MC sample. The results are shown in Fig. 41. One can
 769 easily notice that our sidebands are not sufficiently wide to use these to obtain the shape of
 770 background in the **entire** signal region. This is the reason why, when fitting the data, these
 771 two PDFs, an exponential and a straight line, will be combined with a signal PDF. In either
 772 case, one can see that presence of ISR definitely introduces a large systematic uncertainty in

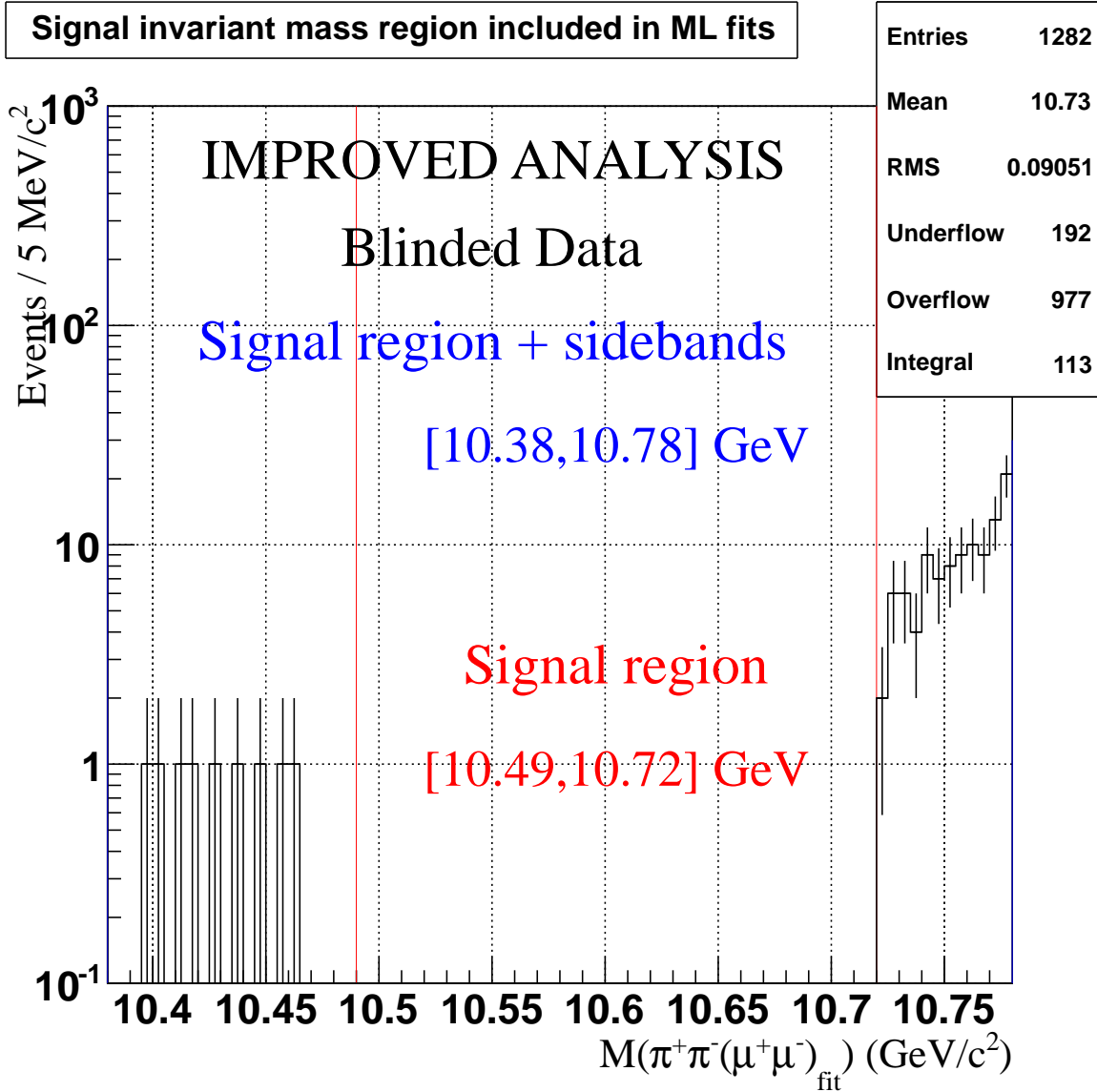


Figure 35: The reconstructed invariant mass $M(\pi^+\pi^-(\mu^+\mu^-)_{\text{fit}})$ for blinded data with relaxed selection criteria plotted using the logarithmic scale for the region of the invariant mass included in the fits. Same events are shown as in Figures 32–34 but using a different bin width. Only best candidates are shown.

773 our results for (relatively) larger invariant masses of W_{bJ} , in the region where the exponential
 774 contribution is rapidly increasing.

775 Now we try to fit the blinded data (just to see if the fit is going to converge at all).
 776 The results of the fit are shown in Fig. 42. Again, we observe that it would be unrealistic
 777 to expect our sidebands to predict the background in the entire, 400 MeV/c²-wide signal
 778 region.

779 Now we try to fit our precious ISR MC sample using three PDFs: the exponential
 780 and the straight line approximating background and the signal line shape shown in Fig. 21a
 781 (convolution of the signal Breit-Wigner with two Gaussians prepared using FFT plug-in in

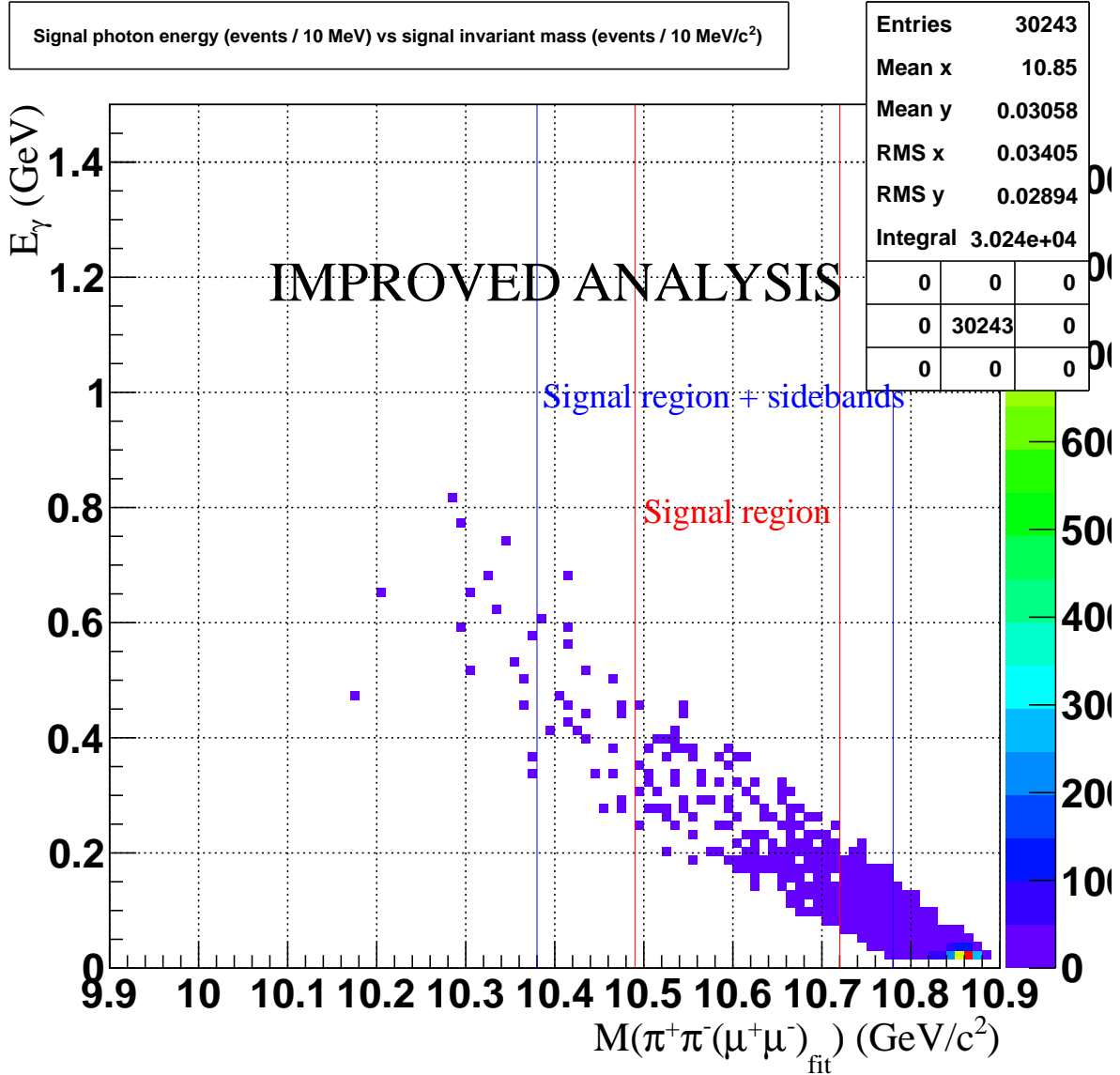


Figure 36: The reconstructed signal photon energy versus the invariant mass $M(\pi^+\pi^-(\mu^+\mu^-)_{\text{fit}})$ for ISR MC sample described in section 6 with relaxed selection criteria. Only best candidates are shown.

782 ROOT). Note that no signal MC events have been added to the pure ISR MC sample yet.
 783 The number of signal events (NS) is an additional parameter in the fit, but the shape of
 784 the signal and its location (*i.e.* the invariant mass of W_{bJ} set at $10.6 \text{ GeV}/c^2$) are fixed
 785 in this fit. As you can see in Fig. 43 the fit finds no statistically significant signal. Note
 786 that the solid green curve superimposed on the results of the fit shows how 50 signal events
 787 would look on average according to signal PDF description. The result of the fit for NS is
 788 a negative fluctuation.

789 Inspired by our success, we now ask the fitter to search for the signal (where there is
 790 none) in ISR MC sample. To do so we let the nominal mass of the W_{bJ} float in the range
 791 between 10.5 and $10.7 \text{ GeV}/c^2$. Note that in our future fits to data we plan to **scan** through

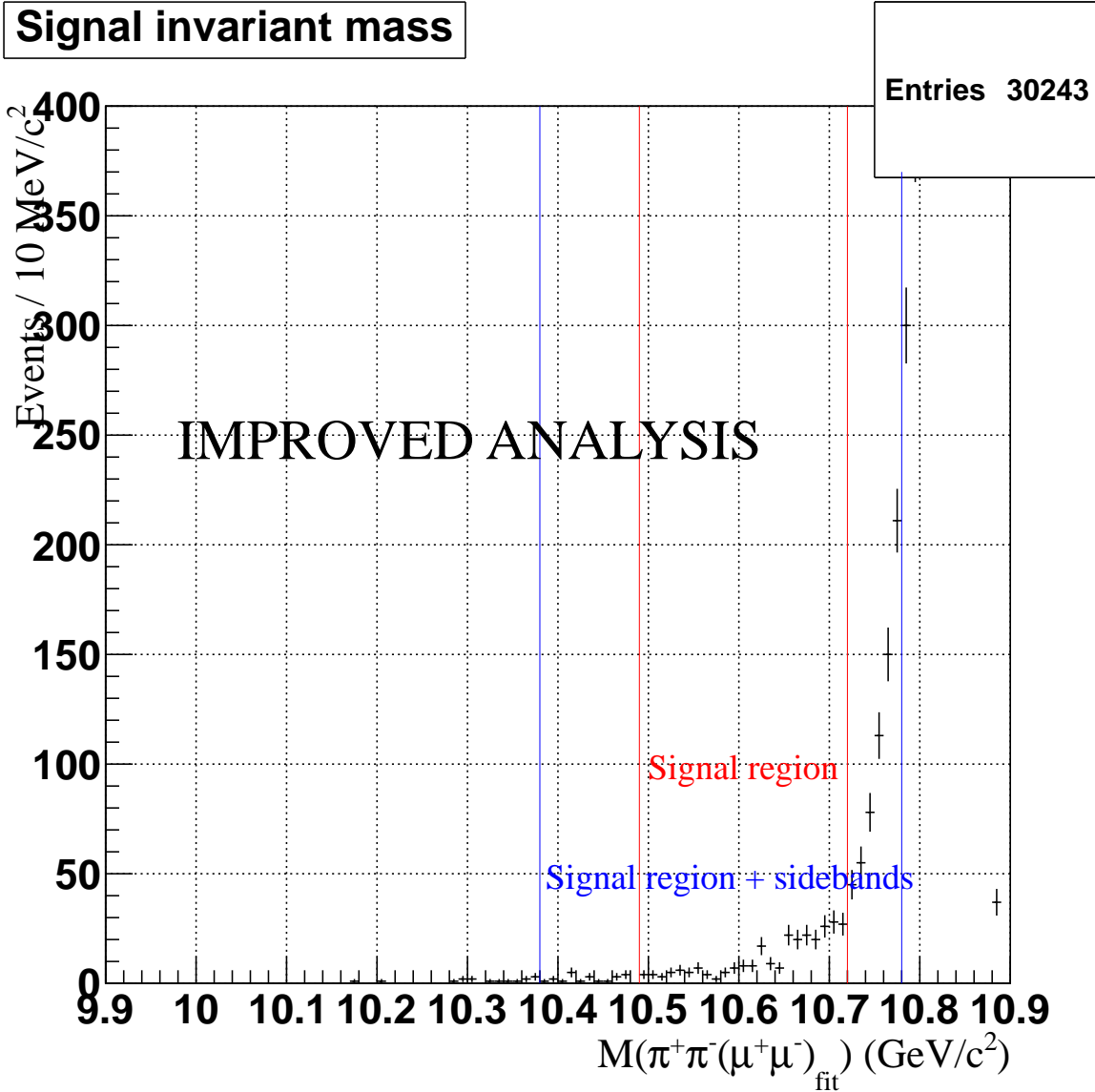


Figure 37: The reconstructed invariant mass $M(\pi^+\pi^-(\mu^+\mu^-)_{\text{fit}})$ for ISR MC sample described in section 6 with relaxed selection criteria. Only best candidates are shown.

792 this interval of $M(\pi^+\pi^-(\mu^+\mu^-)_{\text{fit}})$, however, for the fit performed here we simply want to
 793 see the significance of the worst-case-scenario when the fit “discover” a signal where there
 794 is none. The results of this fit are shown in Fig. 44. Indeed, an obvious enhancement
 795 in the distribution of $M(\pi^+\pi^-(\mu^+\mu^-)_{\text{fit}})$ is “picked-up” by the fitter as the most likely
 796 “signal”, however, as you can observe from the results of the fit, statistical significance of
 797 this “discovery” is consistent with a fluctuation. Such results are also likely to be obtained
 798 in the data, and, in case of low significance and no discovery, this would blow up the upper
 799 limit estimate.

800 Finally, being brave young pioneers, we decide to tackle a simulated data sample where
 801 50 events (with $W_{b,J}$ mass of $10.620 \text{ GeV}/c^2$) are randomly selected from one of our simulated
 802 signal MC sample and are added to the same ISR MC sample we are using for all our fits

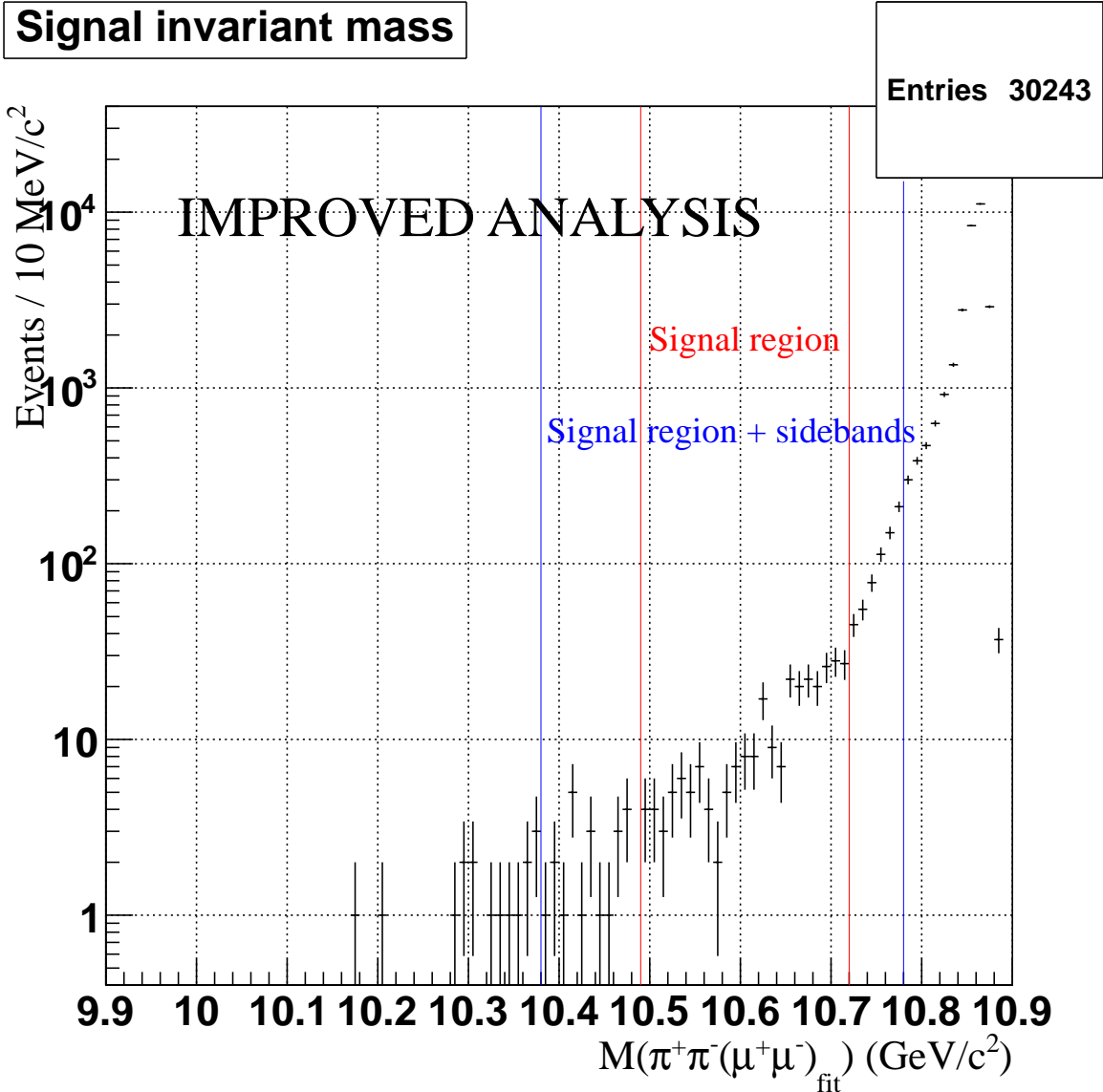


Figure 38: The reconstructed invariant mass $M(\pi^+\pi^-(\mu^+\mu^-)_{\text{fit}})$ for ISR MC sample described in section 6 with relaxed selection criteria shown using the logarithmic scale. Only best candidates are shown.

803 described in this section. We let the fitter search for this signal and report the results in
 804 Fig. 45. The fitter finds the signal of the right magnitude. We conclude that our fitting
 805 procedure is working.

806 Now knowing that our fitting procedure works, we perform a scan on our reweighted ISR
 807 MC sample for the decay $\Upsilon(5S) \rightarrow \Upsilon(1S)\pi^+\pi^-$, holding the nominal mass of W_{bJ} fixed for
 808 values between 10.5 and 10.7 GeV/c^2 in steps of a 5 MeV/c^2 . The results of the scan are
 809 shown in Fig. 46.

810 We perform another (identical) scan on our reweighted ISR MC sample, but this time,
 811 we include 50 toy signal MC events generated from our signal PDF (with the signal mass
 812 fixed at values between 10.5 and 10.7 GeV/c^2 in steps of a 5 MeV/c^2 . The results of the

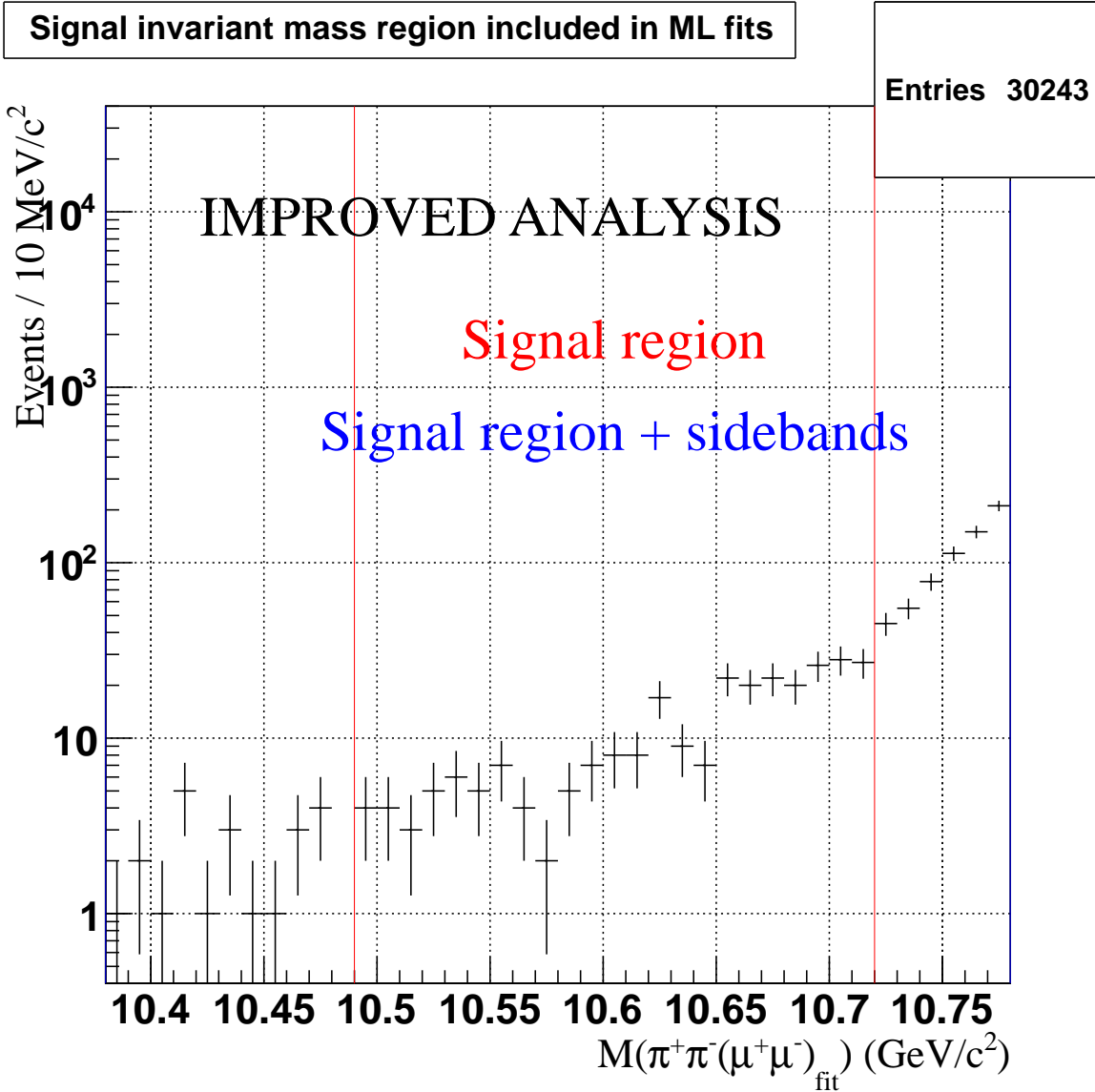


Figure 39: The reconstructed invariant mass $M(\pi^+\pi^-(\mu^+\mu^-)_{\text{fit}})$ for ISR MC sample described in section 6 with relaxed selection criteria shown using the logarithmic scale for the mass region used in the fits. Only best candidates are shown.

813 scan are shown in Fig. 47.

814 Finally, blind data contain 9 events in the lower-mass sideband and 104 events in the
 815 higher-mass sideband, while ISR MC has 22 events in the lower-mass sideband and 652
 816 events in the higher-mass sideband. On basis of this comparison we conclude that our ISR
 817 MC sample is larger than the statistics in data. Therefore, future fits to data will likely
 818 yield results which are more competitive than the estimates shown in this section. To show
 819 an example of a possible improvement, we randomly reduce our ISR sample in the fitting
 820 region to half the size in the original ISR sample and repeat the scans to ISR-only sample
 821 and ISR sample mixed with 50 toy signal MC events. The results of these scans are shown
 822 in Figures 48 and 49.

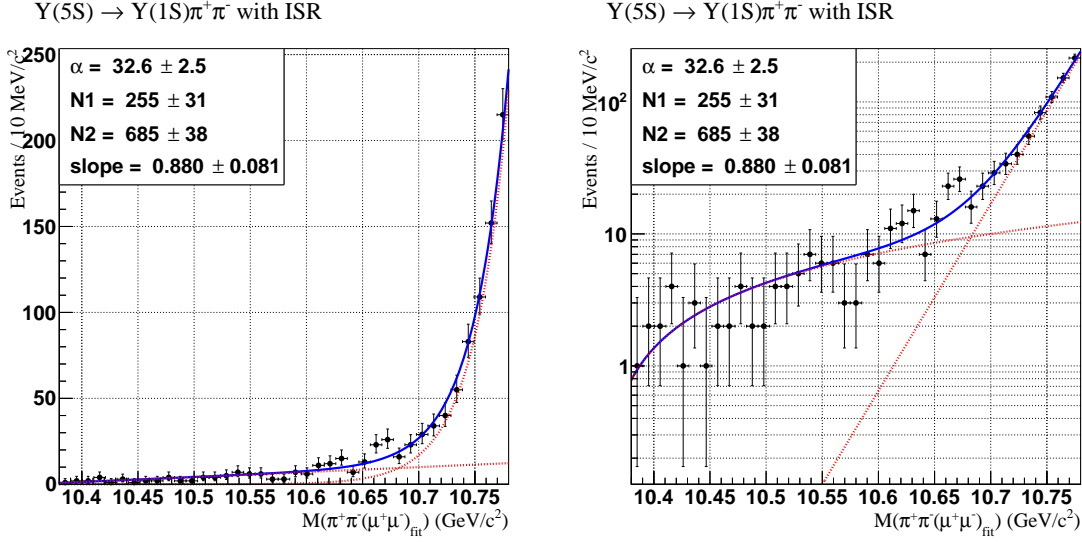


Figure 40: The results of the ML fit for ISR MC sample.

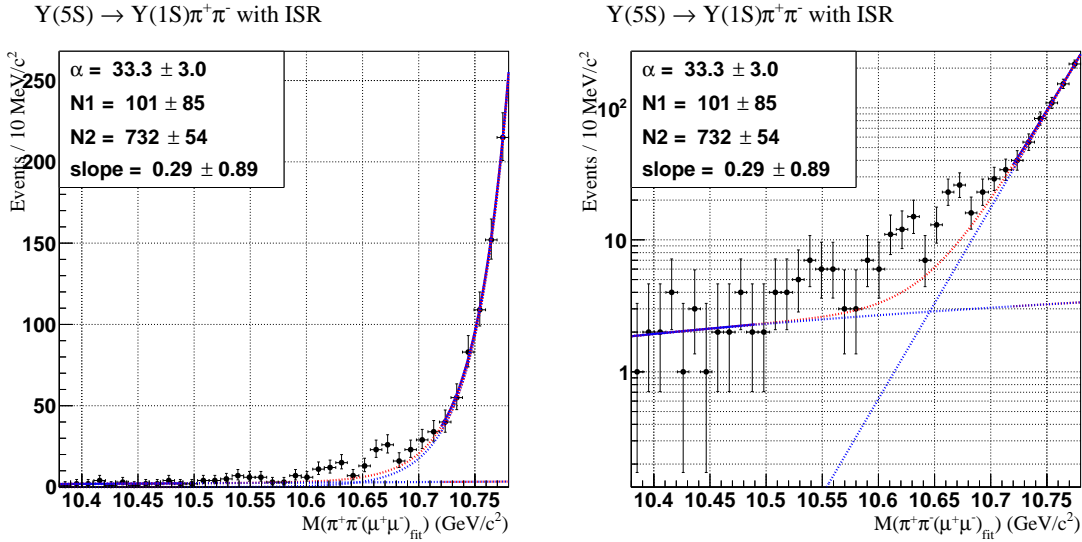


Figure 41: The results of the ML fit for ISR MC sample excluding the signal region.

References

823

824 [1] A. Bondar et al. Observation of two charged bottomonium-like resonances in $Y(5S)$
825 decays. *Phys. Rev. Lett.*, 108:122001, 2012.

826 [2] I. Adachi et al. Evidence for a $Z_b^0(10610)$ in Dalitz analysis of $\Upsilon(5S) \rightarrow Y(nS)\pi^0\pi^0$.
827 2012.

828 [3] P. Krokovny et al. First observation of the $Z_b^0(10610)$ in a Dalitz analysis of $\Upsilon(10860)$
829 $\rightarrow \Upsilon(nS)\pi^0\pi^0$. *Phys. Rev.*, D88(5):052016, 2013.

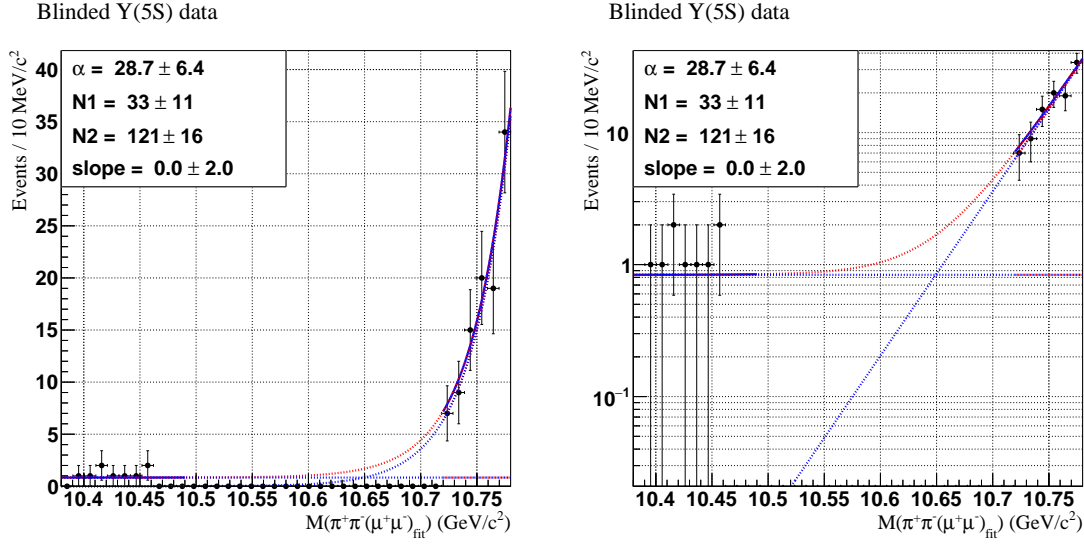


Figure 42: The results of the ML fit for sidebands of the blinded data sample.

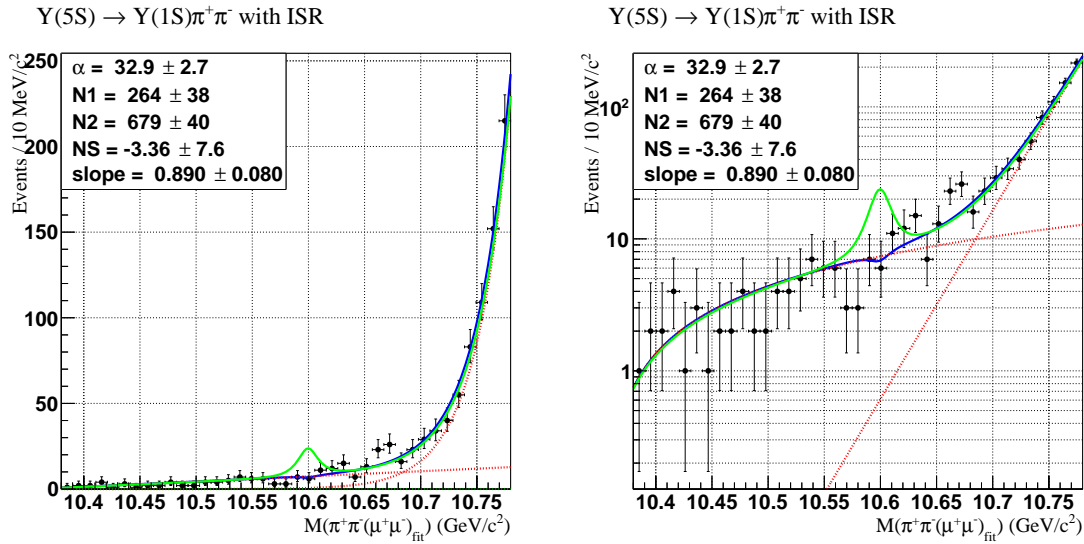


Figure 43: The results of the ML fit for ISR MC sample with background model and signal PDF shape.

- 830 [4] A. Garmash et al. Observation of $Z_b(10610)$ and $Z_b(10650)$ Decaying to B Mesons.
831 *Phys. Rev. Lett.*, 116(21):212001, 2016.
- 832 [5] L. M. Lederman. The discovery of the Upsilon, bottom quark, and B mesons. In
833 *The Rise of the standard model: Particle physics in the 1960s and 1970s. Proceedings,*
834 *Conference, Stanford, USA, June 24-27, 1992*, pages 101–113, 1992.
- 835 [6] M. Tanabashi et al. Review of Particle Physics. *Phys. Rev.*, D98(3):030001, 2018.
- 836 [7] S. Godfrey and N. Isgur. Mesons in a Relativized Quark Model with Chromodynamics.
837 *Phys. Rev.*, D32:189–231, 1985.

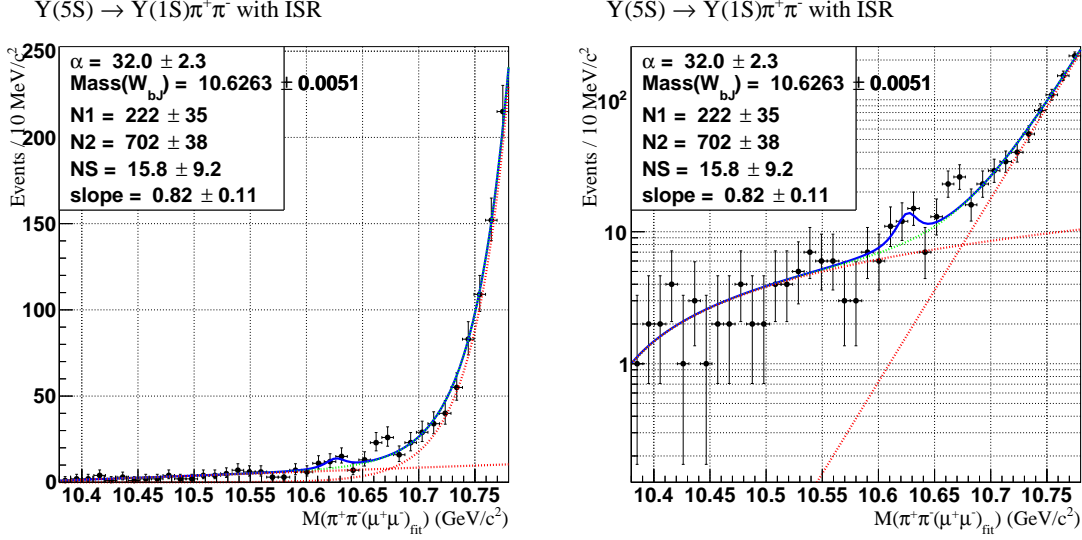


Figure 44: The results of the ML fit for ISR MC sample with background model and signal PDF shape (mass is a free parameter).

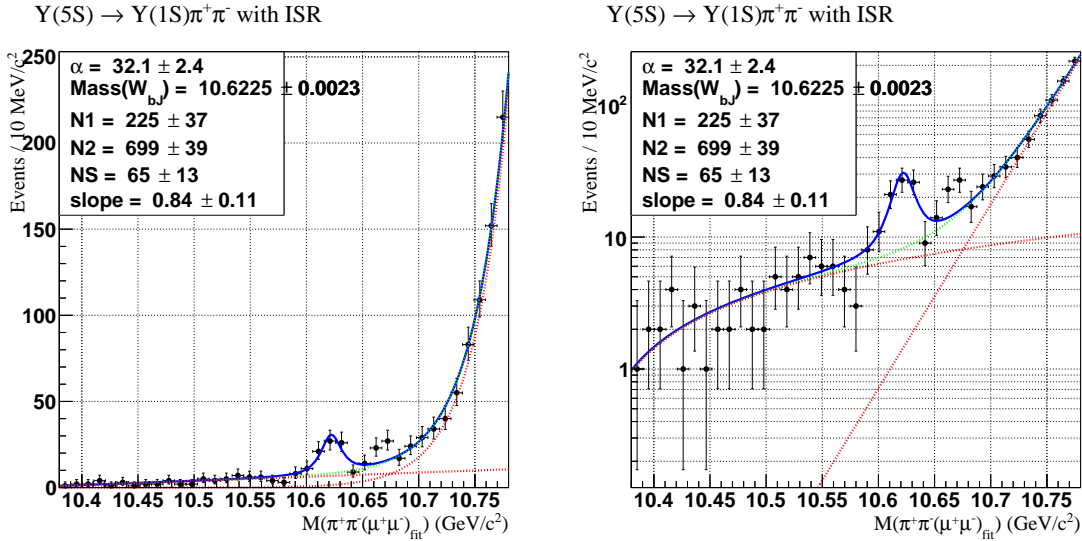


Figure 45: The results of the ML fit for ISR + signal (50 events) MC sample with background model and signal PDF shape (mass is a free parameter).

838 [8] S. Godfrey and K. Moats. Bottomonium Mesons and Strategies for their Observation.
 839 *Phys. Rev.*, D92(5):054034, 2015.

840 [9] S. Godfrey, K. Moats, and E. S. Swanson. B and B_s Meson Spectroscopy. *Phys. Rev.*,
 841 D94(5):054025, 2016.

842 [10] A. E. Bondar, R. V. Mizuk, and M. B. Voloshin. Bottomonium-like states: Physics case
 843 for energy scan above the $B\bar{B}$ threshold at Belle-II. *Mod. Phys. Lett.*, A32(04):1750025,
 844 2017.

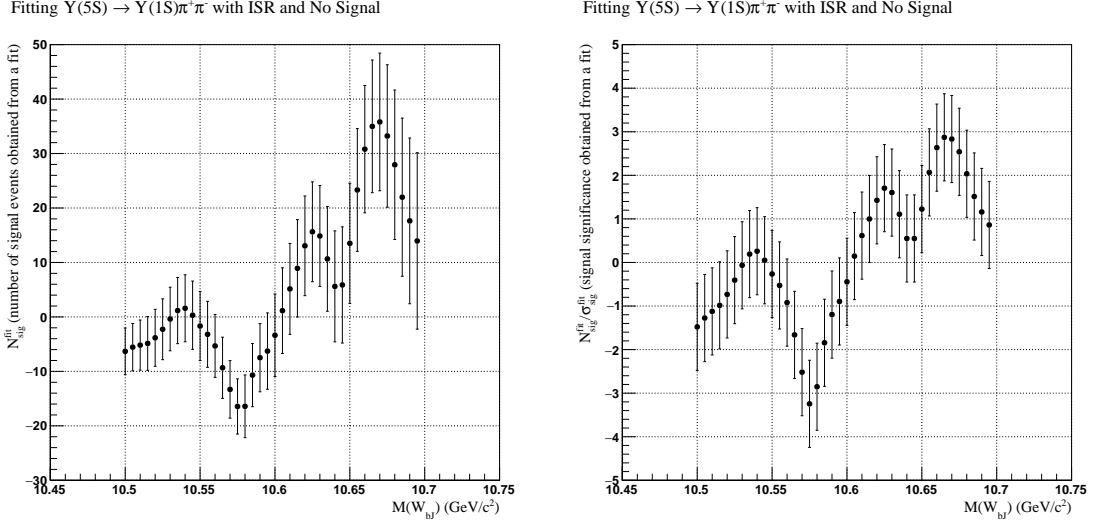


Figure 46: The results of the scan for ISR MC sample with background model and signal PDF shape.

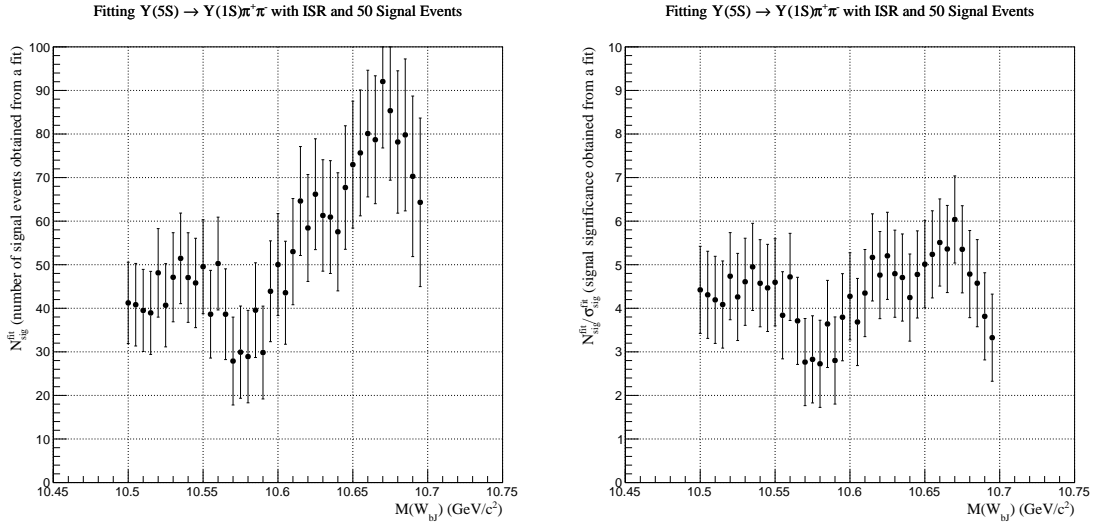


Figure 47: The results of the scan for ISR MC sample + 50 toy MC signal events with background model and signal PDF shape.

- 845 [11] A. E. Bondar, A. Garmash, A. I. Milstein, R. Mizuk, and M. B. Voloshin. Heavy quark
846 spin structure in Z_b resonances. *Phys. Rev.*, D84:054010, 2011.
- 847 [12] Stephen Lars Olsen. A New Hadron Spectroscopy. *Front. Phys.(Beijing)*, 10(2):121–154,
848 2015.
- 849 [13] M. B. Voloshin. Radiative transitions from Upsilon(5S) to molecular bottomonium.
850 *Phys. Rev.*, D84:031502, 2011.
- 851 [14] W. Altmannshofer et al. The Belle II Physics Book, arXiv:hep-ex/1808.10567, 2018.

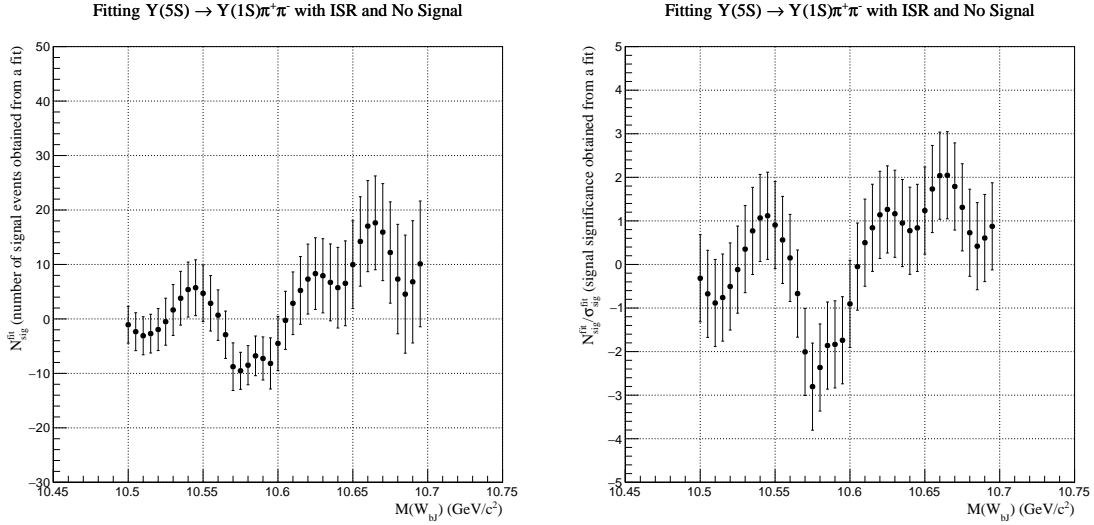


Figure 48: The results of the scan for ISR MC sample with background model and signal PDF shape.

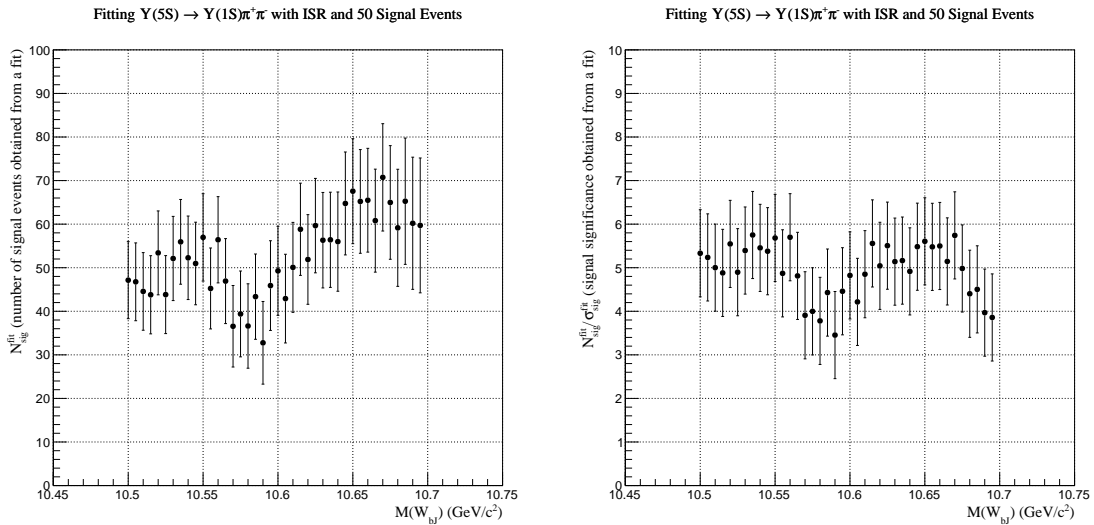


Figure 49: The results of the scan for ISR MC sample + 50 toy MC signal events with background model and signal PDF shape.

852 [15] I. Adachi et al. Study of Three-Body $Y(10860)$ Decays, arXiv:hep-ex/1209.6450,
853 BELLE-CONF-1272, 2012.

854 [16] D. J. Lange. The EvtGen particle decay simulation package. *Nucl. Instrum. Meth.*,
855 A462:152–155, 2001.

856 [17] S. Agostinelli et al. GEANT4: A Simulation toolkit. *Nucl. Instrum. Meth.*, A506:250–
857 303, 2003.

- 858 [18] A. Ryd, D. Lange, N. Kuznetsova, S. Versille, M. Rotondo, D. P. Kirkby, F. K. Wuerth-
859 wein, and A. Ishikawa. EvtGen: A Monte Carlo Generator for B -Physics. 2005.
- 860 [19] E. Barberio and Z. Was. PHOTOS: A Universal Monte Carlo for QED radiative cor-
861 rections. Version 2.0. *Comput. Phys. Commun.*, 79:291–308, 1994.
- 862 [20] J. Brodzicka et al. Physics Achievements from the Belle Experiment. *PTEP*,
863 2012:04D001, 2012.
- 864 [21] M. Benayoun, S. I. Eidelman, V. N. Ivanchenko, and Z. K. Silagadze. Spectroscopy at B
865 factories using hard photon emission. *Mod. Phys. Lett.*, A14:2605–2614, 1999. [Frascati
866 Phys. Ser.15(1999)].
- 867 [22] Wouter Verkerke and David P. Kirkby. The RooFit toolkit for data modeling. *eConf*,
868 C0303241:MOLT007, 2003. [186(2003)].